

# Marine Physical Laboratory

AD-A225 297

## Approaches to the Processing of Data from Large Aperture Acoustic Vertical Line Arrays

Jean-Marie Quoc Danh Tran

DTIC  
ELECTE  
JUL 09 1990  
S B D

SIO Reference 90-21  
April 1990

*Approved for public release; distribution unlimited.*



University of California, San Diego  
Scripps Institution of Oceanography

UNCLASSIFIED

SECURITY CLASSIFICATION OF THIS PAGE

REPORT DOCUMENTATION PAGE				Form Approved OMB No. 0704-0188	
1a. REPORT SECURITY CLASSIFICATION UNCLASSIFIED			1b. RESTRICTIVE MARKINGS		
2a. SECURITY CLASSIFICATION AUTHORITY			3. DISTRIBUTION / AVAILABILITY OF REPORT Approved for public release; distribution unlimited.		
2b. DECLASSIFICATION / DOWNGRADING SCHEDULE					
4. PERFORMING ORGANIZATION REPORT NUMBER(S) SIO Reference 90-21 [MPL-U-26/90]			5. MONITORING ORGANIZATION REPORT NUMBER(S)		
6a. NAME OF PERFORMING ORGANIZATION University of California, San Diego		6b. OFFICE SYMBOL (If applicable) MPL	7a. NAME OF MONITORING ORGANIZATION Office of Naval Research Department of the Navy		
6c. ADDRESS (City, State, and ZIP Code) Marine Physical Laboratory Scripps Institution of Oceanography San Diego, California 92152			7b. ADDRESS (City, State, and ZIP Code) 800 North Quincy Street Arlington, VA 22217-5000		
8a. NAME OF FUNDING / SPONSORING ORGANIZATION Office of Naval Research		8b. OFFICE SYMBOL (If applicable) ONR	9. PROCUREMENT INSTRUMENT IDENTIFICATION NUMBER N00014-87-K-0010		
8c. ADDRESS (City, State, and ZIP Code) 800 North Quincy Street Arlington, VA 22217-5000			10. SOURCE OF FUNDING NUMBERS		
			PROGRAM ELEMENT NO.	PROJECT NO.	TASK NO.
11. TITLE (Include Security Classification) APPROACHES TO THE PROCESSING OF DATA FROM LARGE APERTURE ACOUSTIC VERTICAL LINE ARRAYS					
12. PERSONAL AUTHOR(S) Jean-Marie Quoc Danh Tran					
13a. TYPE OF REPORT thesis		13b. TIME COVERED FROM _____ TO _____		14. DATE OF REPORT (Year, Month, Day) April 1990	
				15. PAGE COUNT 134	
16. SUPPLEMENTARY NOTATION					
17. COSATI CODES			18. SUBJECT TERMS (Continue on reverse if necessary and identify by block number) narrowband frequency data, vertical line arrays		
FIELD	GROUP	SUB-GROUP			
19. ABSTRACT (Continue on reverse if necessary and identify by block number)  This dissertation investigates various approaches to the processing of narrowband frequency data from large aperture acoustic vertical line arrays with on the order of one hundred equally spaced sensors.					
20. DISTRIBUTION / AVAILABILITY OF ABSTRACT <input type="checkbox"/> UNCLASSIFIED/UNLIMITED <input checked="" type="checkbox"/> SAME AS RPT. <input type="checkbox"/> OTIC USERS			21. ABSTRACT SECURITY CLASSIFICATION UNCLASSIFIED		
22a. NAME OF RESPONSIBLE INDIVIDUAL W. S. Hodgkiss			22b. TELEPHONE (Include Area Code) 619 - 534-1798		22c. OFFICE SYMBOL MPL

**UNIVERSITY OF CALIFORNIA**

**SAN DIEGO**

Approaches to the Processing of Data from  
Large Aperture Acoustic Vertical Line Arrays

A dissertation submitted in partial satisfaction of the  
requirements for the degree Doctor of Philosophy  
in Oceanography

by

Jean-Marie Quoc Danh Tran

Committee in charge:

Professor Victor C. Anderson  
Professor Shankar Chatterjee  
Professor LeRoy M. Dorman  
Professor John A. Hildebrand  
Professor William S. Hodgkiss, Jr., Chair

1990

To Sophie

Copyright 1990

by

Jean-Marie Quoc Danh Tran

## Table of Contents

Dedication Page .....	ii
Table of Contents .....	iii
List of Figures .....	vi
List of Tables .....	viii
Acknowledgements .....	ix
Vita .....	x
Abstract .....	xii
<b>Introduction</b> .....	<b>1</b>
<b>1. Array Signal Processing</b> .....	<b>3</b>
1.1. Introduction .....	3
1.2. Basic Assumptions .....	3
1.3. Conventional Beamforming .....	3
1.4. Matched Filter Interpretation of Beamforming .....	6
1.5. Signal Model Definition .....	7
1.6. Adaptive Beamforming .....	8
1.6.1. Optimum vs. Adaptive Processing .....	8
1.6.2. Behaviour of the Minimum Variance Beamformer .....	11
1.6.3. Implementation Issues .....	11
1.6.3.1. Estimating the Covariance Matrix .....	11
1.6.3.2. Inverting the Covariance Matrix .....	13
1.7. Conclusions .....	15
<b>2. Beamforming in a Realistic Environment</b> .....	<b>16</b>
2.1. Introduction .....	16
2.2. The Problem of Correlated Arrivals .....	16
2.2.1. Limitations of the Adaptive Methods .....	16
2.2.2. Structure of the Covariance Matrix Under Correlated Arrivals .....	16
2.2.3. Pre-Processing Methods .....	17
2.2.3.1. Spatial Smoothing .....	17
2.2.3.2. Modified Spatial Smoothing .....	20
2.2.4. Conclusions .....	22
2.3. Wavefront Curvature .....	22
2.3.1. Introduction .....	22
2.3.2. Generating Curved Wavefronts .....	22
2.3.2.1. Derivation of the Phase Relationship in the Vertical ..	23
2.3.2.2. Partial Insonification .....	23
2.3.2.3. How Curved Are Curved Wavefronts ? .....	24
2.3.3. Plane Wavefront Beamformers in a Curved Wavefront Environment .....	24
2.3.4. Curved Wavefront Beamforming .....	25
2.3.4.1. Conventional Curved Wavefront Beamforming .....	25
2.3.4.2. MV Curved Wavefront Beamforming .....	25
2.3.5. Conclusions .....	26

<b>3. Processing Synthetic Data .....</b>	<b>36</b>
3.1. Overview .....	36
3.2. Introduction .....	36
3.3. Beamformer Implementation .....	37
3.3.1. Using Planar Wavefronts .....	37
3.3.2. Using Curved Wavefronts .....	38
3.4. Processing a Very Large Vertical Line Array .....	39
3.4.1. Modeling the Environment .....	39
3.4.2. Processing Results .....	40
3.4.2.1. Conventional Beamforming .....	40
3.4.2.2. MV Processing .....	40
3.4.3. Conclusions .....	41
3.5. Processing a Large Vertical Line Array .....	42
3.5.1. Modeling Results .....	42
3.5.2. Processing Results .....	42
3.5.2.1. Conventional Beamforming .....	42
3.5.2.2. MV Processing .....	42
3.5.2.3. Conclusions .....	33
3.5.3. Signal-Plus-Noise To Noise Ratio Performance Study .....	43
3.5.3.1. Introduction .....	43
3.5.3.2. Description of the Simulation .....	43
3.5.3.3. Results .....	44
3.5.3.4. Array Gain Calculations .....	45
3.5.4. Resolution Study .....	45
3.5.4.1. Description of the Study .....	45
3.5.4.2. Results .....	46
3.5.5. Conclusions .....	46
<b>4. Processing Real Data .....</b>	<b>65</b>
4.1. Overview .....	65
4.2. Presentation of the Data Set .....	65
4.2.1. Introduction .....	65
4.2.2. Description of the VLA System .....	65
4.2.3. Environmental Data .....	66
4.2.4. Data Quality Checks .....	66
4.2.5. Acoustic Modeling .....	66
4.3. Processing Real Data .....	68
4.4. Qualitative Study of the Processing Results .....	69
4.4.1. Conventional Processing .....	69
4.4.2. Full Aperture MV Processing .....	69
4.4.3. Subaperture MV Processing .....	70
4.4.3.1. Experimental Results .....	70
4.4.3.2. Acoustic Modeling .....	71
4.4.4. Conclusions .....	72
4.5. Quantitative Study .....	72
4.5.1. 11 dB Input SNR .....	73
4.5.2. -10 dB Input SNR .....	73
4.6. Array Gain Calculation .....	74
4.7. Conclusions .....	75

<b>5. Matched Field Processing on the VLA Data .....</b>	<b>92</b>
5.1. Overview .....	92
5.2. Introduction to Matched Field Processing .....	92
5.3. Matched Field Processing on Real Data .....	93
5.3.1. Description of the Processing .....	93
5.3.2. 11.8 dB Input SNR Case .....	94
5.3.3. -9.2 dB Input SNR Case .....	95
5.4. Matched Field Processing Simulations .....	96
5.4.1. No Mismatch Simulations .....	96
5.4.2. Analysis of Mismatch .....	96
5.4.3. Tilted Array Simulation .....	96
5.5. Matched Field Performance Study .....	97
5.5.1. 11.8 dB Input SNR Case .....	97
5.5.2. -9.2 dB Input SNR Case .....	98
5.6. Conclusions .....	98
<b>Conclusions .....</b>	<b>114</b>
<b>References .....</b>	<b>116</b>

Accession For	
NTIS GRA&I	<input checked="checked" type="checkbox"/>
DTIC TAB	<input type="checkbox"/>
Unannounced	<input type="checkbox"/>
Justification	
By	
Distribution/	
Availability Codes	
Dist	Avail and/or Special
A-1	



## List of Figures

### Chapter 2

2.1	Upper diagonals of the covariance matrix .....	27
2.2	Upper diagonals of the covariance matrix after spatial smoothing .....	28
2.3	Signal cancellation loss of the MV processor after spatial smoothing .....	29
2.4	Signal cancellation loss of the MV processor after modified spatial smoothing .....	30
2.5	Problem geometry .....	31
2.6	Typical curved wavefront array manifold .....	31
2.7	Phase difference between curved and plane wavefronts .....	32
2.8	Bearing responses of the conventional FFT beamformer to curved wavefronts .....	33
2.9	Bearing responses of the plane wave MV processor to curved wavefronts .....	33
2.10	Loss due to mismatch of the plane wave MV processor under curved wavefront data .....	34
2.11	Bearing responses of the curved wavefront MV processor to curved wavefronts .....	35
2.12	Bearing responses of the MV processor to curved wavefronts using the eigensteering vectors for spatial smoothing on 24 sensors .....	35

### Chapter 3

3.1	Snell's law remapping .....	48
3.2	North-East Pacific historical sound speed profile .....	49
3.3	Propagation experiment geometry .....	50
3.4	GSM eigenrays across the very large vertical line array .....	51
3.5	Conventional beamformer output .....	52
3.6	Full aperture curved wavefront array manifold .....	52
3.7	MV processor output after spatial smoothing on 64 sensors .....	53
3.8	Equivalent array manifold after spatial smoothing on 64 sensors .....	53
3.9	Spectra waterfall calculated by the MV processor on 32-sensor subarrays (after spatial smoothing on 20 sensors) .....	54
3.10	GSM eigenrays across the large vertical line array .....	55
3.11	Conventional beamformer output .....	56
3.12	MV processor output after spatial smoothing on 64 sensors .....	56
3.13	Spectra waterfall computed by the MV processor on 32-sensor subarrays (after spatial smoothing on 20 sensors) .....	57
3.14	Average of the subaperture MV spectra .....	57
3.15	Peak level performance study for a -18 dB input SNR .....	58
3.16	Peak level performance study for a -11 dB input SNR .....	59
3.17	Peak level performance study for a 9 dB input SNR .....	60
3.18	Array Gain .....	61
3.19	Resolution performance study for a -18 dB input SNR .....	62
3.20	Resolution performance study for a -11 dB input SNR .....	63
3.21	Resolution performance study for a 9 dB input SNR .....	64



## Chapter 4

4.1	Sound speed profile at the R/P FLIP .....	76
4.2	Power spectra for selected channels of the VLA .....	77
4.3	Distribution of signal and noise power across the VLA .....	78
4.4	Conventional FFT beamformer output for signal (left) and noise (right) at 200 Hz .....	79
4.5	GSM ray traces .....	80
4.6	GSM power distribution across the VLA .....	80
4.7	GSM eigenrays at 162 km and at the sound axis .....	80
4.8	ATLAS transmission loss versus range at 20 m depth .....	81
4.9	ATLAS power distribution across the VLA .....	81
4.10	Conventional FFT beamformer output on the ATLAS field .....	82
4.11	Conventional FFT beamformer output .....	82
4.12	MV processor output after spatial smoothing on 64 sensors .....	82
4.13	MV processor output after modified spatial smoothing on 64 sensors .....	83
4.14	MV processor output after modified spatial smoothing on 78 sensors .....	83
4.15	MV processor output after modified spatial smoothing on 92 sensors .....	83
4.16	Upper subaperture MV spectrum (modified spatial smoothing length of 48) .....	84
4.17	Lower subaperture MV spectrum (modified spatial smoothing length of 48) .....	84
4.18	Average of the two non-overlapping subaperture MV angular spectra .....	84
4.19	GSM eigenrays between 10° and 15° .....	85
4.20	GSM eigenrays between 160 and 164 km .....	85
4.21	ATLAS modal eigenfunctions .....	86
4.22	Upper and Lower subaperture MV spectra for a single mode pressure field .....	87
4.23	Upper and lower subaperture MV spectra after the Snell's law remapping .....	87
4.24	ATLAS transmission loss .....	88
4.25	Upper and lower subaperture MV spectra of the ATLAS field at 165 km .....	89
4.26	Average of the subaperture MV angular spectra of the ATLAS field ....	89
4.27	Peak level and resolution performance study: 11 dB input SNR .....	90
4.28	Peak level and resolution performance study: -9 dB input SNR .....	91

## Chapter 5

5.1	Matched field processing .....	99
5.2	Matched field processing results on signal, part 1, (11.8 dB input SNR case) .....	100
5.3	Matched field processing results on signal, part 2, (11.8 dB input SNR case) .....	101
5.4	Matched field processing results on noise, part 1, (11.8 dB input SNR case) .....	102
5.5	Matched field processing results on noise, part 2, (11.8 dB input SNR case) .....	103
5.6	Matched field processing results on signal, part 1, (-9.2 dB input SNR case) .....	104
5.7	Matched field processing results on signal, part 2, (-9.2 dB input SNR case) .....	105
5.8	Matched field processing results on noise, part 1, (-9.2 dB input SNR case) .....	106

5.9	Matched field processing results on noise, part 2, (-9.2 dB input SNR case) .....	107
5.10	Matched field processing simulation, part 1, (no mismatch, no noise) .....	108
5.11	Matched field processing simulation, part 2, (no mismatch, no noise) .....	109
5.12	Array navigation data for Tape 915 .....	110
5.13	Tilted array simulation geometry .....	111
5.14	Matched field processing simulation, part 1, (tilted array) .....	112
5.15	Matched field processing simulation, part 2, (tilted array) .....	113

## List of Tables

### Chapter 3

3.1	Bottom loss table (GSM Province Type 3 [Weinberg; 1985]) .....	47
-----	--	----

### Chapter 4

4.1	Length of the data blocks .....	69
4.2	Array Gain .....	75

### Chapter 5

5.1	Matched field processing (11.8 dB input SNR) .....	94
5.2	Matched field processing (-9.2 dB input SNR) .....	95
5.3	Tilted array matched field processing simulation .....	97
5.4	Array gain calculation (11.8 dB input SNR) .....	98
5.5	Array gain calculation (-9.2 dB input SNR) .....	98

## ACKNOWLEDGEMENTS

I wish to thank Dr. Hodgkiss for supervising my work during the past few years with thoughtful advices and encouragements. Dr. Hodgkiss was a stimulating mentor, full of energy and optimism, sharing his knowledge and understanding of the field through continuous comments and recommendations. Thanks also go to my committee members for reviewing this dissertation and offering their feedback.

Some of the original material presented here relies on data collected at sea by Dr. Hildebrand, Chief Scientist on the R/P FLIP during the September 1987 Vertical Line Array Experiment. The array system was developed and built by Vince Pavlicek, Tony Aja, Dick Harris, Howard Humphrey, Pam Scott and Norm Waters. I enjoyed learning from these skilled and dedicated engineers, and also from Gary Austin and Tony Boegeman while in Dr. Spiess's Deep Tow Group. I am grateful for their understanding of my weak stomach while out at sea !

An excellent data analysis environment with large computing resources is available at the Marine Physical Laboratory thanks to Dr. Hodgkiss, John McInerney and Eric Wolin. The availability of the acoustic models, initiated by Dr. Hodgkiss, was crucial to this research and the efforts of Gerald D'Spain and Martin Olivera to port the programs is appreciated. The ATLAS normal mode program developed at the Naval Ocean System Center by Frank Ryan was used extensively in this work. I wish to acknowledge Paul Baxley and Homer Bucker, also from the Naval Ocean System Center, who provided valuable comments and suggestions along the work. I enjoyed sharing ideas and learning from my office mate Gerald D'Spain and also from Lee Culver, Amos Dotan, Christian de Moustier, and Barbara Sotirin. The friendly atmosphere in the laboratory was a great support.

I am indebted to the Henri Kummerman Foundation from Geneva, Switzerland, for the one year fellowship to study in America and to the United States Navy Office of Naval Research which provided funding for this research under contract # N00014-87-K-0010.

I always received support, encouragement and much more from my family and would like to express my deep gratitude to my parents Phong and Françoise. I want to thank my dear wife Sophie for her love, patience and cheer during all these years and for reminding me that work is only part of one's life.

## **VITA**

December 28, 1962 Born, Saigon, Vietnam

- 1985           Diplôme d'Ingenieur de l'Ecole Nationale Supérieure de  
Techniques Avancées, Paris, France.
- 1985           Fellowship from the Henri Kummerman Foundation,  
Geneva, Switzerland.
- 1985-1986     Scientific Attache at the Submarine Base of Toulon, France.
- 1986-         Research Assistant at the Marine Physical Laboratory of the  
Scripps Institution of Oceanography, San Diego, California.
- 1987           Ingenieur de Réserve de l'Armement.
- 1988           Master of Science in Oceanography,  
University of California, San Diego.
- 1990           Doctor of Philosophy in Oceanography,  
University of California, San Diego.

## **FIELDS OF STUDY**

Major Field: Oceanography

Studies in Underwater Acoustics.  
Professors Victor C. Anderson and William S. Hodgkiss

Studies in Digital Signal Processing and Array Processing.  
Professor William S. Hodgkiss

Studies in Instrumentation.  
Professor Fred N. Spiess

## **PUBLICATIONS**

Jean-Marie Tran, W. S. Hodgkiss, "200 Hz Matched Field Processing on the September 1987 Data Set", Fourth Matched Field Processing Workshop, Sept. 6-8, 1989, Defence Research Establishment Pacific, Victoria, B.C., Canada.

Paul Baxley, Jean-Marie Tran, "The Adverse Effects of a Mismatched Surface Layer on Matched Field Depth Discrimination", Fourth Matched Field Processing Workshop, Sept. 6-8, 1989, Defence Research Establishment Pacific, Victoria, B.C., Canada.

Jean-Marie Tran, W. S. Hodgkiss, "A Performance Study of Full Aperture and Subaperture Processing of Vertical Line Arrays with the MV Processor", Marine Physical Laboratory, Scripps Institution of Oceanography (in preparation).

Jean-Marie Tran, W. S. Hodgkiss, "Processing Real Data with the Full Aperture and Subaperture MV Beamformer", Marine Physical Laboratory, Scripps Institution of Oceanography (in preparation).

Jean-Marie Tran, W. S. Hodgkiss, "200 Hz Matched Field Processing On the September 1987 VLA Data Set", Marine Physical Laboratory, Scripps Institution of Oceanography (in preparation).

Jean-Marie Tran, W. S. Hodgkiss, "Analysis of 200 Hz CW Tone Propagation Signals Recorded during the September 1987 VLA Experiment", Marine Physical Laboratory, Scripps Institution of Oceanography (in preparation).

Jean-Marie Tran, W. S. Hodgkiss, "High Resolution Beamforming on Large Vertical Line Arrays: Processing Synthetic Data", Marine Physical Laboratory, Scripps Institution of Oceanography (in preparation).

Jean-Marie Tran, W. S. Hodgkiss, "High Resolution Beamforming on Vertical Line Arrays in a Realistic Oceanic Environment", MPL Technical Memorandum 408, Marine Physical Laboratory, Scripps Institution of Oceanography, San Diego, CA, (1989).

Jean-Marie Tran, "Broadband Spectral Estimation Using the Multiple Window Method: A Comparison with Classical Techniques", MPL Technical Memorandum 403, Marine Physical Laboratory, Scripps Institution of Oceanography, San Diego, CA, (1988).

Jean-Marie Tran, "Parabolic Equation Model", MPL Technical Memorandum 401, Marine Physical Laboratory, Scripps Institution of Oceanography, San Diego, CA, (1988).

## **ABSTRACT OF THE DISSERTATION**

Approaches to the Processing of Data from  
Large Aperture Acoustic Vertical Line Arrays

by

Jean-Marie Quoc Danh Tran  
Doctor of Philosophy in Oceanography  
University of California, San Diego, 1990  
Professor William S. Hodgkiss, Jr., Chair

This dissertation investigates various approaches to the processing of narrowband frequency data from large aperture acoustic vertical line arrays with on the order of one hundred equally spaced sensors. When little is known about the oceanic environment, beamforming is performed to detect signals and estimate the vertical arrival structure of the pressure field. The attention is focussed on using the adaptive Minimum Variance processor. The issues of signal cancellation due to correlated arrivals and mismatch due to wavefront curvature are examined. In practice, planar wavefront replica vectors do not result in significant mismatch for a 900 m aperture. Processing subapertures is proposed because of the adaptive processor requirement of having numerous data snapshots to estimate and invert the covariance matrix, while the pressure field may not be stationary. Full aperture and subaperture processing techniques are validated with simulated data created by a normal mode model, and then used on 200 Hz data collected in the North-East Pacific by the Marine Physical Laboratory in September 1987. Multipath arrivals are found to illuminate only parts of the 120 sensor array, cut for 100 Hz and 900 m long, thus indicating that the wavefield can be highly inhomogeneous with depth. The processing gain obtained with the adaptive processor is found lower than with the conventional beamformer because of the reduction of the aperture after spatial smoothing, residual signal cancellation and mismatch, but this is compensated for by a much larger resolution for high level arrivals. Beamforming simulated or real data produces a gain 6 to 7 dB lower than the array gain expected with matched field processing. Matched field processing on the real data is very successful because of their good quality, adequate knowledge of the environment, and proper acoustic modeling. The 200 Hz source is correctly localized, 165 km from the array. Array gain estimates indicate that matched field processing is a better beamforming approach for signal detection than is conventional beamforming.

## Introduction

Vertical line arrays with equally spaced sensors are systems commonly used by the scientific community as experimental tools to measure ambient noise as well as long range propagation signals [Anderson, 1974, Anderson, 1979, Kewley, 1984, Dosso, 1987, Sen, 1988, Sotirin, 1989]. At first with moderate lengths on the order of a few hundred meters, array apertures recently have been increased to provide better coverage of the water column and to enable work at lower frequencies (from tens to hundreds of Hertz). An example of a large and well filled acoustic array is the Marine Physical Laboratory (MPL) digital array, a 120 sensor aperture of 900 m cut for 100 Hz [Sotirin, 1989]. This dissertation investigates various ways to process narrowband signal data from large vertical line arrays in a realistic oceanic environment, from beamforming which theoretically requires little or only very limited knowledge of the environment to matched field processing where the environment has to be fully characterized.

The data from an array such as the MPL array are processed using spectral estimation techniques to obtain the pressure field angular spectrum and a picture of directionality. Peaks in the angular spectrum allow the identification of the direction of arrival of underwater signals with enhanced signal-to-noise ratio. The conventional beamformer is commonly used due to its computationally efficient implementation with Fast Fourier Transforms (FFTs) and its robustness. Its resolution is characterized by the ratio of the acoustic wavelength to the overall aperture length so that improvement in resolution at low frequency (or large wavelength) can only be realized with large arrays. Since feasibility and cost considerations generally put a limit on the spatial coverage, processing techniques with increased resolution capabilities are very attractive. Adaptive methods, such as the Minimum Variance processing technique [Capon, 1969], are more sophisticated and make specific assumptions on the wavefield to produce such resolution improvements at high signal-to-noise ratio. A benefit in using adaptive techniques is the ability to reject strong interferences and allow the detection of weaker signals. An increased resolution allows the separation of the multipath arrivals impinging on the vertical line array, thus making possible a detailed study of the complex propagation physics. Since the model assumptions made by the adaptive processor often do not hold in actual operation [Vural, 1979], the influence of the complex oceanic environment on the processing is addressed here. The pressure field may be strongly influenced by the sound speed profile and the ocean boundaries, since large aperture arrays have lengths on the order of the water depth. The variations of sound speed with depth result in waveguide propagation where the arrivals have curved wavefronts. The bottom and surface boundaries combined with the waveguide structure, produce multipath arrivals or spatially correlated arrivals. Another problem with the adaptive methods is their requirement for large data sample size to estimate the array covariance matrix and obtain a statistically stable estimate of the power spectrum. This can be troublesome if the field is not stationary such as in the case of a moving source.

Chapter 1 discusses the array processing hypothesis, and presents the conventional and adaptive Minimum Variance processors. The general beamforming procedure is decomposed into two components, a processing structure and a signal model which assumes uncorrelated arrivals with given wavefronts (generally planar). Implementation issues for the Minimum Variance processor are discussed. Chapter 2 investigates two aspects of sound propagation in the ocean: the problem of multipaths and wavefront curvature. The impact of these environmental factors on the conventional beamformer and the Minimum Variance processor are studied and evaluated, and correcting actions examined. Spatial smoothing techniques [Shan, 1985] are discussed and curved wavefront replica vectors, derived with a ray

geometric approach, are introduced. Using these preliminary results, two processing strategies with the Minimum Variance processor are proposed in Chapter 3 and studied through simulations. Full array aperture and array subaperture processing is envisioned with curved and planar wavefronts. The choice of the most adequate scheme is based on beamforming a 3000 m or a 900 m aperture where pressure field data at a particular frequency are generated by an acoustic normal mode model. After this validation on synthetic data, these processing techniques are used in Chapter 4 on real data, collected at sea by the MPL digital array during the September 1987 Vertical Line Array (VLA) Experiment in the North-East Pacific. 200 Hz signals are processed and their arrival structure interpreted with ray and normal mode acoustic models. Performance aspects (processing gain and resolution), are considered for various input signal-to-noise ratios in the case of the synthetic and the real data. Finally, Chapter 5 presents matched field processing which is a generalized form of beamforming where a global knowledge of the environment is required. Matched field processing is performed on the same data set as in Chapter 4. Localization and processing gain performance are examined and sources of mismatch investigated.



# 1. Array Signal Processing

## 1.1. Introduction

This chapter presents a comprehensive discussion of array processing techniques used to process the data from line arrays with equi-spaced sensors. The advantage of using an array of sensors is the spatial discrimination that it provides. The directions from which underwater signals propagate can be extracted from the measured data. After an outline of the frequency-wavenumber representation of the acoustic pressure field and its associated assumptions, the conventional beamformer is derived. Beamforming is decomposed into a signal model and a processing structure. The signal model provides a mathematical description of the propagation physics and makes assumptions on the arrival wavefronts. The function of the processing structure is to measure how close the experimental data are to a particular direction of arrival. The adaptive Minimum Variance processor is emphasized and will be used in the thesis. Its implementation is discussed and its performance summarized.

## 1.2. Basic Assumptions

Array processing methods decompose the pressure field into a directionality representation by assuming homogeneous wavefields [Yen; 1977]. A homogeneous wavefield is the superposition of uncorrelated elementary waves [Bohme; 1987]. This mathematical formulation sets a clear analogy between time series spectral estimation and array processing in its frequency-wavenumber representation of the random field [Bohme; 1987, Capon; 1969] :

$$p(t, \mathbf{r}) = \int \exp[ j ( - \omega t + \mathbf{K} \cdot \mathbf{r} ) ] dZ(\omega, \mathbf{K}) \quad (1.1)$$

where  $p$  denotes the random field at time  $t$  and spatial position  $\mathbf{r}$ ,  $\omega$  the circular frequency in rad/s and  $\mathbf{K}$  the wavenumber vector.  $dZ$  is the spectral increment of the random spectral measure  $Z(\omega, \mathbf{K})$  with covariance

$$\text{COV}[dZ(\omega, \mathbf{K})dZ(\omega', \mathbf{K}')] = \frac{1}{(2\pi)^4} \delta(\omega - \omega') \delta(\mathbf{K} - \mathbf{K}') S(\omega, \mathbf{K}) \partial\omega \partial\mathbf{K} \quad (1.2)$$

where  $\omega$  and  $\omega'$  are circular frequencies,  $\mathbf{K}$  and  $\mathbf{K}'$  wavenumber vectors,  $S$  the frequency-wavenumber spectrum of the random field  $p(t, \mathbf{r})$  and  $\delta$  the dirac delta function.

This representation is a generalization of the Cramer spectral representation for stationary time series [Priestley; 1981]. Its main assumption is that spectral increments  $dZ$  at two distinct frequencies or at two distinct wavenumber vectors are uncorrelated. It constitutes the foundation of any array processing method. Thus, this representation is one where the receiving array measures signals which result from the superposition of uncorrelated elementary waves. These elementary waves generally are assumed planar. Such a homogeneous wavefield representation is restrictive since it excludes correlated arrivals (e.g. multipaths).

## 1.3. Conventional Beamforming

Conventional beamforming on a line array with uniformly spaced sensors is a simple illustration of the already mentioned analogy with classic time series spectral estimation [Kay; 1988]. The conventional beamformer is the simplest

processing structure since it implements a linear regression on the sensor outputs, either in the time domain or in the frequency domain [Shumway; 1988].

The time domain implementation is known as delay-and-sum beamforming. A beam is formed in the time domain by summing up the lagged (delayed) outputs of the array sensors [Johnson; 1982, De Fatta; 1988]

$$y(t, \theta) = \sum_{m=0}^{M-1} a_m x_m(t - \tau_m) \quad (1.3)$$

where  $t$  denotes time,  $x_m(t)$  is the output of the  $m^{\text{th}}$  sensor,  $M$  the number of sensors,  $(a_m)_{m=0, M-1}$  the shading coefficients and  $(\tau_m)_{m=0, M-1}$  the delays associated with each sensor corresponding to a particular look direction,  $\theta$ . The time delays  $\tau_m$  are determined by making additional assumptions on the propagating signals. If one considers plane waves impinging on a line array with equally spaced sensors, the delays  $\tau_m$  are given by

$$\tau_m = \frac{m d \sin \theta}{c} \quad (1.4)$$

where  $d$  is the interelement spacing,  $c$  the sound velocity and  $\theta$  the look direction [DeFatta; 1988].

The frequency domain regression can be derived by taking the Fourier transform of the output  $y(t)$

$$Y(f, \theta) = \sum_{m=0}^{M-1} a_m e^{-j2\pi f \tau_m} X_m(f) \quad (1.5)$$

where  $f$  is the carrier frequency,  $Y(f, \theta)$  and  $X_m(f)$  the Fourier transforms of  $y(t)$  and  $x_m(t)$  respectively. In essence, Equation (1.5) is the narrow-band implementation of Equation (1.3) at the frequency  $f$ , and can also be expressed as an inner product :

$$Y(f, k) = \mathbf{A}^H \mathbf{X} \quad (1.6)$$

with

$$\mathbf{X}^T = [X_0(f) \ X_1(f) \ \cdots \ X_{M-1}(f)] \quad (1.7)$$

$$\mathbf{A}^T = [a_0 e^{j2\pi f \tau_0} \ a_1 e^{j2\pi f \tau_1} \ \cdots \ a_{M-1} e^{j2\pi f \tau_{M-1}}] \quad (1.8)$$

the superscript  $H$  denotes the Hermitian operation (complex conjugate transpose operation), and the superscript  $T$  denotes the transpose operation. Assuming plane waves, that is using Equation (1.4) and letting

$$k = \frac{f d \sin \theta}{c} \quad (1.9)$$

Equation (1.5) can be put under the form of a spatially windowed Discrete Fourier Transform [Oppenheim; 1975] :

$$Y(f, k) = \sum_{m=0}^{M-1} a_m e^{-j2\pi k m} X_m(f) \quad (1.10)$$

where  $k$  is a normalized wavenumber. The frequency-wavenumber power spectrum is estimated by the periodogram

$$I_p(f, k) = \frac{1}{\left(\sum_{i=0}^{M-1} a_i\right)^2} |Y(f, k)|^2 \quad (1.11)$$

where  $M$  is the number of sensors.  $I_p(f, k)$  can be converted into a power spectrum parametrized by the arrival angle  $\theta$  by the nonlinear mapping given in Equation (1.9) [De Fatta; 1968]. The narrow-band conventional beamformer is often implemented as a FFT beamformer [Williams; 1968]. Since it is well known that the periodogram gives an inconsistent estimate of the power spectral density [Priestley; 1981], additional incoherent averaging over successive time snapshots is typically performed. The estimate then becomes

$$P(f, k) = \frac{1}{\left(\sum_{i=0}^{M-1} a_i\right)^2} \frac{1}{K} \sum_{i=0}^{K-1} |Y_i(f, k)|^2 \quad (1.12)$$

where  $Y_i(f, k)$  is FFT beamformer output from the  $i^{\text{th}}$  time snapshot.  $P$  has a  $\chi^2$  distribution with  $2K$  degrees of freedom [Kay; 1988]. The mean and the variance of the conventional estimator are [Pillai; 1989, p. 112]

$$E(P) = \bar{P} \quad (1.13a)$$

$$\text{Var}(P) = \frac{1}{K} \bar{P}^2 \quad (1.13b)$$

where  $E$  denotes the expectation,  $\text{Var}$  the variance, and  $\bar{P}$  the power spectrum computed by the conventional processor on the expectation of the covariance matrix.

The conventional FFT beamformer directly operates on the data, and corresponds to a direct form of spectral estimation. The power spectrum can also be obtained by indirect transformation of the cross-spectral matrix based on the data [Marple; 1987]. This formulation of the conventional beamformer in terms of the array covariance matrix is now examined.

When the window applied to the aperture is the rectangular window, the  $a_i$ 's are taken equal to unity and the power spectrum can be expressed in a simplified matrix form

$$I_p(f, k) = \frac{1}{M^2} (\mathbf{E}^H \mathbf{X}) (\mathbf{E}^H \mathbf{X})^H \quad (1.14a)$$

$$= \frac{1}{M^2} \mathbf{E}^H \mathbf{X} \mathbf{X}^H \mathbf{E} \quad (1.14b)$$

where  $\mathbf{E}$  is the plane wave steering vector,

$$\mathbf{E}^T = \begin{bmatrix} 1 & e^{j2\pi k} & \dots & e^{j2\pi k(M-1)} \end{bmatrix} \quad (1.15)$$

and  $\mathbf{X} \mathbf{X}^H$  is an estimate at the frequency  $f$  of the cross spectral density matrix based on the data, or array covariance matrix. With additional averaging over time snapshots, the conventional beamformer, also called Bartlett beamformer, is given by

$$P_B(f, k) = \frac{1}{M^2} \mathbf{E}^H \mathbf{R} \mathbf{E} \quad (1.16)$$

with

$$\mathbf{R} = \frac{1}{K} \sum_{i=0}^{K-1} \mathbf{X}_i \mathbf{X}_i^H \quad (1.17)$$

where  $\mathbf{X}_i$  is the vector of Fourier coefficients corresponding to the time snapshot  $i$ .  $\mathbf{R}$  is an estimate of the array covariance matrix. When a weighting window is applied, one gets

$$P_B(f, k) = \frac{1}{M^2} \mathbf{E}^H \mathbf{W}^H \mathbf{R} \mathbf{W} \mathbf{E} \quad (1.18)$$

where the  $(M, M)$  real diagonal matrix  $\mathbf{W}$  is

$$\mathbf{W}^T = \frac{1}{\frac{1}{M} \sum_{i=0}^{M-1} a_i} \begin{pmatrix} a_0 & 0 & \cdots & 0 \\ 0 & a_1 & \cdots & . \\ . & . & \cdots & . \\ . & . & \cdots & . \\ . & . & \cdots & 0 \\ 0 & 0 & \cdots & a_{M-1} \end{pmatrix} \quad (1.19)$$

#### 1.4. Matched Filter Interpretation of Beamforming

This indirect formulation of the conventional beamformer in terms of the array covariance matrix allows the decomposition of the processing into two components: a processor and a set of steering vectors.

For a given set of replica vectors, finding an arrival corresponds to finding a peak in the processor output. Therefore, the processing can be interpreted as spatial matched filtering. Using Equation (1.14), the quantity to be maximized in order to find an arrival or a signal, is given by

$$\mathbf{E}^H \mathbf{X} \mathbf{X}^H \mathbf{E} = |\mathbf{E}^H \mathbf{X}|^2 \quad (1.20)$$

where  $\mathbf{E}$  is a direction vector (given by Equation (1.15)) corresponding to an arrival angle  $\theta$ .  $\mathbf{E}$  is a steering vector or replica vector from a set often called array manifold [Schmidt; 1981, Clarke; 1988] which contains the true underlying arrival wavefronts. Generally, the plane wave array manifold is selected.

If a single signal impinges on the array at a given but unknown angle of arrival, the measured array signal vector  $\mathbf{X}$  given by Equation (1.7) will be an amplitude weighted plane wavefront vector. From the Schwartz inequality the output of the processor will be maximum if the replica vector  $\mathbf{E}$  and the array signal vector  $\mathbf{X}$  are colinear. The processor provides a measure of the mismatch between the observed field and a replica vector or steering vector. A match implies a high output and an arrival [Cox; 1973].

Most of the emphasis in the array processing community has been on the choice of a best processing structure and has lead to the development of various techniques besides conventional beamforming, such as adaptive methods, approaches based on auto-regressive models, and principle component techniques [Pillai; 1989]. All these advanced processing schemes operate on the array covariance matrix and have their own advantages and disadvantages related to performance criteria such as resolution, processing complexity, stability. In particular, the adaptive Minimum Variance method [Capon; 1969] has received much attention in the underwater acoustics community and will be studied later in this chapter and used throughout this thesis. The propagation physics play a minor role in conventional beamforming since it is incorporated through a simple signal model and the selection of planar wavefronts. This underlying signal model is now studied.

### 1.5. Signal Model Definition

If  $p$  narrowband signals at the carrier frequency  $f$  impinge on the array, the time domain array signal vector at the input of the beamformer is given by [Cox; 1973, De Graaf; 1985]

$$\mathbf{r}(t) = \mathbf{B} \mathbf{s}(t) + \mathbf{n}(t) \quad (1.21)$$

where  $\mathbf{s}(t)$  is the  $(p,1)$  signal vector, sometimes called the envelope vector [Cadzow; 1988],  $\mathbf{n}(t)$  is the  $(M,1)$  vector of additive noise and  $\mathbf{B}$  the matrix of stacked directions with columns equal to

$$\mathbf{B} = [\mathbf{d}_0 \ \mathbf{d}_1 \ \cdots \ \mathbf{d}_{p-1}] \quad (1.22)$$

each  $(M,1)$  column vector  $\mathbf{d}_j$  corresponds to an arrival angle  $\theta_j$ . The equivalent narrow-band frequency domain representation is, at the signal carrier frequency  $f$ ,

$$\mathbf{r} = \mathbf{B} \mathbf{s} + \mathbf{n} \quad (1.23)$$

where  $\mathbf{s}$  is the  $(p,1)$  signal vector,  $\mathbf{n}$  is the additive noise  $(M,1)$  vector, and  $\mathbf{B}$  the matrix of stacked directions. The corresponding model covariance matrix  $\mathbf{R}_{model} = \mathbf{r} \mathbf{r}^H$  is thus

$$\mathbf{R}_{model} = \mathbf{B} \mathbf{S} \mathbf{B}^H + \mathbf{Q} \quad (1.24)$$

where  $\mathbf{S}$  is the  $(p,p)$  signal covariance matrix given by  $E(\mathbf{s} \mathbf{s}^H)$  and  $\mathbf{Q}$  is the noise covariance matrix given by  $E(\mathbf{n} \mathbf{n}^H)$  with  $E$  denoting the expectation.

Under the assumption of a homogeneous wavefield, the signals are uncorrelated, and the  $(p,p)$  signal matrix  $\mathbf{S}$  is diagonal of full rank  $p$ . Recalling that  $\mathbf{S} = E(\mathbf{s} \mathbf{s}^H)$  with  $\mathbf{s}^T = [s_0 \ s_1 \ \cdots \ s_{p-1}]$ , uncorrelated arrivals means that the signal envelopes are such that, for  $i \neq j$ ,

$$E(s_i s_j^*) = 0 \quad (1.25)$$

where  $*$  denotes the complex conjugate operation. If  $s_i$  and  $s_j$  are correlated, then

$$E(s_i s_j^*) \neq 0 \quad (1.26)$$

Restricting the discussion to two arrivals, the signal covariance matrix is

$$\mathbf{S} = \begin{bmatrix} E(s_0 s_0^*) & E(s_0 s_1^*) \\ E(s_1 s_0^*) & E(s_1 s_1^*) \end{bmatrix} \quad (1.27)$$

with  $E(s_i s_i^*) = \sigma_i^2$ , the power of the  $i^{th}$  signal, and for  $i \neq j$ ,  $E(s_i s_j^*) = \sigma_i \sigma_j \rho_{i,j}$ , where  $\rho_{i,j} = \rho_{j,i}^*$  is the complex correlation given by

$$\rho_{i,j} = \frac{E(s_i s_j^*)}{E(|s_i|^2)E(|s_j|^2)} \quad (1.28)$$

Then, the signal covariance matrix  $\mathbf{S}$  can be written [Reddy; 1987]

$$\mathbf{S} = \begin{bmatrix} \sigma_0^2 & \sigma_0 \sigma_1 \rho \\ \sigma_0 \sigma_1 \rho^* & \sigma_1^2 \end{bmatrix} \quad (1.29)$$

For fully correlated arrivals  $|\rho| = 1$ , hence  $\det \mathbf{S} = \sigma_0^2 \sigma_1^2 (1 - |\rho|^2) = 0$ . Fully correlated arrivals are called coherent arrivals [Pillai; 1989, p. 10].

The standard model for the noise covariance  $\mathbf{Q}$  is a sensor noise uncorrelated from sensor to sensor [Nickel; 1988, Schmidt; 1986]. Under this assumption, the noise covariance matrix is  $\mathbf{Q} = \sigma_n^2 \mathbf{I}$ , where  $\sigma_n^2$  is the noise power and  $\mathbf{I}$  the identity matrix. It follows that the  $(M, M)$  covariance matrix  $\mathbf{R}_{model}$  is of full rank.

Furthermore, if one assumes the elementary waves of the field to be planar, the covariance matrix  $\mathbf{R}_{model}$ , which is Hermitian by construction (i.e.  $\mathbf{R}_{model}^H = \mathbf{R}_{model}$ ), also is Toeplitz (constant along the diagonals).

$$\mathbf{R}_{model} = \sigma_0^2 \mathbf{d}_0 \mathbf{d}_0^H + \sigma_1^2 \mathbf{d}_1 \mathbf{d}_1^H + \dots + \sigma_{p-1}^2 \mathbf{d}_{p-1} \mathbf{d}_{p-1}^H + \sigma_n^2 \mathbf{I} \quad (1.30)$$

Since  $\mathbf{d}_i = [1 \ e^{j2\pi k_i} \ e^{j2\pi 2k_i} \ \dots \ e^{j2\pi(M-1)k_i}]$ , each outer product in the sum given by Equation (1.30) is Toeplitz :

$$\mathbf{d}_i \mathbf{d}_i^H = \begin{bmatrix} 1 & e^{-j2\pi k_i} & e^{-j2\pi 2k_i} & \dots & e^{-j2\pi(M-1)k_i} \\ e^{j2\pi k_i} & 1 & e^{-j2\pi k_i} & \dots & . \\ . & . & 1 & \dots & . \\ . & . & . & \dots & . \\ e^{j2\pi(M-1)k_i} & e^{j2\pi(M-2)k_i} & . & \dots & 1 \end{bmatrix} \quad (1.31)$$

so that  $\mathbf{R}_{model}$  is both Toeplitz and Hermitian. The Toeplitz character of the array covariance matrix is a result of the duality between homogeneous plane wavefields and wide sense stationary time series.

## 1.6. Adaptive Beamforming

The narrow-band beamforming problem can be viewed as finding a set of complex weights or, equivalently, a steering vector given by Equation (1.15) [De Graaf; 1985] corresponding to the signal direction of arrival. The conventional processor (which assumes plane waves) is the most widely used, the best known and the most robust, but has the least resolution. Since only limited sampling in space can be achieved at a reasonable cost, an important performance criteria is resolution. Data adaptive techniques, which are described in what follows, are used to meet this design requirement. They make full use of the information summarized in the covariance matrix, using the signal model described in the previous paragraph.

### 1.6.1. Optimum versus Adaptive Processing

Optimum signal processing derives optimal processors based on completely known covariance matrices [Orfanidis, 1988]. It assumes that all the entries in the signal model given by Equation (1.24) are perfectly known, in particular the noise covariance matrix  $\mathbf{Q}$ . Adaptive arrays which find multiple applications in RADAR or active SONAR [Brennan; 1973], solve the problem of detecting a signal in a "primary sample" based on a signal-free or noise-only "secondary sample" [Kelly; 1989]. The secondary samples allow the estimation of the noise covariance matrix  $\mathbf{Q}$ , which is used to compute the optimal set of weights which maximizes the output signal-to-noise ratio, given a particular direction of look  $\mathbf{E}$  [Cox; 1973]:

$$\mathbf{W} = \frac{\mathbf{Q}^{-1} \mathbf{E}}{\mathbf{E}^H \mathbf{Q}^{-1} \mathbf{E}} \quad (1.32)$$

The processor using those weights has been normalized to yield unity response with zero phase shift in the look direction  $\mathbf{E}$  [Cox; 1987]. In adaptive arrays, the

look direction  $\mathbf{E}$  is called unadapted beam or quiescent beam. The output power produced by the processor is given by

$$P_{processor} = \mathbf{W}^H \mathbf{R} \mathbf{W} \quad (1.33)$$

In the context of passive SONAR, the noise field includes all "unwanted" signals and the noise covariance matrix  $\mathbf{Q}$  is not known. Then, the optimum processor is implemented by an adaptive processor which uses estimate of the array covariance [Cox; 1987] (since the noise covariance matrix is not known, the estimate of the whole array covariance  $\mathbf{R}$  is used instead of the noise-only covariance matrix  $\mathbf{Q}$ ). Then, the adaptive processor is obtained by using the weight

$$\mathbf{W} = \frac{\mathbf{R}^{-1} \mathbf{E}}{\mathbf{E}^H \mathbf{R}^{-1} \mathbf{E}} \quad (1.34)$$

and is the well known Minimum Variance Distorsionless Response (MVDR) beamformer [Zoltowski; 1988]. This adaptive processor is called the Minimum Variance (MV) processor in this thesis. It was originally called Maximum Likelihood Method (MLM) [Capon; 1969] because it was shown to be the maximum likelihood estimator in the case of Gaussian noise (i.e. it minimizes the log-likelihood under the assumption of Gaussian statistics). The MV processor is also called the Minimum Energy processor in [De Graaf; 1985]. This adaptive beamformer determines a data dependent set of weights as the solution of a constrained optimization problem [Griffiths; 1977, Monzingo; 1985, Van Veen; 1988]. The MV processor, classically, is derived by minimizing the output power of the adaptive spatial filter subject to the constraint of passing the on-look direction undistorted [Lacoss; 1971, Cox; 1973, Kanasewich; 1975, Marple; 1987] :

$$\text{MIN} \left[ \mathbf{W}^H \mathbf{R} \mathbf{W} \right]_{\mathbf{E}^H \mathbf{W} = 1} \quad (1.35)$$

where  $\mathbf{W}$  is the unknown weight vector,  $\mathbf{E}$  the look of direction vector or replica vector from the array manifold and  $\mathbf{R}$  the cross-spectral density matrix, estimated from the data and given by Equation (1.17). As before, one assumes that the data have been Fourier analysed and a single frequency  $f$  is considered. The weight vector  $\mathbf{W}$  can be derived by using the Lagrange's multiplier method [Lacoss; 1971, Kanasewitch; 1975, Marple; 1987] and is given by Equation (1.34). The corresponding power spectrum is

$$P_{MV}(f, k) = \frac{1}{\mathbf{E}^H \mathbf{R}^{-1} \mathbf{E}} \quad (1.36)$$

As stated earlier, this processor also maximizes the output signal-to-noise ratio and the array gain (the output signal-to-noise ratio in the beam divided by the signal-to-noise ratio at a sensor) [Gammelsaeter; 1980]. If

$$\mathbf{R} = \sigma_s^2 \mathbf{d} \mathbf{d}^H + \mathbf{Q} \quad (1.37)$$

where  $\sigma_s^2$  is the signal power and  $\mathbf{d}$  the signal direction vector (normalized to unit norm), the array gain is given by

$$G = \left( \frac{\sigma_s^2 \mathbf{W}^H \mathbf{d} \mathbf{d}^H \mathbf{W}}{\mathbf{W}^H \mathbf{Q} \mathbf{W}} \right) / \left( \frac{\sigma_s^2}{q_{11}} \right) \quad (1.38)$$

where  $q_{11}$  is the (1,1) term of the noise covariance matrix  $\mathbf{Q}$ . Then,

$$G = \frac{q_{11} (\mathbf{W}^H \mathbf{d} \mathbf{d}^H \mathbf{W})}{\mathbf{W}^H \mathbf{Q} \mathbf{W}} \quad (1.39)$$

which can be transformed into

$$G = (r_{11} - \sigma_s^2) \frac{\mathbf{W}^H \mathbf{d} \mathbf{d}^H \mathbf{W}}{\mathbf{W}^H \mathbf{R} \mathbf{W} - \sigma_s^2 \mathbf{W}^H \mathbf{d} \mathbf{d}^H \mathbf{W}} \quad (1.40)$$

It is evident from Equations 1.39 and 1.40 that maximizing the array gain  $G$  is equivalent to minimizing  $\mathbf{W}^H \mathbf{Q} \mathbf{W}$  or minimizing  $\mathbf{W}^H \mathbf{R} \mathbf{W}$  if one constrains  $\mathbf{W}^H \mathbf{d}$  to unity.

Assuming the signal model of Equation (1.37) and spatially white noise i.e.  $\mathbf{Q} = \sigma_n^2 \mathbf{I}$ , the MV power spectrum can be expressed as

$$P_{MV} = \frac{1}{M} \frac{\sigma_n^2 (1 + \frac{\sigma_n^2}{\sigma_s^2})}{1 + \frac{\sigma_n^2}{\sigma_s^2} - \frac{1}{M} |\mathbf{E}^H \mathbf{d}|^2} \quad (1.41)$$

using the matrix inversion lemma [Kay; 1988, p. 24]. If there is no mismatch,  $\mathbf{E}$  corresponds to the signal direction and  $\frac{1}{M} |\mathbf{E}^H \mathbf{d}| = 1$  so that  $P_{MV} = \frac{1}{M} (\sigma_s^2 + \sigma_n^2)$ . It is identical to the output of the conventional processor under the same assumptions since  $P_B = \frac{1}{M^2} \mathbf{E}^H \mathbf{R} \mathbf{E} = \frac{1}{M} [\sigma_s^2 \frac{1}{M} |\mathbf{E}^H \mathbf{d}|^2 + \sigma_n^2]$ . Similarly, in a noise direction  $\mathbf{E}^H \mathbf{d}$  is small so  $P_{MV}$  and  $P_B$  are close to  $\frac{1}{M} \sigma_n^2$ .

The MV processor stands as a "high resolution" method compared to the conventional FFT beamformer. This statement is proven by showing that  $P_{MV} \leq P_B$  [Pillai; 1989]. The covariance matrix  $\mathbf{R}$  is Hermitian ( $\mathbf{R}^H = \mathbf{R}$ ), and can be decomposed according to the spectral theorem [Golub; 1985] as

$$\mathbf{R} = \mathbf{Q}^H \mathbf{D} \mathbf{Q} \quad (1.42)$$

where  $\mathbf{Q}$  is unitary (i.e.  $\mathbf{Q}^H \mathbf{Q} = \mathbf{I}$ , where  $\mathbf{I}$  is the identity matrix), and  $\mathbf{D}$  is a diagonal real matrix. The covariance matrix can also be put under the form

$$\mathbf{R} = (\mathbf{D}^{1/2} \mathbf{Q})^H \mathbf{D}^{1/2} \mathbf{Q} = (\mathbf{R}^{1/2})^H \mathbf{R}^{1/2} \quad (1.43)$$

Assume the steering vector  $\mathbf{e}$  normalized such that  $\mathbf{e}^H \mathbf{e} = 1$ , the unit norm relation can be expressed as

$$\mathbf{e}^H \mathbf{R}^{1/2} \mathbf{R}^{-1/2} \mathbf{e} = 1 \quad (1.44)$$

which is a vector inner-product between two vectors  $\mathbf{u} = (\mathbf{R}^{1/2})^H \mathbf{e}$  and  $\mathbf{v} = \mathbf{R}^{-1/2} \mathbf{e}$ . Using the Schwarz inequality  $\mathbf{u}^H \mathbf{v} \leq \mathbf{u}^H \mathbf{u} \mathbf{v}^H \mathbf{v}$  and

$$\mathbf{u}^H \mathbf{u} = \mathbf{e}^H \mathbf{R} \mathbf{e} \quad (1.45a)$$

$$\mathbf{v}^H \mathbf{v} = \mathbf{e}^H \mathbf{R}^{-1} \mathbf{e} \quad (1.45b)$$

one obtains the inequality [Pillai; 1989, p. 20]

$$\frac{1}{\mathbf{e}^H \mathbf{R}^{-1} \mathbf{e}} \leq \mathbf{e}^H \mathbf{R} \mathbf{e} \quad (1.46)$$

so that, while the MV processor reports the same peak levels as the conventional Bartlett processor, it has a better resolving power in general. That is why the MV estimator is called a "high resolution" method and is used in various areas such as the seismic field [Capon; 1969, Baggeroer; 1974, Baggeroer; 1982, Hsu; 1986], the oceanographic field [Oltman-shay; 1984] as well as the underwater acoustics arena [Owsley; 1985].



### 1.6.2. Behaviour of the MV Beamformer

The behaviour of the MV beamformer has been studied rather extensively [Cox; 1973, De Graaf; 1985] and only general performance trends are presented here. For the adaptive array pointing in a given direction, the signal arriving in another direction is an interference to be cancelled. The stronger the interference, the more suppression the designed filter is able to put on it. This suppression, based on the covariance structure across the array, depends on the signal-to-noise ratio. In the context of matched filtering, the MV processor is such that a slight mismatch in the replica vector results in serious reduction of its output, in the case of a high signal-to-noise ratio environment [Cox; 1973]. This high sensitivity to mismatch can cause problems, for instance, when an insufficient number of look directions is used or if the array manifold is chosen with improper assumptions about the true underlying wavefronts. Sensitivity to mismatch also means that any kind of errors (such as gain or phase errors in the analog processing chain of each sensor or such as sensor position) will degrade the performance of the adaptive processor to a large extent. Then, the MV beamformer breaks down and its resolving capability can be less than that of the conventional processor [Seglison; 1970, McDonough; 1972]. As a result of this sensitivity to mismatch, resolution is highly dependent on signal-to-noise ratio, and is high for high signal-to-noise ratios. For instance, the MV resolution for a line array receiving two signals with 30 dB output signal-to-noise ratio is slightly over three times the Rayleigh resolution of conventional processor [Cox; 1973] which is given in radians by [Burdic; 1984]

$$\theta = \frac{\lambda}{L} \quad (1.47)$$

where  $\lambda$  is the acoustic wavelength and  $L$  is the length of the array. At low signal-to-noise ratio, the sensitivity to mismatch of the MV processor decreases and the resolution of the adaptive processor becomes comparable to the conventional processor resolution [Cox; 1973, Kanasewich; 1975, Zoltowski; 1988].

### 1.6.3. Implementation Issues

The MV beamformer is a more complicated processing structure than the conventional processor and, to obtain the power spectrum, requires the estimation of the narrowband covariance matrix based on the data and its inversion

#### 1.6.3.1. Estimating the Covariance Matrix

The problem of estimating the covariance matrix is avoided by the conventional FFT beamformer. Since the MV processor requires the inversion of the covariance matrix, a requirement is to work with a nonsingular covariance matrix. Thus, in Equation (1.17), one must average at least as many dyad products as sensors, otherwise the covariance matrix theoretically is singular and non-invertible. The way one estimates the covariance matrix has some impact on the final power spectrum.

This issue has been addressed by the adaptive array community, and the literature provides guidelines on how the covariance matrix should be estimated. These guidelines, derived for the noise covariance matrix  $\mathbf{Q}$ , immediately apply for the full array covariance matrix  $\mathbf{R}$ , since in the context of passive SONAR, noise cannot be differentiated from signals. As already stated by Equation (1.17), the noise covariance matrix is estimated by averaging dyad vectors

$$\hat{\mathbf{Q}} = \frac{1}{K} \sum_{i=0}^{K-1} \mathbf{x}_i \mathbf{x}_i^H \quad (1.48)$$

where  $\mathbf{X}_i$  is a complex sample vector of the  $M$  sensor outputs corresponding to the frequency  $f$ .  $K$  is the number of snapshots such that  $K \geq M$ . It is assumed that the sensor outputs  $\mathbf{X}_i$  are independent multidimensional complex Gaussian random vectors with probability density function given by

$$f_{\mathbf{X}}(\mathbf{X}_i) = \frac{1}{\pi \det \mathbf{Q}} \exp \left( -\mathbf{X}_i^H \mathbf{Q}^{-1} \mathbf{X}_i \right) \quad (1.49)$$

where the noise covariance matrix  $\mathbf{Q}$  is Hermitian positive definite and  $\det \mathbf{Q}$  is the determinant of  $\mathbf{Q}$ . It is well known [Goodman; 1963] that the estimator given in Equation (1.17) or (1.48) is the maximum likelihood estimator based on the data. That is, it maximizes the log likelihood function,  $\ln L$ , where  $L$  is the joint probability of the  $K$  independent random vectors  $(\mathbf{X}_i)_{i=0, K-1}$ . The distribution of the covariance matrix estimate is a complex Wishart distribution [Goodman; 1963]. Based on this result, it has been shown [Reed; 1974] that the adaptive signal-to-interference-plus-noise ratio achieved with the weights  $\hat{\mathbf{W}} = k \hat{\mathbf{Q}}^{-1} \mathbf{E}$  (where  $k$  is a complex number, in our discussion  $k = 1/(\mathbf{E}^H \hat{\mathbf{Q}}^{-1} \mathbf{E})$ ) approaches the optimum one (where  $\mathbf{Q}$  is assumed known) by a normalized signal-to-noise ratio  $\rho$  with expected value given by

$$E(\rho) = \frac{K + 2 - M}{K + 1} \quad (1.50)$$

Equation (1.50) leads to the useful rule of thumb that one must average a number of dyads equal to twice the number of sensors to compute the covariance matrix in order to maintain an average loss ratio of 3 dB. The analysis is developed further in [Boroson; 1980] where it is pointed out that a larger number of averages is required to insure a certain probability of having a reduction in signal-to-noise ratio below 3 dB (the examples given in [Boroson; 1980] are  $K \geq 3M$  to ensure that the probability  $P(\rho \geq 3 \text{ dB}) \leq 0.0196$ , and  $K \geq 4M$  to ensure that the probability  $P(\rho \geq 3 \text{ dB}) \leq 0.0032$ ).

It noted in [Gabriel; 1980, Hudson; 1980] that averaging over only a few snapshots, still, can lead to an adaptive filter with good interference rejection capabilities, but with a distorted beampattern. The asymptotic sidelobe level of the adaptive filter is given by  $\frac{1}{K+1}$  [Kelly; 1989]. If the noise plus interference field is composed of only a few interferences with power levels well above the noise background, the covariance matrix  $\mathbf{R}$  will have a large spread in eigenvalues and therefore will be poorly conditioned and, in fact, intrinsically singular [Hudson; 1981, p. 136]. In this case, the amount of averaging required to estimate the covariance matrix can be relaxed to twice the number of strong interferences [Hudson; 1981, p. 123]. Even with few averages, virtually perfect nulling can be achieved: the sample covariance matrix is rendered invertible by augmenting its diagonal by a supplement  $\epsilon$  [Capon; 1969, Hudson; 1981, Carlson; 1988].

The number of snapshots entering in the estimation of the array covariance matrix controls how well the covariance matrix is estimated, thus the bias and variance of the MV estimator. Based on the distribution of the covariance matrix estimate, the MV power spectrum has been shown in [Capon; 1970] to have a  $\chi^2$  distribution with a number of degrees of freedom equal to  $2(K-M+1)$  where  $K$  is the number of snapshots and  $M$  the number of sensors. The MV power spectrum estimator has a mean and a variance given by [Pillai; 1989, p. 112]

$$E(P_{MV}) = \frac{K - M + 1}{K} \bar{p} \quad (1.51a)$$

$$\text{Var}(P_{MV}) = \frac{K - M + 1}{K^2} \bar{p}^2 \quad (1.51b)$$

where  $\bar{P}$  the power spectrum computed by the MV processor on the expectation of the covariance matrix. Therefore, the MV estimator is biased by

$$\text{bias}(dB) = 10 \log \frac{K - M + 1}{K} \quad (1.52)$$

Furthermore, one observes that the adaptive processor requires a large number of snapshots compared to the conventional processor in order to achieve statistical stability, especially for large number of sensors.

### 1.6.3.2. Inverting the Covariance Matrix

The possibility of handling an ill-conditioned covariance matrix was mentioned in the previous Section. This problem is now addressed. Two treatments of singular or nearly singular matrices are proposed in the literature. One uses the pseudo-inverse instead of the true inverse (which in the worst case does not exist) and the other stabilizes the covariance matrix.

#### Using the Pseudo-Inverse

The pseudo-inverse (also called Moore-Penrose inverse [Penrose; 1985]) of a  $M$  sensor array covariance matrix  $\mathbf{R}$ , with  $k < M$  non zero eigenvalues, is defined as

$$\mathbf{R}^+ = \sum_{n=1}^k \lambda_n^{-1} \mathbf{e}_n \mathbf{e}_n^H \quad (1.53)$$

where  $\lambda_n$  and  $\mathbf{e}_n$  are the eigenvalues and eigenvectors of  $\mathbf{R}$ . If  $\mathbf{R}$  is of full rank (i.e.  $k = M$ ) then, the pseudo-inverse corresponds to the true inverse  $\mathbf{R}^+ = \mathbf{R}^{-1}$ . The use of the pseudo-inverse is considered in [Hudson; 1981, pp 142-143] for the case where only  $k$  dyad products are used to estimate the covariance matrix in an adaptive array context. Since  $\mathbf{W}$  is proportional to  $\mathbf{R}^{-1} \mathbf{E}$ , the weight vector belongs to the span of eigenvectors of  $\mathbf{R}$  with smallest eigenvalues which tends to be orthogonal to the span of eigenvectors of  $\mathbf{R}$  with largest eigenvalues (those correspond to the interferences). If  $\lambda_1 > \lambda_2 > \dots > \lambda_M$ , then the dominant term in the pseudo-inverse will be  $\lambda_M^{-1} \mathbf{e}_M \mathbf{e}_M^H$ ,  $\lambda_{M-1}^{-1} \mathbf{e}_{M-1} \mathbf{e}_{M-1}^H$ ,  $\dots$ , and so on.

It is shown in [Hung; 1983] through theoretical derivations and simulations that using the pseudo-inverse can lead to misleading results. The theoretical reason is that for a matrix whose smallest eigenvalues are very close to zero, the pseudo-inverse (which in practice does not keep those near zero eigenvalues) actually does not keep the dominant terms which appear in the inverse of the covariance matrix. Thus the weight vector  $\mathbf{W}$  is chosen in a vector space which does not include the dominant null-eigenvalue vector space.

#### Using White Noise Stabilization

In contrast, the white noise stabilization procedure retains those dominant terms which enter into the true inverse  $\mathbf{R}^{-1}$ ,

$$\mathbf{R} + \epsilon \mathbf{I} = \sum_{i=1}^k (\lambda_i + \epsilon) \mathbf{e}_i \mathbf{e}_i^H + \sum_{i=k+1}^M \epsilon \mathbf{e}_i \mathbf{e}_i^H \quad (1.54)$$

$$(\mathbf{R} + \epsilon \mathbf{I})^{-1} = \sum_{i=1}^k (\lambda_i + \epsilon)^{-1} \mathbf{e}_i \mathbf{e}_i^H + \sum_{i=k+1}^M \epsilon^{-1} \mathbf{e}_i \mathbf{e}_i^H \quad (1.55)$$

so that even if a slightly incorrect weighting of the various directions is performed, the optimum weight vector  $\mathbf{W}$  is drawn from the subspace of the null eigenvalues of

$\mathbf{R}$  [Hudson; 1981, p. 141].

The idea of stabilizing the covariance matrix was introduced early on by Capon [Capon; 1969]. The condition number of the matrix, which is defined as

$$c = \frac{\lambda_{\min}}{\lambda_{\max}} \quad (1.56)$$

where  $\lambda_{\min}$  and  $\lambda_{\max}$  are respectively the minimum and maximum eigenvalue of the array covariance matrix, provides a convenient criterion for the matrix invertibility (based on the eigenvalue spread). The matrix can be easily inverted if

$$c \geq c_0 \quad (1.57)$$

where  $c_0$  is typically on the order of  $10^{-6}$ .

Several stabilization schemes have been proposed. One employs the knowledge of the extrema eigenvalues of  $\mathbf{R}$  [Lunde; 1976] and uses as stabilization, if  $c < c_0$ :

$$\epsilon = \lambda_{\max} c_0 - \lambda_{\min} \quad (1.58)$$

if  $c \geq c_0$ , then no stabilization is needed and  $\epsilon = 0$ . Another scheme, which requires less computation and is more commonly used, is to add to the main diagonal of  $\mathbf{R}$

$$\epsilon = \gamma \frac{\text{tr}(\mathbf{R})}{M} \quad (1.59)$$

where  $\gamma$  is a free parameter called fraction of noise with typical values between  $10^{-3}$  and  $10^{-1}$ , and  $\text{tr}$  is the trace operator. This procedure of stabilizing the covariance matrix with spatially white noise is also called the "pseudonoise addition technique" [Gabriel; 1980, Takao; 1986], or "diagonal loading" [Carlson; 1988]. This stabilization scheme will be used in this thesis. In addition to allowing or facilitating the matrix inversion, diagonal loading can be shown to increase the robustness of the adaptive processor although there is a trade-off since stabilization is equivalent to an increase of the noise power. Using a stabilization factor  $\gamma$  of 0.001 corresponds to introducing in the system an uncorrelated sensor noise 30 dB below the average sensor power level. Thus, the MV angular spectrum is biased by the amount

$$\text{Bias(dB)} = 10 \log \frac{\mathbf{E}^H \mathbf{R}^{-1} \mathbf{E}}{\mathbf{E}^H (\mathbf{R} + \epsilon \mathbf{I})^{-1} \mathbf{E}} \quad (1.60)$$

Furthermore, the general statistics of the stabilized covariance matrix is not known, nor is the statistics of the corresponding MV estimator [Baggeroer; 1988]. The trade-off associated with the covariance matrix stabilization has been studied in [Carlson; 1988]. By adding noise in the system, one effectively reduces the adaptive filter nulling capabilities against the weak interferences which have small eigenvalues. While excessive loading can result in unacceptable performance degradation, a low level of stabilization is known to greatly improve the performance of adaptive arrays. The various interpretations of the stabilization procedure, given in the literature to explain the performance improvement, are now presented.

If one uses  $\mathbf{R}' = \mathbf{R} + \epsilon \mathbf{I}$  (where  $\epsilon$  is a free parameter), instead of  $\mathbf{R}$  in the derivation of the MV processor, one does actually maximize with respect to  $\mathbf{W}$  the following Lagrangian functional

$$\Lambda(\mathbf{W}) = \mathbf{W}^H \mathbf{R}' \mathbf{W} + \lambda(\mathbf{W}^H \mathbf{E} - 1) \quad (1.61)$$

which, in terms of  $\mathbf{R}$  can be expressed as

$$\Lambda(\mathbf{W}) = \mathbf{W}^H \mathbf{R} \mathbf{W} + \lambda(\mathbf{W}^H \mathbf{E} - 1) + \epsilon \mathbf{W}^H \mathbf{W} \quad (1.62)$$

where  $\lambda$  is a Lagrange multiplier [Gabriel; 1980, Takao; 1986].  $\epsilon$  which depends on the average power across the array (c.f. Equation (1.59)) is independent of the look direction and is not a true Lagrange multiplier. Then, the stabilization procedure is interpreted as adding a "constraint" on the weight vector norm. Adding a constraint on the adaptive weight vector norm has been proposed to increase the robustness of the MV processor [Maksym; 1979]. Large weights are characteristic of superdirectivity conditions where an interference is close to the look direction. This robust version of the MV is also called the Bounded Weight Vector Norm Method (BNX) [Verlardo; 1989]. Note that stabilizing the covariance matrix and performing the Minimum Variance calculation is different from using the BNX processor for which in Equation (1.62), both  $\lambda$  and  $\epsilon$  would be Lagrange multipliers.

The additional "constraint" on the adaptive weights, which corresponds to the covariance matrix stabilization, can be also transposed in the dual optimization problem that the MV processor solves. This dual problem is the maximization of the array gain [Gammelsaeter; 1980] and the stabilization "constraint" is set on the white noise gain [Cox; 1987]. The white noise gain is obtained by setting  $\mathbf{Q} = \sigma_n^2 \mathbf{I}$  in Equation (1.37)

$$G_w = \frac{|\mathbf{W}^H \mathbf{d}|^2}{\mathbf{W}^H \mathbf{W}} \quad (1.63)$$

where  $\mathbf{d}$  is the signal direction defined in Equation (1.37). Although there is not a simple direct relationship between the amount of stabilization  $\epsilon$  and the constraint on the white noise gain  $G_w$  [Cox; 1987], this provides an interesting interpretation of the covariance matrix stabilization in terms of processor robustness. Mismatch can be expressed as a random perturbation in the covariance matrix. Denoting the perturbation matrix by  $\eta \mathbf{P}$ , the signal model of Equation (1.37) becomes

$$\mathbf{R} = \sigma_s^2 \mathbf{d} \mathbf{d}^H + \eta \mathbf{P} + \mathbf{Q} \quad (1.64)$$

and the robustness of the processor can be measured by the fractional sensitivity of the array gain to the mismatch or the perturbation matrix  $\eta \mathbf{P}$ . Defining the fractional sensitivity of the array gain as [Cox; 1987]:

$$S = \frac{(dG/d\eta)}{G} \quad (1.65)$$

one can show that

$$S = \frac{\mathbf{W}^H \mathbf{P} \mathbf{W}}{|\mathbf{W}^H \mathbf{d}|^2} \quad (1.66)$$

which is precisely the reciprocal of the array gain against noise with covariance matrix  $\mathbf{P}$ . When  $\mathbf{P} = \mathbf{I}$ ,  $S$  is the reciprocal of the white noise gain given in Equation (1.63). This shows that diagonal loading actually increases the robustness of the MV processor to errors which are uncorrelated from sensor to sensor.

## 1.7. Conclusions

In this chapter, the general concepts of array processing have been outlined. Beamforming has been decomposed into two parts: a processing structure and a signal model. The signal model provides the general framework that characterizes the physical environment. The processing structure is used to decide whether or not a particular arrival is received by the line array. The adaptive Minimum Variance processor which can provide more resolution than the conventional beamformer is emphasized and will be used in the rest of the dissertation.

## **2. Beamforming in a Realistic Environment**

### **2.1. Introduction**

In Chapter 1, a simple signal model was introduced where the pressure field is the superposition of uncorrelated plane wave arrivals. This chapter deals with a more realistic and more complex description of the underwater medium sampled by a vertical line array. The effects of the water column boundaries and the variations of the index of refraction with depth are now studied. The surface and bottom boundaries produce multipath propagation or correlated arrivals across the receiving array. The resulting covariance matrix is not Toeplitz as in the original signal model assuming planar wavefronts. The MV processor is well known to fail in this scenario and requires some pre-processing, which, in order to remove spatial correlation, consists in averaging over space. Spatial smoothing is a necessary processing step before using the adaptive processor, although it reduces the aperture length (thus the resolution) and increases the computational burden. Then, the effect of a variable sound speed with depth is examined. The sound speed profile produces a waveguide propagation, where the arrivals impinging on a vertical array are not planar but curved. The effect of wavefront curvature is studied using a ray geometric approach. The plane wavefront beamformers under curved data can suffer large performance degradation for arrivals with low arrival angle with respect to the horizontal and curved wavefront beamforming is proposed. The distortion caused by the smoothing techniques in the context of the MV processor is addressed. Mismatch can be avoided by using curved steering vectors modified to account for the effect of spatial smoothing on  $\mathbf{R}$ .

### **2.2. The Problem of Correlated Arrivals**

#### **2.2.1. Limitations of the Adaptive Methods**

Although array processing and spectral analysis on time series are related, they are not identical. The surface and bottom boundaries produce multipath propagation [Yen; 1977], and the sound projected by a source arrives at a vertical line array through multipaths [Urick; 1983]. The severe performance limitations of the MV beamformer under correlated arrivals are well known [White; 1979, Cantoni; 1980]. The adaptive filter uses the non-look direction signals to minimize its output power and since the signals are correlated with the look direction signal, the latter is suppressed. This process is the so-called signal cancellation phenomena in adaptive antennas [Widrow; 1982].

#### **2.2.2. Structure of the Covariance Matrix Under Correlated Arrivals**

In Section 1.5, it was shown that coherence between two arrivals results in a rank deficient signal covariance matrix. This explains why, on an algorithmic level, the adaptive method fails. Since the signal model presented in Chapter 1 breaks down, the structure of the covariance matrix for inhomogeneous wavefields is now investigated.

The array covariance matrix of a homogeneous field using the plane wave array manifold is both Toeplitz and Hermitian. In a realistic environment, the field is not homogeneous i.e. not stationary in space because of multipath arrivals and the covariance matrix of an equi-spaced sensor line array is not Toeplitz [Gabriel; 1980] (it is Hermitian by construction). The model covariance matrix for two

correlated arrivals in spatially white sensor noise, given by Equation (1.30) (where the signal covariance matrix is given by Equation (1.29)) has terms along the upper diagonal given by

$$\mathbf{R}_{model}(i, i+1) = \sigma_0^2 e^{-j2\pi k_0} + \sigma_1^2 e^{-j2\pi k_1} + \sigma_0 \sigma_1 \left\{ [\rho e^{j2\pi i(k_0 - k_1)}] e^{-j2\pi k_0} + [\rho^* e^{j2\pi i(k_1 - k_0)}] e^{-j2\pi k_1} \right\} \quad (2.1)$$

for  $i = 1, M-1$ . The matrix is not Toeplitz because of the last term due to correlation ( $\rho \neq 0$ ). Correlation introduces a modulation term in the diagonals of the array covariance matrix, as can be observed on Figure 2.1 where plotted are the magnitude and phase of the upper diagonals of the array covariance matrix for a field corresponding to two uncorrelated and coherent unit-power plane wave arrivals. The order of the diagonals can be identified by their length. The line array ( $10\frac{1}{3}$  wavelength long) has 32 sensors with 25 m interelement spacing. The arrivals have  $-10^\circ$  and  $-20^\circ$  incidence angles. The operating frequency is 20 Hz and the sound speed is 1498 m/s.

Observing this non-Toeplitz character is important since it leads, in a natural way, to the processing methods designed to limit the negative effects of correlation: spatial smoothing.

### 2.2.3. Pre-Processing Methods

The methods which limit the effects of spatial correlation operate on the covariance matrix to make it "more Toeplitz" by performing an averaging operation [Linebarger; 1988]. Based on the concept of redundancy [Linebarger; 1988], the straight arithmetic and geometric averaging of the covariance matrix diagonals, have been proposed in the literature [Naidu; 1988, Hsu; 1986]. However, forcing a Toeplitz structure does not systematically result in a non-negative definite cross-spectral matrix and is considered not viable [Linebarger; 1988]. The major successful averaging techniques proposed in the literature are

- (1) Frequency averaging which is averaging covariance matrices at different frequencies [Wang; 1985, Zhu; 1988]. This method is relevant only to broadband situations and will not be discussed here.
- (2) Spatial averaging or spatial smoothing, developed for narrowband problems (and for a plane wavefront array manifold) [Gabriel; 1980, Shan; 1985, Su; 1986, Reddy; 1987, Takao; 1987, Linebarger; 1988]. This method is particularly relevant to the problems discussed here, and will be used in this work.

#### 2.2.3.1. Spatial Smoothing

The concept of spatial smoothing comes from the idea that the relative phase between two correlated arrivals changes in space [Gabriel; 1980, Widrow; 1982]. In practice, moving the array in space may not be practical. Spatial smoothing is achieved by averaging covariance matrices estimated on subarrays extracted from the full aperture and corresponding to slightly different spatial position. It induces a reduction of the terms due to correlation [Linebarger; 1988] because the phase variations are eventually averaged to zero. The technique uses the special geometry of line arrays with equi-spaced sensors [Linebarger; 1988] and computes the average of the covariance matrix estimated on subarrays, where each subarray shares all but one of its sensors with an adjacent subarray [Shan; 1985]. If the full aperture array has  $M$  sensors, and the subarrays have  $s$  sensors, this is equivalent to averaging  $M - s + 1$  blocks of  $s$  by  $s$  element extracted from the full array  $M$  by  $M$  covariance matrix along the main diagonal [Takao; 1987]. It can also be viewed as

a low-pass filtering operation [Linebarger; 1988]. Furthermore averaging decreases the variance of the estimate of the cross-spectral matrix.

Spatial smoothing is implemented as follows [Shan; 1985]. If  $\mathbf{X}$  is the full aperture  $(M, 1)$  array vector, and  $\mathbf{X}_i$  the  $i^{th}$   $(s, 1)$  subaperture signal vector

$$\mathbf{X}_i^T = [X_i(f) \ X_{i+1}(f) \ \cdots \ X_{i+s}(f)] \quad (2.2)$$

the spatially smoothed covariance matrix is

$$\mathbf{R}_{smoothed} = \frac{1}{M-s+1} \sum_{i=0}^{M-s} \mathbf{X}_i \mathbf{X}_i^H \quad (2.3)$$

To illustrate the decorrelation process achieved by spatial smoothing, the diagonals of the array covariance of a field composed of two coherent arrivals are plotted in Figure 2.2 for two smoothing scenarios. As in Figure 2.1, the two unit-power plane wave arrivals impinge on the array with incidence angles of  $-10^\circ$  and  $-20^\circ$ . The array is  $10 \frac{1}{3}$  wavelength long and has 32 sensors. Two different subarray lengths are selected, 24 and 16, so that the number of averages in the smoothing increases from 9 to 17. As the number of average increases or subarray length decreases, the covariance matrix becomes more and more Toeplitz.

It is shown in [Shan; 1985] that if  $p$  coherent signals impinge on the array, at least  $p$  averages over subarrays of  $p$  elements must be performed in order to recover the rank of the signal covariance matrix, that is to have  $\det \mathbf{S} \neq 0$  (i.e.  $\mathbf{S}$  is a  $p$  by  $p$  matrix of rank  $p$ ). This result is of great importance because it indicates the number of averages necessary to determine the direction of arrivals with high resolution methods (i.e. eigenvector methods). It leads to the rule of thumb that a  $M$  sensor array is able to detect at most  $\frac{M}{2}$  correlated arrivals with spatial smoothing [Shan; 1985].

This results is not as valuable for the MV processor since a full rank matrix does not ensure total decorrelation of the arrivals (i.e. a diagonal signal covariance matrix). Partial correlation among the arrivals leads to partial signal cancellation for the adaptive beamformer and therefore performance degradation.

The spatial smoothing decorrelation rate for two correlated arrivals is studied in [Reddy; 1987]. The model covariance matrix corresponding to the  $k^{th}$  subarray can be expressed as

$$\mathbf{R}_k = \mathbf{B} \Phi^{k-1} \mathbf{S} (\Phi^{k-1})^H \mathbf{B}^H + \sigma^2 \mathbf{I} \quad (2.4)$$

where  $\mathbf{R}_k$  is the subarray covariance matrix and corresponds to  $\mathbf{X}_k \mathbf{X}_k^H$ ,  $\mathbf{B}$  is the stacked plane wave direction matrix (a  $s$  by  $p$  matrix, where  $p$  is the number of signals),  $\mathbf{S}$  is the  $p$  by  $p$  signal covariance matrix and  $\Phi$  the diagonal matrix given by

$$\Phi = \begin{bmatrix} e^{-j\omega\tau_1} & 0 & 0 & \cdots & 0 \\ 0 & e^{-j\omega\tau_2} & 0 & \cdots & 0 \\ 0 & 0 & e^{-j\omega\tau_3} & \cdots & 0 \\ \cdot & \cdot & \cdot & \cdots & \cdot \\ \cdot & \cdot & \cdot & \cdots & \cdot \\ \cdot & \cdot & \cdot & \cdots & \cdot \\ 0 & 0 & 0 & \cdots & e^{-j\omega\tau_p} \end{bmatrix} \quad (2.5)$$



where  $\tau_i$  represents the elementary time delay between two consecutive sensors for the  $i^{th}$  arrival.

This formulation allows the effects of spatial smoothing to be interpreted in a useful way in terms of the smoothed signal covariance matrix:

$$\bar{\mathbf{S}} = \frac{1}{K} \sum_{k=1}^K \Phi^{k-1} \mathbf{S} (\Phi^{k-1})^H \quad (2.6)$$

where  $K$  is the number of averages, also called the smoothing index. Restricting the discussion to two correlated arrivals, [Reddy; 1987] indicates that perfect decorrelation is achieved when the (1,2) term of  $\bar{\mathbf{S}}$  is equal to zero. This term is given by

$$\bar{\mathbf{S}}(1, 2) = \frac{\sigma_0 \sigma_1 \rho}{K} \sum_{k=1}^K \exp \left[ -j(k-1) 2\pi \frac{d}{\lambda} (\sin \theta_0 - \sin \theta_1) \right] \quad (2.7)$$

$$\bar{\mathbf{S}}(1, 2) = \frac{\sigma_0 \sigma_1 \rho}{K} \frac{\sin \frac{\pi d K}{\lambda} (\sin \theta_0 - \sin \theta_1)}{\sin \frac{\pi d}{\lambda} (\sin \theta_0 - \sin \theta_1)} \quad (2.8)$$

where  $\rho$  is complex correlation between the two arrivals of power  $\sigma_0^2, \sigma_1^2$  and physical arrival angles  $\theta_0$  and  $\theta_1$ ,  $d$  is the array interelement spacing, and  $\lambda$  the acoustic wavelength. Perfect decorrelation is achieved when

$$K = \frac{\lambda}{d |\sin \theta_0 - \sin \theta_1|} \quad (2.9)$$

These values of the smoothing index  $K$  can be tabulated for a particular array geometry and depends on the arrival pair angular separation and position with respect to broadside. For instance, 12 averages are required to fully decorrelate a 5° separated pair impinging on an array with half wavelength interelement spacing at 10°. Equation (2.9) shows that the number of averages necessary to decorrelate two arrivals depends on their angular spacing. Two closely spaced arrivals are very difficult to decorrelate [Reddy; 1987] and require a large number of averages which in practice may not be possible, the array having a limited number of sensors. Furthermore, the effective aperture is reduced from  $M$  to  $s$  sensor which results in lower resolution. Decorrelation is achieved at the cost of resolution and computational burden.

Simulations can be used to quantify the signal cancellation loss at the output of the MV processor. As before, a  $10\frac{1}{3}$  wavelength array with 32 sensors receives a pair of coherent unit-power plane wave arrivals in the set of incidence angles  $\{0^\circ, 5^\circ, 10^\circ, 15^\circ, 20^\circ, 25^\circ, 30^\circ, 35^\circ, 40^\circ\}$ . A background sensor noise is also included with a power of -20 dB. The possible angular spacings are multiples of 5° which is close to the Rayleigh resolution of the array. For each pair of arrival combinations, spatial smoothing followed by MV beamforming is performed. The difference in dB between the true power (in this case 0 dB) and the power of the arrivals at the output of the beamformer is measured and plotted in Figure 2.3 as a function of the number of spatial smoothing averages (which varies from 3 to 19). Each panel corresponds to an angular separation which includes a number of arrival combinations, e.g. the 10° separation corresponds to the following pairs: (0°, 10°), (5°, 15°), (10°, 20°), (15°, 25°), (20°, 30°), (25°, 35°), (30°, 40°). The impact of the number of averages on the final angular spectrum can be observed in Figure 2.3 and a best subarray length can be selected for each case. Considerable smoothing must be performed when the two arrivals are close together: a 5° separation requires at

least 16 averages for the MV processor to yield cancellation loss on the order of a few dB. On the other hand, a subsegment length of 24 does a good job at decorrelating arrivals separated by at least  $10^\circ$ .

### 2.2.3.2. Modified Spatial Smoothing

A second version of spatial smoothing has been proposed [Williams; 1988] and uses an estimate of the covariance matrix which is the modified covariance matrix of the combined forward/backward linear prediction algorithm for auto-regressive spectral estimation [Burg; 1967]. The modified covariance method is known to perform better in time series auto-regressive spectral estimation in producing less spurious peaks [Marple; 1987]. The modified covariance matrix also is used in the maximum entropy wavenumber processing for line arrays [Barnard; 1982] and in the Kumaresan-Tufts high resolution method of direction of arrival estimation [Kumaresan; 1983].

In modified spatial smoothing, the covariance matrices of the array data and of the reversed data are estimated and averaged to produce the array covariance matrix. This is made possible by the special geometry of equi-spaced line arrays and the planar array manifold. The modified spatial smoothing does the average of the spatially smoothed covariance matrices estimated on the 99 % overlapped subarrays and their corresponding reversed matrix. Modified spatial smoothing can be expressed as [Williams; 1988]

$$\mathbf{R}_{smoothed} = \frac{1}{M-s+1} \sum_{i=0}^{M-s} \frac{1}{2} (\mathbf{x}_i \mathbf{x}_i^H + \mathbf{J} (\mathbf{x}_i \mathbf{x}_i^H)^* \mathbf{J}) \quad (2.10)$$

where  $*$  is the complex conjugate operation and  $\mathbf{J}$  is the reflection matrix or reverse matrix given by

$$\mathbf{J} = \begin{bmatrix} 0 & 0 & 0 & \dots & 1 \\ 0 & 0 & 0 & \dots & 0 \\ \vdots & \vdots & \vdots & \ddots & \vdots \\ \vdots & \vdots & \vdots & \ddots & \vdots \\ \vdots & \vdots & 1 & \dots & \vdots \\ 0 & 1 & 0 & \dots & 0 \\ 1 & 0 & 0 & \dots & 0 \end{bmatrix} \quad (2.11)$$

It is shown in [Pillai; 1989] that if  $p$  correlated arrivals impinge on the array, it is sufficient to average  $\frac{p}{2}$  subarrays of  $p$  sensors to recover the rank of the signal covariance matrix (i.e. to have  $\det \mathbf{S} \neq 0$ ), this result was first stated and proved (under some specific constraints) in [Williams; 1988]. With modified spatial smoothing, a  $M$  sensor array is able to detect at most  $\frac{2M}{3}$  correlated arrivals [Williams; 1988]. This result is of great interest because it indicates that the number of averages, necessary to determine the direction of arrivals with principal component methods, is half of what the original spatial smoothing requires. It allows the so-called increase in efficient array aperture, thus better resolution.

The issue with the MV processor is the decorrelation rate that modified spatial smoothing can achieve, compared to original spatial smoothing. The study outlined in the previous section is repeated here for the modified spatial smoothing. One considers two correlated arrivals impinging on a  $M$  sensor array referenced to its center as in [Takao; 1987]. Then, the full aperture plane wave steering vectors are given by

$$\mathbf{d}_i^T = \left[ \exp(j \frac{2\pi d}{\lambda} (m - \frac{M+1}{2}) \sin \theta_i) \right]_{m=1, M} \quad (2.12)$$

The array and signal covariance matrices can be separated into a part that corresponds to original spatial smoothing  $\bar{\mathbf{R}}_1$ ,  $\bar{\mathbf{S}}_1$  and a part that corresponds to modified spatial smoothing  $\bar{\mathbf{R}}_2$ ,  $\bar{\mathbf{S}}_2$ . The (1,2) term of the spatially smoothed signal covariance matrix is given by Equation (2.8). The modified part of the array covariance matrix is given by

$$\bar{\mathbf{R}}_2 = \mathbf{J} \bar{\mathbf{R}}_1^* \mathbf{J} \quad (2.13)$$

where  $\mathbf{R}_1$  the spatially smoothed covariance matrix. Using the factorization of  $\mathbf{R}_1$  in terms of the signal covariance matrix  $\bar{\mathbf{S}}_1$

$$\bar{\mathbf{R}}_1 = \mathbf{B} \bar{\mathbf{S}}_1 \mathbf{B}^H \quad (2.14)$$

where  $\mathbf{B}$  is the stacked direction matrix over the subarrays, the modified covariance matrix  $\bar{\mathbf{R}}_2$  is

$$\bar{\mathbf{R}}_2 = \mathbf{J} \mathbf{B}^* \bar{\mathbf{S}}_1^* \mathbf{B}^T \mathbf{J} \quad (2.15)$$

Using the fact that  $\mathbf{J} \mathbf{B}^* = \mathbf{B}$  [Williams; 1988],  $\bar{\mathbf{R}}_2 = \mathbf{B} \bar{\mathbf{S}}_1^* \mathbf{B}^H$  and since  $\bar{\mathbf{R}}_2 = \mathbf{B} \bar{\mathbf{S}}_2 \mathbf{B}^H$ , the modified part of the signal covariance matrix is  $\bar{\mathbf{S}}_2 = \bar{\mathbf{S}}_1^*$ . Therefore, the (1,2) term of  $\bar{\mathbf{S}}$  is

$$\bar{\mathbf{S}}(1, 2) = \frac{\sigma_0 \sigma_1 |\rho|}{M-s+1} \frac{\sin \pi \frac{d}{\lambda} K(\sin \theta_0 - \sin \theta_1)}{\sin \pi \frac{d}{\lambda} (\sin \theta_0 - \sin \theta_1)} \cos \phi \quad (2.16)$$

where  $\phi$  and  $|\rho|$  are given by the complex correlation between the two arrivals  $\rho = |\rho| e^{j\phi}$ .

This result shows a peculiarity of modified spatial smoothing: when the electrical phase  $\phi$  between the two arrivals referenced at the center of the array is  $\frac{\pi}{2}$ , perfect decorrelation is achieved, whatever spatial smoothing length is used. The array covariance matrix is Toeplitz and there is no loss due to correlation at the output of the MV beamformer, even if  $s = M$ . When the electrical phase is zero, the decorrelation rate is identical to that of spatial smoothing. These results, that strongly depend on the electrical phase  $\phi$ , are similar to what was observed in [Gabriel; 1986] for adaptive antennas and in [White; 1979] for the minimum entropy method operating on fully correlated arrivals in quadrature. The chances of having two signals in quadrature at the center of the array are slim. Thus, all one can state is that the modified spatial smoothing works as well or better than the original spatial smoothing in decorrelating a pair of correlated arrivals. If the reference is taken at another spatial position along the array, the dependence of the modified spatial smoothing performance on the electrical phase  $\phi$  still exists. The precise phase relationship between the two signals for which decorrelation is achieved is not  $\frac{\pi}{2}$  and depends on the reference point, the interelement spacing, the wavelength, and the arrival angles.

These theoretical results showing the importance of the relative phase between two arrivals are simulated with the same 32 sensor array receiving two unit-power plane wave arrivals at  $-5^\circ$  and  $0^\circ$  incidence angle. The subarray length is 32 so that only two averages using modified spatial smoothing are performed. The maximum loss of the two arrivals due to correlation at the output of the MV beamformer is plotted on Figure 2.4. When the two signals are in quadrature, there

is no loss since the modified covariance matrix is Toeplitz. The loss due to correlation increases as the electrical phase decreases, and reduces to what is produced by original spatial smoothing.

#### **2.2.4. Conclusions**

The effect of correlated arrivals on the adaptive MV beamformer has been highlighted and spatial smoothing has been described and interpreted. The smoothing techniques attempt to reduce the modulation of the diagonals of the covariance matrix which should be Toeplitz according to the homogeneous signal and planar wavefront model. Signal cancellation occurs as soon as correlation among arrivals exists. The difficulty of decorrelating two closely spaced arrivals clearly appears in the simulations. In practice, substantial loss due to correlation may still occur even after heavy spatial smoothing. Modified spatial smoothing generally produces a larger decorrelation than the original spatial smoothing but depends on the relative phase of the arrivals. Although spatial smoothing techniques reduce the effective aperture of the array (thus reducing the resolution and increasing the computational burden), they are a necessary pre-processing step before using the adaptive MV processor.

### **2.3. Wavefront Curvature**

#### **2.3.1. Introduction**

Besides the surface and bottom boundaries, another important aspect of the underwater medium is its highly refractive character, which is variable in the vertical as well as the horizontal. Propagation over long range is controlled by the sound speed profile depth and range dependence [Murphy; 1987]. The wavefront curvature due to refraction is investigated in the following.

In ray theory, the variation of sound speed with depth causes ray bending and can be summarized by Snell's law [Brekhovskikh; 1982] :

$$\frac{c}{\cos\theta} = \text{constant} \quad (2.17)$$

where  $c$  is the local sound speed and  $\theta$  the ray angle with respect to the horizontal. Ray bending can be large, for instance, a  $10^\circ$  angle ray at great depth with speed of 1500 m/s has a  $13.8^\circ$  angle with respect to the horizontal shallower in the water column where the sound speed equals 1480 m/s. Since ray bending can be large over large depth, wavefront curvature could have an important impact on the angular spectra produced by the beamformers processing the data from large vertical line arrays. Processing a field with varying arrival angle across the array aperture is similar to the case of processing nonstationary random processes in time series analysis. The selection of the plane wave array manifold that corresponds to a medium of a constant sound speed, may not be appropriate, especially for a very long vertical line array.

First, attention is directed toward generating a curved wavefront array manifold based on the sound speed profile across the array. This manifold will then allow the simulation of a more realistic pressure field and the evaluation of the plane wavefront beamformers under curved arrivals.

#### **2.3.2. Generating Curved Wavefronts**

### 2.3.2.1. Derivation of the Phase Relationships in the Vertical

Wavefront curvature is modelled with the simple geometric approach of ray theory. Since the sound speed continuously varies with depth, the phase variations from a point  $M_0$  in space to a point  $M_1$  can be expressed by the integral relationship

$$\phi = \int_{M_0}^{M_1} \vec{K} d\vec{r} \quad (2.18)$$

where  $\phi$  is the phase of the propagating wavefront,  $\vec{K}$  the wavenumber vector which is a function of position in the two dimensional space sampled by the vertical array defined by the  $(r, z)$  coordinate system, with  $\vec{r} = r \vec{e}_r + z \vec{e}_z$ .  $(\vec{e}_r, \vec{e}_z)$  spans the space as defined by Figure 2.5.  $\vec{K}$  can be expressed as

$$\vec{K}(r, z) = \frac{2\pi f}{c(r, z)} \left( \cos\theta(r, z) \vec{e}_r + \sin\theta(r, z) \vec{e}_z \right) \quad (2.19)$$

where  $f$  is the acoustic frequency,  $c(r, z)$  the sound speed,  $\theta(r, z)$  the ray angle with respect to the horizontal at a point in space of coordinates  $(r, z)$ . If the receiving array has its sensors numbered from top to bottom, negative angles of arrival corresponds to downgoing sound or uplooking beams. Since the array is deployed in the vertical, only phase variations in the vertical are of interest so that  $d\vec{r} = dz \vec{e}_z$  and, assuming a horizontally stratified ocean (i.e. range independent), Equation (2.18) becomes

$$\phi = 2\pi f \int_{z_0}^{z_1} \frac{\sin\theta(z)}{c(z)} dz \quad (2.20)$$

Using Snell's law, one gets

$$\phi = 2\pi f \int_{z_0}^{z_1} \frac{\text{Sgn}(\theta(z))}{c(z)} \left( 1 - \cos^2\theta(z_0) \left[ \frac{c(z)}{c(z_0)} \right]^2 \right)^{1/2} dz \quad (2.21)$$

where  $\text{Sgn}$  is the signum function, and  $\cos^2\theta(z_0) \left[ \frac{c(z)}{c(z_0)} \right]^2 < 1$  is implicitly assumed for all  $z$ . If the medium is isovelocity (for all  $z$ ,  $c(z) = c(z_0)$ ), Equation (2.21) reduces to the plane wavefront result :

$$\phi = \frac{2\pi f \sin\theta(z_0)}{c(z_0)} (z_1 - z_0) \quad (2.22)$$

Equation (2.21) provides the variation of phase in the vertical and is identical to a ray representation of the field, as shown in [Tran; 1989a].

### 2.3.2.2. Partial Insonification

The phase relationships, thus the arrival angles, depend on the selected reference depth and corresponding sound speed. Several reference points can be used, for instance the center of the array aperture, or the point of minimum sound speed across the array. Using a particular reference point, the results of the previous Section can be used to compute the phase entering into the steering vectors. The replica vectors then can be stacked in the array manifold matrix which has complex columns that correspond to physical angles and rows that correspond to the different sensors of the array. The sensors are assumed numbered from top to bottom. The  $i^{\text{th}}$  sensor or the  $i^{\text{th}}$  row in the matrix is associated with a sound speed  $c_i$ . If  $c_i > c_0$ , where  $c_0$  is the reference sound velocity (sound velocity at the center of the array), a ray with angle  $\theta_0$  with respect to the horizontal at the center

may not propagate to the sensor depending on  $\theta_0$ . The condition for physical existence of a ray at the  $i^{th}$  sensor is

$$\theta_0 \geq \cos^{-1} \frac{c_0}{c_i} \quad (2.25)$$

If Equation (2.25) does not hold, the ray has turned over, and the steering vector complex exponential is replaced by zero. Beyond the turning point, there is a shadow zone where the solution of the wave equation, under the WKB approximation, is exponentially decaying [Boyles; 1984, p. 210]. Here, the ray model assumes that there is no insonification past the turning point. Figure 2.6 shows a generic array manifold matrix for a particular sound velocity profile with respect to a receiving line array. The shaded area corresponds to zero-filled entries (i.e. no sound).

### 2.3.2.3. How Curved Are Curved Wavefronts ?

The relative importance of wavefront curvature with respect to plane wavefronts is now assessed. This is performed by simply comparing the phase of a curved wavefront to that of a corresponding plane wavefront (i.e. with same angle at the reference point), with the reference taken at the center of the array. A simulation is performed on a 64 element array with 25 m spacing in the water column with a sound speed linearly increasing from 1481 m/s at the top of the array to 1515 m/s at the bottom of the array. The reference sound speed at the center of the array is 1498 m/s and the frequency is 20 Hz. The phase differences for each sensor position and all arrivals with angles between  $-90^\circ$  and  $90^\circ$  are plotted on Figure 2.7. The relative phase change between curved and plane wavefront arrivals is up to 10 % of the maximum total phase phase variation. Figure 2.7 shows that only a few steering vectors yield a large phase difference between the curved and plane cases. The arrivals which are subject to these large deviations have low angles with respect to the horizontal. Even short apertures experience some important relative phase variations at low angles.

### 2.3.3. Plane Wave Beamformers in a Curved Wavefront Environment

The response of the plane wave beamformers to a curved wavefront field is of interest in order to assess the importance of wavefront curvature. The 64 element array of the previous Section is used in the same environment. The data at the input of the plane wave beamformer are unit-power curved wavefront arrivals. Curved and plane wavefront phase relationships are generated as discussed in the previous sections. No noise is included here. A Kaiser-Bessel window with an  $\alpha$  parameter of 1.5 weights the data across the array in order to yield a 38 dB side lobe rejection. Bearing responses for arrivals at  $-40^\circ, -30^\circ, -20^\circ, -10^\circ, -5^\circ, -0.2^\circ, 0.2^\circ, 7^\circ, 10^\circ, 20^\circ, 30^\circ, 40^\circ$  are plotted in Figure 2.8. The bearing responses of the conventional beamformer for curved data are similar to the one for plane wave data in the case of high angles of arrival. Differences appear for low angles of arrival, where the main peaks appear smeared and biased. The conventional beamformer yields a peak at  $5^\circ$  with a 3 dB loss under the  $0.2^\circ$  arrival. Furthermore, the side lobe level for low arrival angles is raised by at least 20 dB.

Since there is no noise in the simulations, the MV processor is extremely sensitive to mismatch compared to the conventional processor [Seglison; 1970, McDonough; 1971], as illustrated in Figure 2.9. The plane wave MV bearing responses show large mismatch loss for all directions especially for near horizontal arrivals where curvature is largest. The loss due to mismatch at the output of the MV processor is plotted in Figure 2.10 for different array lengths in the same environment. The loss increases with the number of sensors. It also increases as the

arrivals becomes closer to the horizontal. These results suggest that wavefront curvature should be included in the processing.

#### 2.3.4. Curved Wavefront Beamforming

The results of the previous Section indicate that using the plane array manifold for a vertical array in a curved wavefront environment may not be appropriate, especially for low angle of arrivals. Curved wavefront steering vectors should be used as replica vectors [Murphy87].

##### 2.3.4.1. Conventional Curved Wavefront Beamforming

Generally, the Bartlett beamformer is used with a tapering window in order to provide good sidelobe rejection. Windowing is necessary to avoid unacceptably high sidelobe levels, but is not as straightforward as in the plane wave case, because of the partial insonification of the array aperture. The window length has to be adjusted and applied to the insonified part only of the array manifold matrix. Curved wavefront processing using an adjusted Kaiser-Bessel window with an  $\alpha$  parameter of 1.5 avoids the smearing and bias for low angle of arrival but not the high sidelobe level on the order of -20 dB which is due to the reduction of the aperture length corresponding to partial insonification [Tran; 1989a].

##### 2.3.4.2. MV Curved Wavefront Beamforming

###### Array Covariance Matrix of a Curved Wavefield

To understand why the plane wave MV processor performs so poorly under curved wavefront data, the effects of curvature on the array covariance matrix are now investigated. Uncorrelated plane wavefront arrivals impinging on a line array with equispaced sensors lead to a Toeplitz Hermitian covariance matrix. When the arrivals have curved wavefronts, the corresponding phase variations from sensor to sensor are not constant and the covariance matrix is not Toeplitz. The contribution to the covariance matrix of an arrival with a signal direction  $\mathbf{E}$

$$\mathbf{E}^T = [e^{j\phi_1} \ e^{j\phi_2} \ \dots \ e^{j\phi_M}] \quad (2.26)$$

is  $\mathbf{E} \mathbf{E}^H$  which has a first upper diagonal given by

$$[e^{j(\phi_1 - \phi_2)} \ e^{j(\phi_2 - \phi_3)} \ \dots \ e^{j(\phi_{M-1} - \phi_M)}] \quad (2.27)$$

Because of curvature, one has for  $i \neq j$ ,  $\phi_i - \phi_{i+1} \neq \phi_j - \phi_{j+1}$ , and  $\mathbf{E} \mathbf{E}^H$  is not Toeplitz.

###### Spatial Smoothing in a Curved Wavefield

Since correlated arrivals with curved wavefront actually impinge on the array, spatial smoothing techniques must be used. The direct application of the spatial averaging schemes introduces some distortion since the underlying structure of the covariance matrix is not Toeplitz and depends on the arrivals which are unknown a priori. Simulations in a noise free environment indicate that using curved wavefront replica vectors after spatial smoothing still results in some loss, although it produces an improvement compared to using planar wavefronts, as shown in Figure 2.11 for a 32 sensor array extracted from the 64 sensor array of the previous section. This loss is due to the mismatch between the curved wavefront replica

vectors and the equivalent signal direction vectors after spatial smoothing. For each bearing characterized by a signal direction vector  $\mathbf{E}$  (which has a curved wavefront), the mismatch can be minimized by choosing the replica vector  $\tilde{\mathbf{E}}$  that maximizes the power at the output of the conventional processor

$$\tilde{\mathbf{E}}^H \left\{ T(\mathbf{E} \mathbf{E}^H) \right\} \tilde{\mathbf{E}} \quad (2.28)$$

where  $T$  denotes the smoothing transformation. The "best" replica vector is given by the eigenvector of  $T(\mathbf{E} \mathbf{E}^H)$  that has the largest eigenvalue. This replica vector will be referred to as the eigensteering vector. Because the distortion effects associated with the smoothing transformation are relatively small, the smoothed matrix is of rank 1 for all practical purposes.

Figure 2.12 gives the bearing responses for the MV beamformer processing the same 32 sensor array as in Figure 2.11, after spatial smoothing with subsegment length of 24. Eigensteering vectors are used and there is no loss due to mismatch.

### Performance of the MV Beamformer after Smoothing

The issue finally addressed here is to determine how the MV processor performs under correlated curved wavefront arrivals after pre-processing with the spatial smoothing techniques. A simulation (similar to the plane wave case of Section 2.2.3.1) with a pair of coherent arrivals [Tran; 1989a] showed that the MV processor after spatial smoothing performs like the plane wave case except for low angle arrivals near horizontal which suffer more loss. In some cases, the low angle arrivals are not even resolved as a result of the partial insonification and the reduction of the efficient aperture because of spatial smoothing [Tran; 1989a].

### 2.3.5. Conclusions

Based on the sound speed profile, curved wavefront steering vectors can be derived conveniently using the simple geometric approach of ray theory. Wavefront curvature is large for near horizontal arrivals, even for a relatively short array aperture. Arrivals with steep angles with respect to the horizontal are quite similar to plane wave arrivals. These same results are observed on the bearing responses of the plane wave conventional and MV beamformers which perform reasonably well for steep arrivals with respect to the horizontal but poorly for near horizontal arrivals. The great sensitivity to mismatch of the MV processor is observed in the noise-free simulations. The direct application of spatial smoothing to decorrelate correlated curved wavefront arrivals causes some slight distortion and using the curved wavefront array manifold still yields some loss due to mismatch. This loss due to mismatch can be avoided by using the eigensteering vectors. The performance of the curved wavefront MV beamformer under correlated curved wavefront arrivals is similar to the plane wave case (i.e. plane wave data and plane wave replica vectors), except for near horizontal arrivals where performance degradation occurs.



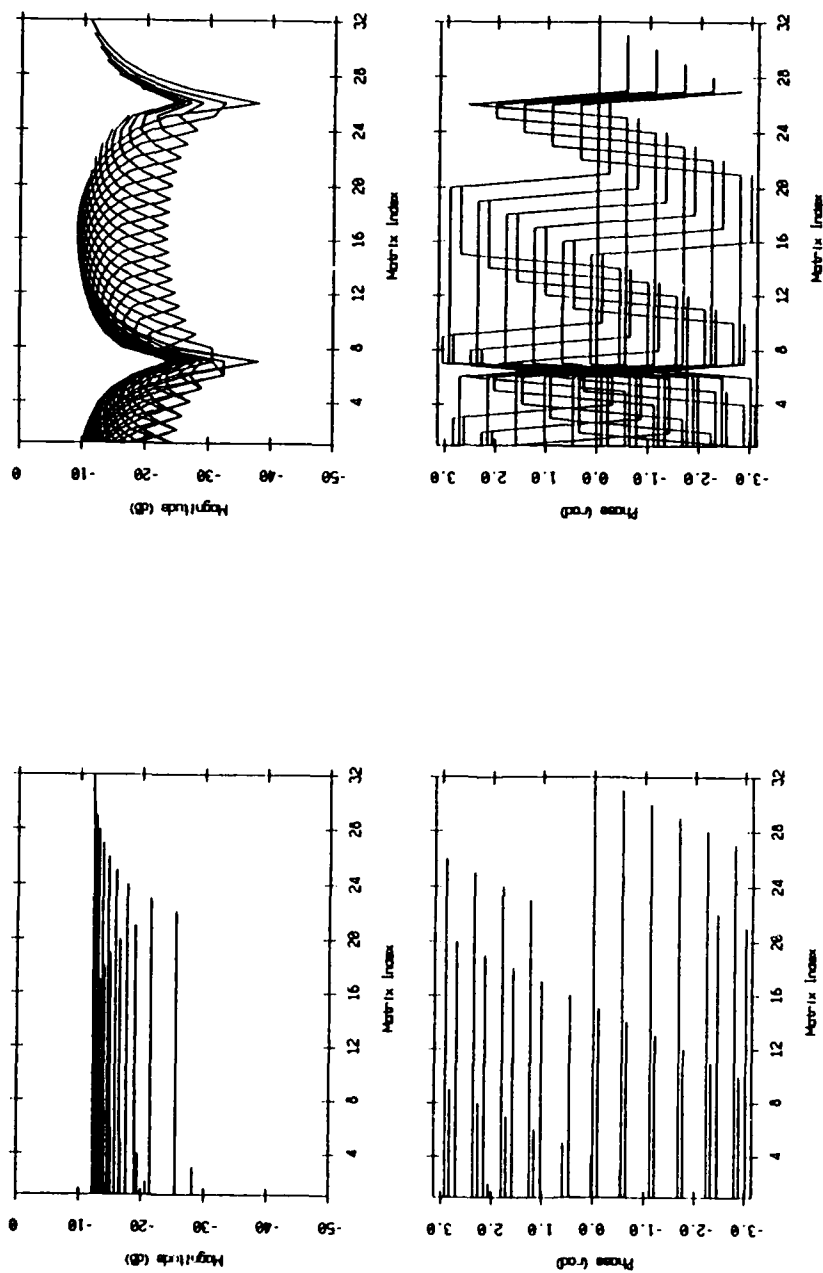


**Figure 2.1:** Upper diagonals of the covariance matrix. Two uncorrelated (left) or coherent (right) arrivals at  $-10^\circ$  and  $-20^\circ$  impinge on the 32 sensor array.

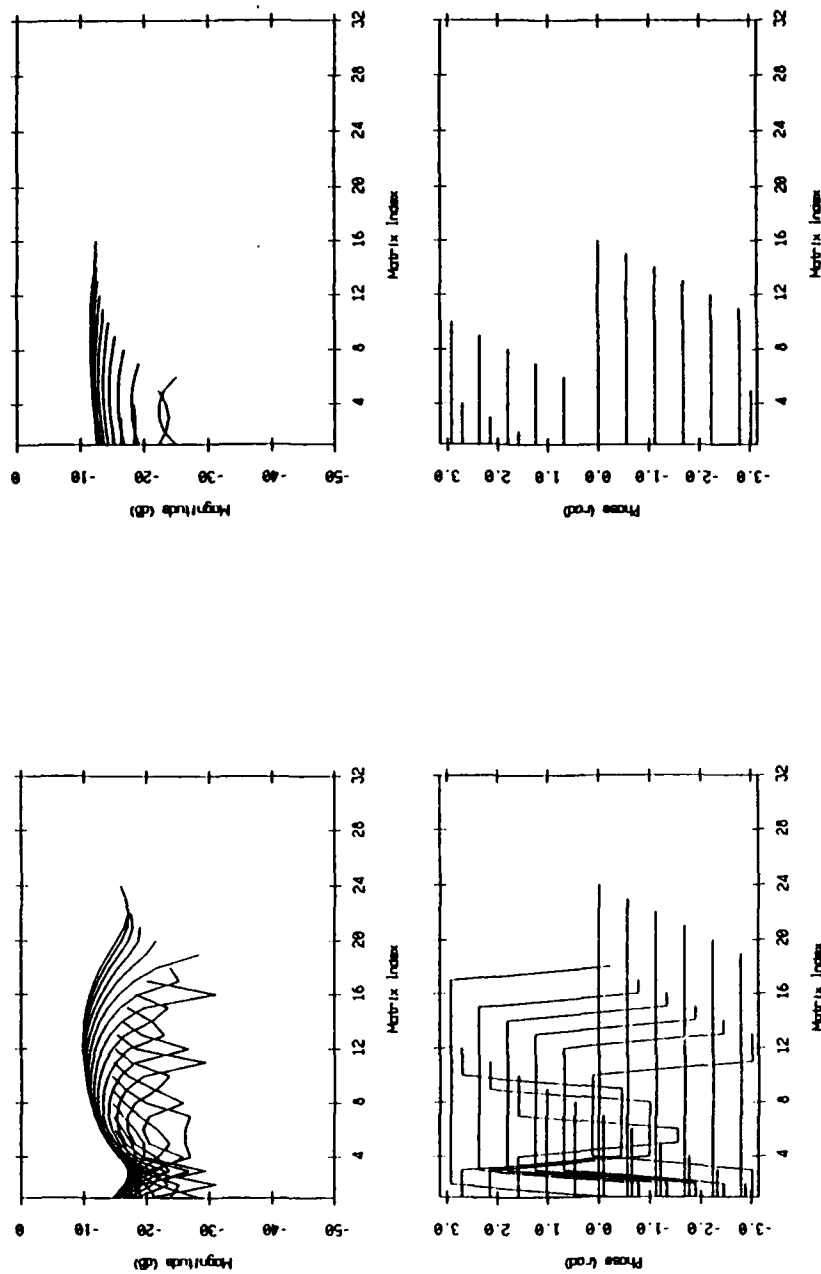


**Figure 2.2:** Upper diagonals of the covariance matrix after spatial smoothing. Smoothing is performed on 24 (left) or 16 (right) sensors. The 32 sensor array receives two coherent arrivals at  $-10^\circ$  and  $-20^\circ$ .

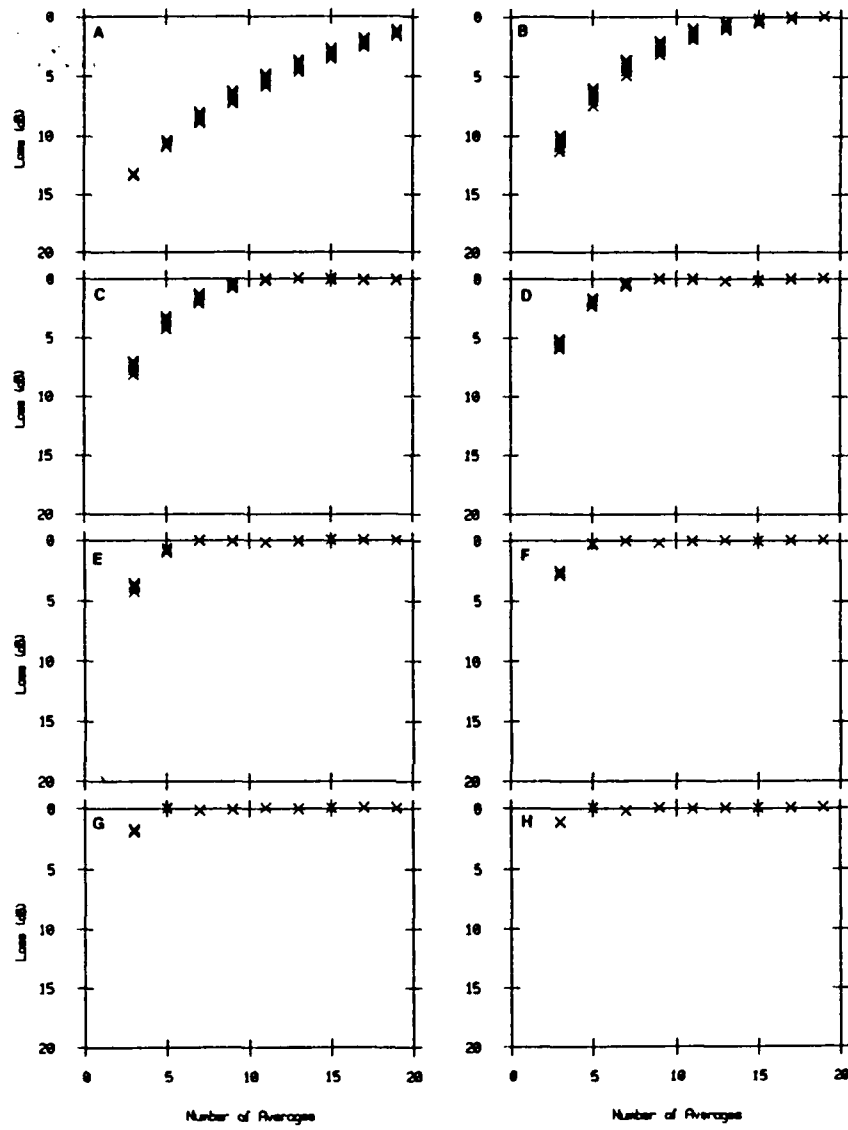
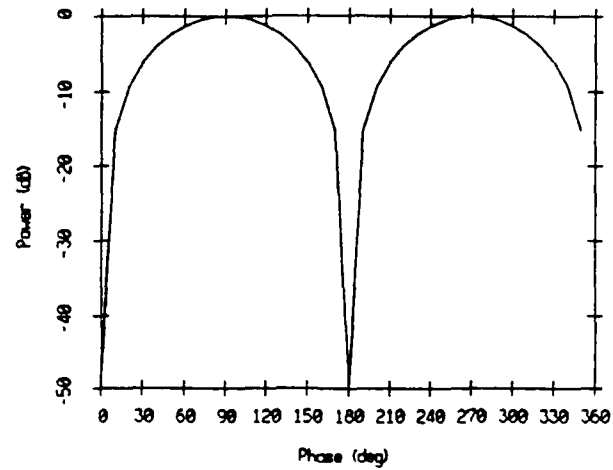
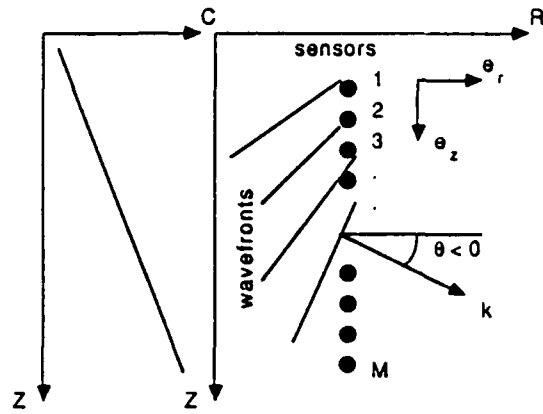


Figure 2.3: Signal cancellation loss of the MV processor after spatial smoothing. Panels A to H correspond to a coherent arrival pair with angular separations equal to  $5^\circ$  up to  $40^\circ$  with a  $5^\circ$  increment.



**Figure 2.4:** Signal cancellation loss of the MV processor after modified spatial smoothing. The loss varies as a function of the electrical phase between the two coherent arrivals that impinge on the array at  $-5^\circ$  and  $0^\circ$ .



**Figure 2.5:** Problem Geometry.

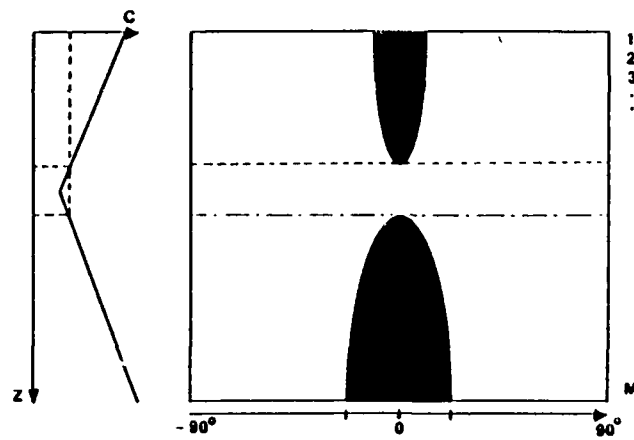


**Figure 2.6:** Typical curved wavefront array manifold.

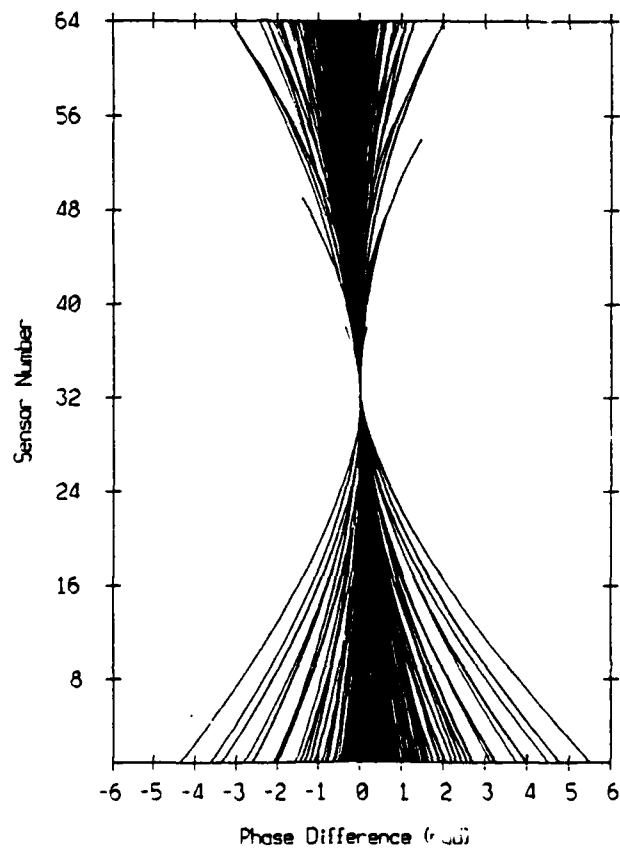


**Figure 2.7:** Phase difference between curved and plane wavefronts. The arrivals between  $-90^\circ$  and  $90^\circ$  impinge on a 64 sensor vertical array in a constant gradient sound speed.

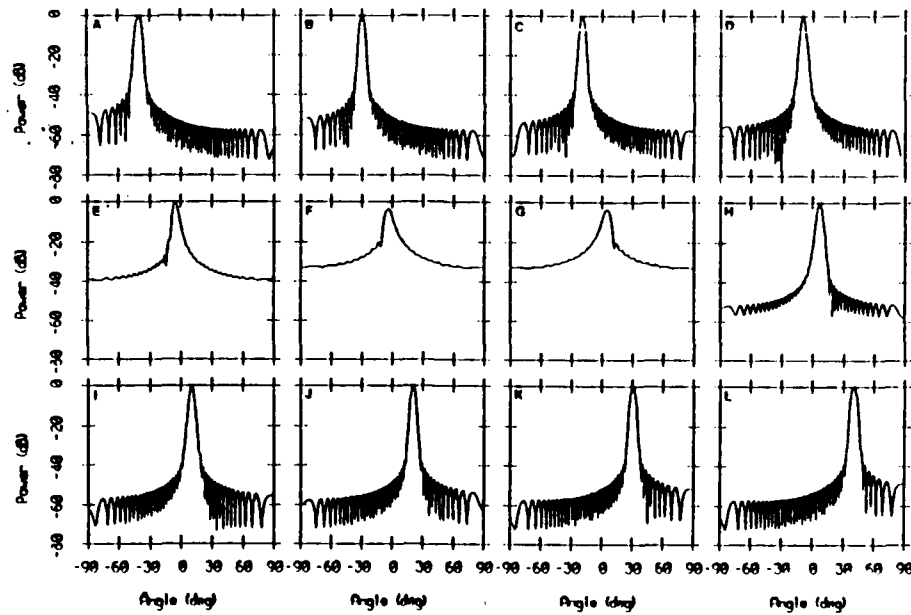


**Figure 2.8:** Bearing responses of the Conventional FFT beamformer to curved wavefronts. A Kaiser-Bessel window  $\alpha=1.5$  weights the data. Panels A to L correspond to arrivals at  $-40^\circ$ ,  $-30^\circ$ ,  $-20^\circ$ ,  $-10^\circ$ ,  $-5^\circ$ ,  $-0.2^\circ$ ,  $0.2^\circ$ ,  $7^\circ$ ,  $10^\circ$ ,  $20^\circ$ ,  $30^\circ$  and  $40^\circ$ .

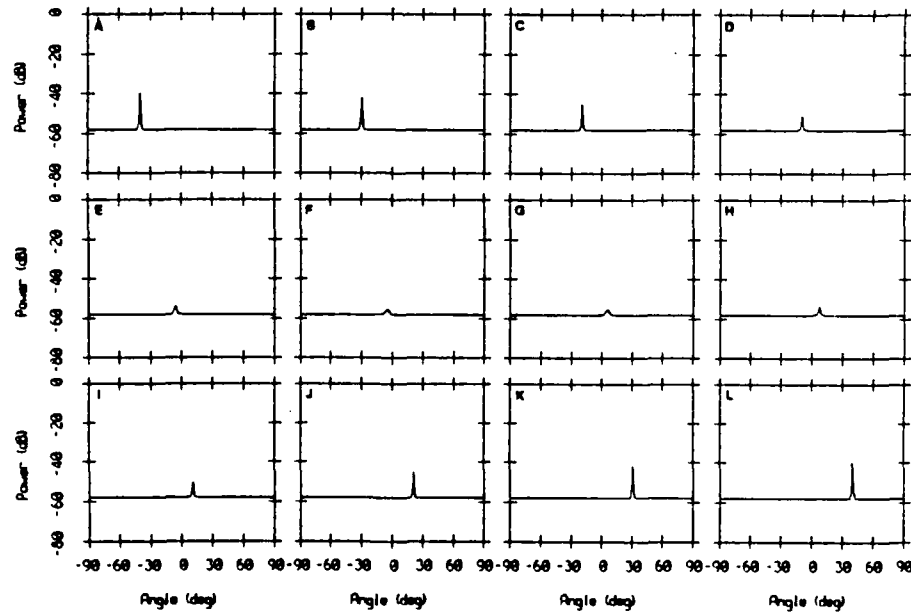


**Figure 2.9:** Bearing responses of the plane wave MV processor to curved wavefronts. Panels A to L correspond to arrivals at  $-40^\circ$ ,  $-30^\circ$ ,  $-20^\circ$ ,  $-10^\circ$ ,  $-5^\circ$ ,  $-0.2^\circ$ ,  $0.2^\circ$ ,  $7^\circ$ ,  $10^\circ$ ,  $20^\circ$ ,  $30^\circ$  and  $40^\circ$ .

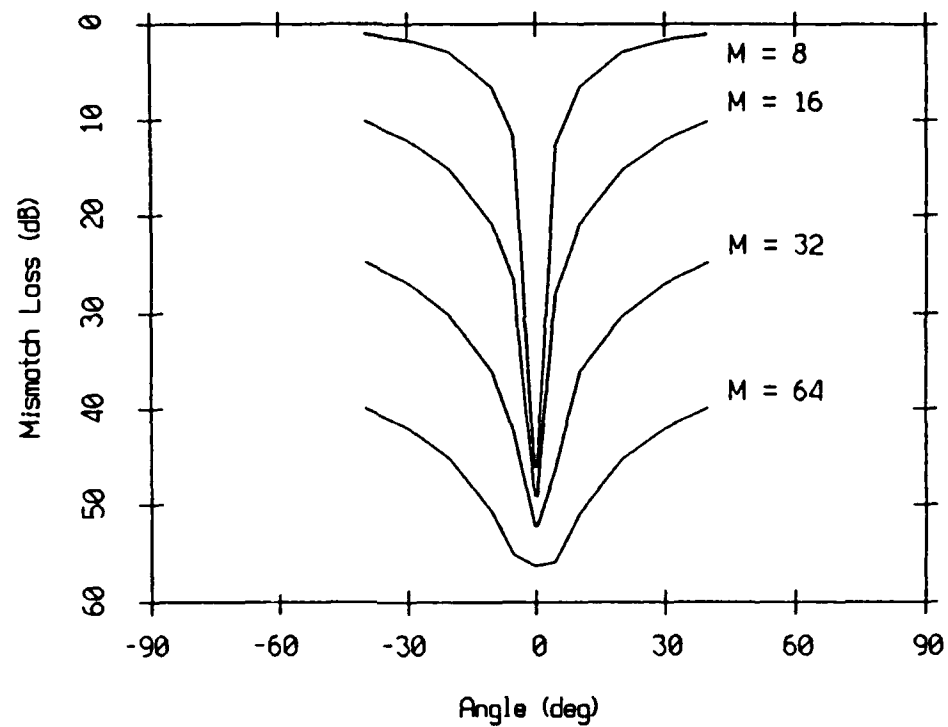


**Figure 2.10:** Loss due to mismatch of the plane wave MV processor under curved wave-front data.  $M$  is the number of array sensors.



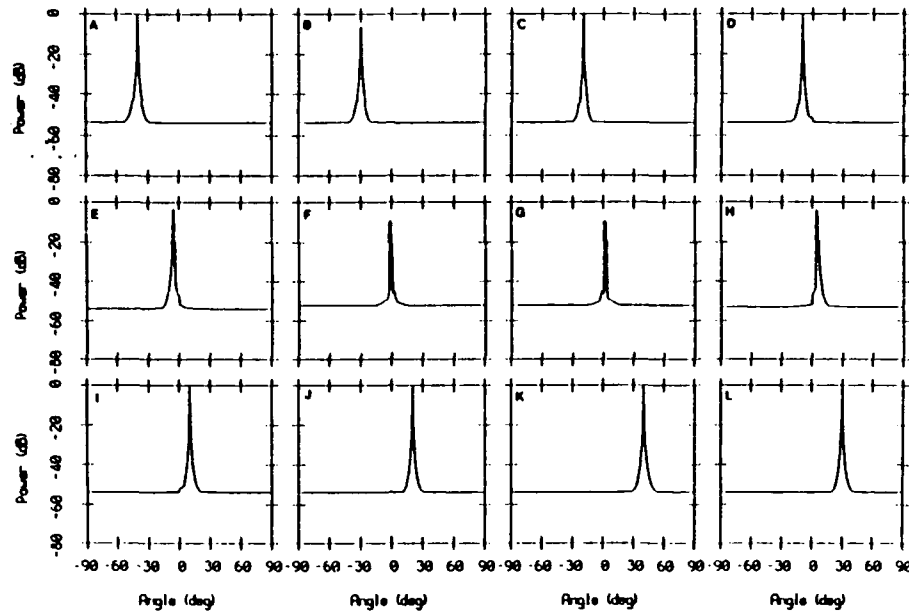


**Figure 2.11:** Bearing responses of the curved wavefront MV processor to curved wavefronts. Panels A to L correspond to arrivals at  $-40^\circ$ ,  $-30^\circ$ ,  $-20^\circ$ ,  $-10^\circ$ ,  $-5^\circ$ ,  $-0.2^\circ$ ,  $0.2^\circ$ ,  $7^\circ$ ,  $10^\circ$ ,  $20^\circ$ ,  $30^\circ$  and  $40^\circ$ .

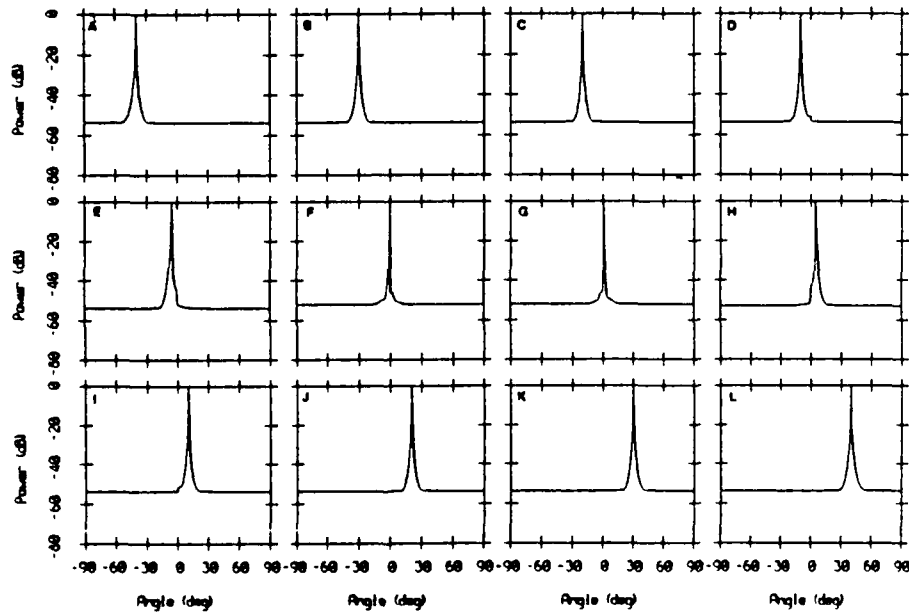


**Figure 2.12:** Bearing responses of the MV processor to curved wavefronts using the eigensteering vectors for spatial smoothing on 24 sensors. Panels A to L correspond to arrivals at  $-40^\circ$ ,  $-30^\circ$ ,  $-20^\circ$ ,  $-10^\circ$ ,  $-5^\circ$ ,  $-0.2^\circ$ ,  $0.2^\circ$ ,  $7^\circ$ ,  $10^\circ$ ,  $20^\circ$ ,  $30^\circ$  and  $40^\circ$ .

### **3. Processing Synthetic Data**

#### **3.1. Overview**

Full and subaperture beamforming approaches are proposed to process the data from large vertical line arrays and for the purpose of estimating signal arrival structure. Simulations on synthetic data produced by a normal mode model are used to determine if wavefront curvature must be considered and if the processing approaches appear qualitatively and quantitatively viable. Simulations involving a 3000 m long vertical line array indicate that curved wavefront replica vectors based on the sound speed profile should be used to estimate the vertical angular spectrum, especially if the arrival structure contains low arrival angles. Then, simulations involving a 900 m aperture and 128 sensors show that subaperture processing is workable and potentially worthwhile. For such an aperture, it is shown that plane wavefront replica vectors can be used without any concern of mismatch, even at high input signal-to-noise ratio, the signal-to-noise ratio at a single element (i.e. 10 dB). Processing gain and resolution performance relative to the conventional processor are quantified for various input signal-to-noise ratio scenarios. Using the Minimum Variance processor results in some reduction of the processing gain. This reduction decreases with lower input signal-to-noise ratios, as the sensitivity to mismatch of the adaptive processor decreases. Resolution enhancements can be obtained with the Minimum Variance processor at high and medium input signal-to-noise ratios (i.e. 10, -10 dB), but not for lower input signal-to-noise ratios.

#### **3.2. Introduction**

This research investigates how to process the data from large vertical line arrays such as the Marine Physical Laboratory (MPL) digital acoustic array [Sotirin; 1989], a 120 sensor array cut for 100 Hz and sampling 900 m of water column. As indicated in the previous chapters, the focus is put on how to use the adaptive Minimum Variance processor in practice. The MV processor can provide substantial resolution improvement but lacks robustness and exhibits a large sensitivity to mismatch at high input signal-to-noise ratios.

Full aperture coherent processing offers the best processing gain in theory. It is commonly performed using the conventional FFT beamformer, which is a very computationally efficient processor [De Fatta; 1988]. The FFT beamformer does across-sensor FFTs on a selected narrowband frequency to obtain angular spectra that are then averaged to achieve statistical stability. Full aperture processing with the Minimum Variance beamformer on a long and well-filled array, (i.e. with the number of sensors on the order of a hundred), can be performed, although several aspects do not appear practical. As a preliminary step, the adaptive processor requires the estimation of the array covariance matrix and needs a large number of time snapshots in order to correctly estimate an invertible covariance matrix and to control the power spectrum variance. The amount of time snapshots required by the MV processor may be well beyond the length of the data stationary sample record, especially if the signals of interest come from a moving source. Furthermore, the MV processor involves matrix operations for which computation counts have a  $N^3$  order where  $N$  is the size of the matrix [Kung; 1988]. Large computational resources may be required.

Another strategy is to process subarrays with the MV processor and incoherently recombine the corresponding angular spectra, as it is commonly done in time series spectral estimation. This approach presents several advantages: it requires less snapshots to estimate the smaller size subarray covariance matrices and less computing resources. Although the MV processor operates on smaller apertures, it could yield sufficient resolution, if not better resolution than

conventional beamforming, depending on the input signal-to-noise ratio and should enjoy a certain level of robustness as a result of incoherent averaging. In addition, this approach produces angular spectra corresponding to different windows in the water column and may provide some information on multipath variability in the vertical, if any.

The implementation of the two envisioned processing approaches is discussed below and the techniques are validated using synthetic data. The simulated data are created with an acoustic normal mode model that outputs the complex wavefield at a particular frequency for a particular source-receiver geometry. Normal mode models provide a complete solution of the wave equation including full diffraction effects [Boyles; 1984, p. 199] and should produce a realistic wavefield to process with the proposed methods. A deep water CW tone propagation experiment is simulated with two receiving array geometries. The first one is of a very long vertical line array with an aperture length over 3000 m. The second geometry involves a large vertical line array, with a length on the order of 900 m, comparable to the MPL digital array.

### **3.3. Beamformer Implementation**

The conventional beamformer and the adaptive MV processor described in Chapter 1, are used in the following. The conventional beamformer operates on the full aperture. The corresponding angular spectrum will be used as a reference. The MV processor processes the full aperture and subapertures with various spatial smoothing lengths. Two wavefront models are considered, the plane wavefront and the curved wavefront based on the sound speed profile across the array, as developed in Chapter 2. The angular spectra, produced by the various processors using the two wavefront models, are referenced to a particular depth and sound speed in order to be intercompared. Here, the reference depth is taken at the sound speed minimum across the whole water column (i.e. the sound axis depth). The receiving arrays are deployed across the sound axis at a known absolute depth.

#### **3.3.1. Using Planar Wavefronts**

The planar wavefronts, referenced to the sound axis depth and sound speed, are generated using Equation (2.22). The differential phase across the array depends only on the reference sound speed and the reference depth just introduces an unimportant phase shift. This is consistent with the FFT implementation of the conventional processor (c.f. Equation (1.12)) which produces a power spectrum in normalized wavenumber or electrical angle, then transformed into physical angles through a nonlinear mapping (given by Equation (1.9)) involving only the reference sound speed. A Kaiser-Bessel window with  $\alpha$  parameter of 1.5 is used to weight the aperture, prior to the conventional beamforming to control the sidelobe level to -35 dB. The MV processor is directly implemented with the quadratic form in Equation (1.36). In the case of processing the full aperture with planar wavefronts, the replica vectors are created according to the efficient aperture length after spatial smoothing using the sound axis sound speed as reference.

Subaperture processing requires the computation of a reference sound speed for each subaperture in order to compute its associated plane wave replica vectors. The reference sound speed can be the mid-subarray sound speed, the arithmetic or harmonic sound speed average across the subarray. Because the relative difference in sound speed is small anyway, any choice appears acceptable for producing the planar replica vectors. The harmonic sound speed is used here [Polvani; 1984]. Since different averaged sound speeds are associated with each subaperture, a first order correction is necessary to take into account ray bending and insure that the arrivals are properly aligned from one subaperture to another. The mapping is performed

by applying a correction based on Snell's law which shifts and aligns the peaks of the angular spectra which then can be incoherently averaged to produce a composite angular spectrum. For example, assume a two non-overlapping subaperture case where the upper subaperture has a lower reference sound speed than the the lower subaperture. Then, denote  $P_{up}(\theta_{up})$  and  $P_{low}(\theta_{low})$  the angular spectra of the upper and lower apertures.  $P_{low}$  is remapped for a sound speed deviation from  $c_{low}$  to  $c_{up}$  using Snell's law

$$\frac{\cos(\theta_{low})}{c_{low}} = \frac{\cos(\theta_{up})}{c_{up}} \quad (3.1)$$

Since  $P_{low}$  is evaluated on a regular grid in  $\theta_{low}$  angles, which actually correspond to an irregular grid in  $\theta_{up}$  angles referenced to  $c_{up}$ , one just needs to do an interpolation to go from an irregular angular grid back to a regular grid. This procedure is summarized in Figure 3.1. The result for  $P_{low}$  is large angular shifts for low angles and small angular shifts for steep angles with respect to the horizontal. The low angle arrivals for the lower aperture corresponds to steeper angle arrivals for the remapped lower aperture and very low angle sound may not exist. One must note at this point that small variations in the subarray reference sound speeds may result in large shifts in angles, especially for low arrival angles (below  $10^\circ$ ). The harmonic sound speed was found to produce a very good alignment of the subaperture peaks.

### 3.3.2. Using Curved Wavefronts

Curved wavefront beamforming, proposed in Chapter 2, is summarized here. The sound speed profile, assumed known across the array, is used in Equation (2.21) to create the curved wavefront replica vectors corresponding to the full aperture. If the ray corresponding to a particular angle at the sound axis has turned over and does not insonify part of the array, the non-insonified sensors or rows in the array manifold matrix have zero entries. When the Bartlett processor beamforms the data, a Kaiser-Bessel window with  $\alpha$  parameter of 1.5 is used to weight the insonified part of the array like in the plane wave case. Care is necessary to ensure proper normalization of the power spectrum. if the top  $n_1$  sensors and the bottom  $n_2$  sensors are not insonified by a particular steering vector  $\mathbf{E}_c$ , the curved wavefront conventional processor is

$$P_{Kaiser} = (\mathbf{W} \mathbf{E}_c)^H \mathbf{R} (\mathbf{W} \mathbf{E}_c) \quad (3.2)$$

where  $\mathbf{E}_c$  and  $\mathbf{R}$  are defined as before,  $\mathbf{W}$  is defined by

$$\mathbf{W} = \begin{bmatrix} \mathbf{O}_{n_1, n_1} & \mathbf{O}_{n_1, M_i} & \mathbf{O}_{n_1, n_2} \\ \mathbf{O}_{M_i, n_1} & \mathbf{w}_{M_i, M_i} & \mathbf{O}_{M_i, n_2} \\ \mathbf{O}_{n_2, n_1} & \mathbf{O}_{n_2, M_i} & \mathbf{O}_{n_2, n_2} \end{bmatrix} \quad (3.3)$$

where  $\mathbf{O}_{n_i, n_j}$  is a matrix with only zero entries and size  $n_i$  by  $n_j$ , and  $\mathbf{w}_{M_i, M_i}$  is given by

$$\mathbf{w}_{M_i, M_i} = \frac{1}{\sum_{i=0}^{M_i-1} a_i} \begin{bmatrix} a_0 & 0 & \dots & 0 \\ 0 & a_1 & \dots & \cdot \\ \cdot & \cdot & \dots & \cdot \\ \cdot & \cdot & \dots & \cdot \\ \cdot & \cdot & \dots & 0 \\ 0 & 0 & \dots & a_{M_i-1} \end{bmatrix} \quad (3.4)$$

where the  $a_i$ 's are the Kaiser-Bessel window coefficients weighting the  $M_i$  insonified sensors of the array,  $M_i = M - n_1 - n_2$ .

When the MV processor is used to process the full aperture, the eigensteering vector corresponding to each curved wavefront replica vector must be computed to avoid mismatch due to spatial smoothing. The array covariance matrix corresponding to each replica vector is passed through spatial smoothing, the smoothed matrix is decomposed in eigenvalues and eigenvectors and the unit-norm eigenvector  $\mathbf{E}_e$  corresponding to the largest eigenvalue is stored in the eigen array manifold. Therefore, a large number of computations is required for each smoothing scenario. As in the case of the Bartlett processor, care is necessary to correctly normalize the power spectrum. The Minimum Variance power spectrum is given by

$$P_{MV} = \frac{1}{s_i(\mathbf{E}_e)} \frac{1}{\mathbf{E}_e^H T(\mathbf{R})_s^{-1} \mathbf{E}_e} \quad (3.5)$$

where  $T(\mathbf{R})_s$  is the spatially smoothed covariance matrix on  $s$ -sensor subarrays and  $s_i(\mathbf{E}_e)$  is the number of sensor actually insonified by an arrival with replica vector  $\mathbf{E}_e$ .

When subapertures are processed, the part of the full aperture curved wavefront replica vectors that corresponds to a particular subaperture is used to create the corresponding eigensteering vectors. The subaperture angular spectra then are computed as in the full aperture MV angular spectrum using their respective eigen array manifold. The subaperture spectra can then be directly averaged together since they correspond to the same depth and sound speed references. Therefore, there is an interesting benefit of using curved wavefront replica vectors compared to plane wavefront replica vector. The remapping operation of the angular spectra (associated with a particular subarray and a particular constant sound speed), which inherently is sensitive to the subaperture sound speeds, is avoided. The disadvantage is the large computational complexity since an eigenvalue-eigenvector decomposition is required for each beam in order to compute the eigen array manifold.

### 3.4. Processing a Very Large Vertical Line Array

#### 3.4.1. Modeling the Environment

The simulated data created by the ATLAS normal mode model [Gordon; 1985], corresponds to a range independent deep water environment with a water depth of 4667 m. The sound speed profile, plotted in Figure 3.2, is characteristic of the North-East Pacific, with a sound axis around 500 m. The critical depth of this oceanic waveguide is on the order of 3313 m. Thus, the sound channel has a depth excess and convergence zone propagation may take place. The bottom is characterized by a frequency invariant bottom loss table (bottom loss in dB as a function of incidence angle), given in Table 3.1, which corresponds to a Generic Sonar Model (GSM) Province Type 3 [Weinberg; 1985]. A 5 m deep omnidirectional source is projecting a 20 Hz CW tone with a source level of 200 dB re 1  $\mu$ Pa at 1 m. The environment is assumed to be noise free. The very long vertical line array is cut for 30 Hz with an interelement spacing of 25 m, has 128 equi-spaced sensors and extends across most of the water column from 100 m to 3275 m. It has its sensors numbered from top to bottom so that at the output of the beamformers positive angles of arrival correspond to downlooking beams or upgoing sound. This receiving array is assumed deployed 56 km from the source in its first convergence zone. The geometry is summarized in Figure 3.3. The analysis and interpretation of these synthetic data [Tran; 1989b] are performed with the ATLAS

normal mode model and the GSM ray model [Weinberg; 1985] using the continuous gradient approximation of the sound speed profile (CONGRATS). The GSM is used to cross-check the ATLAS results. A fair agreement was found between the two models, although the ray model reports a well defined convergence zone around 56 km, while the normal mode model does not. The GSM produces ray diagrams which can be compared to the beamformer outputs. The eigenrays connecting the source to the array receivers, between  $-45^\circ$  and  $45^\circ$ , are plotted in Figure 3.4. The sign convention of the GSM eigenrays is the same as for the beamformers, positive angle eigenrays are propagating upward (i.e. the signs are flipped with respect to the original Generic Sonar Model results). The effect of ray bending with depth is clearly observed for the rays with smaller angles with respect to the horizontal.

### **3.4.2. Processing Results**

#### **3.4.2.1. Conventional Beamforming**

The angular spectra produced by the conventional beamformer using the plane and curved wavefront replica vectors are overlaid in Figure 3.5 with the GSM eigenrays at the sound axis. Since no noise is included in the simulation, over twelve multipath arrivals are resolved, mostly between  $-30^\circ$  and  $30^\circ$ . Using either curved or planar wavefront replica vectors gives similar results but some arrivals are reported at slightly different angles, even with the reference taken at the sound axis in all cases. The GSM eigenray structure at the sound axis is similar to the angular spectra although the eigenray peak powers are higher than the ATLAS spectrum peaks. This is consistent with the modeling results. When curved wavefront replica vectors are used, the two arrivals near  $-15^\circ$  and  $20^\circ$  are better resolved and their directions of arrival are closer to the GSM eigenray angles. The conventional beamformer using curved wavefront replica vectors reports high power levels at near horizontal angles. This is due to the partial insonification of the aperture which results in higher sidelobes and lower resolution. The insonified part of the 128 element array is plotted in Figure 3.6 as a function of arrival angle. Near horizontal arrivals insonify a very limited part of the aperture, if not a single sensor (# 13). Since the beamwidth of a few sensor array steered in a near horizontal direction is large, power corresponding to steeper arrivals is reported at low angle of arrival.

#### **3.4.2.2. MV Processing**

This simulation does not include noise and therefore corresponds to an "infinite" signal-to-noise ratio. In such conditions, the MV processor exhibits a large sensitivity to mismatch, and only curved wavefront replica vectors are used in the following. The angular spectrum produced by the full aperture MV beamformer after spatial smoothing on 64 sensors is overlaid in Figure 3.7 with the GSM eigenrays and the conventional processor using curved wavefront replica vectors. A large amount of smoothing is necessary to decorrelate a cluster of over a dozen multipaths. The MV peak powers of the arrivals are up to 20 dB lower than the ones produced by the conventional processor. Since a large amount of spatial smoothing has been performed and eigensteering vectors are utilized, this loss is thought to be the result of an insufficient sampling in angle (only 256 beams are used between  $-90^\circ$  and  $90^\circ$ ). Improvement in resolution is observed clearly compared to the conventional processor, even with the efficient smoothed aperture reduced by half.

As in the case of the conventional curved wavefront processor, an increase in power near horizontal angles is due to the partial insonification of the equivalent smoothed aperture, as shown in Figure 3.8 where the insonified efficient aperture is plotted.

The processing results, produced by the MV processor on 32-sensor subarrays, after spatial smoothing on 20 sensors and with the eigensteering vectors, are presented in a waterfall plot in Figures 3.9. The angular spectra correspond to 48 subarrays sliding from the top to the bottom of the full aperture by two elements (i.e. the first subarray extends from sensor 1 to 32, the second subarray extends from sensor 3 to 34 and so on...) and are all referenced to the sound axis. The flat area at low angles corresponds to an angular region where no arrival or sound can physically exist, according to the ray geometric approach selected here. It is the result of the partial insonification discussed earlier. The peak power estimates are lower than the ones reported by the conventional processor because of signal cancellation (the subarrays are shorter and allow only limited multipath decorrelation), and insufficient angular sampling (as in the case of full aperture processing, only 256 beams are used). A great variability in the detected arrivals is observed from subarray to subarray, even though all the spectra are referenced to the sound axis. It is largest in the upper half and the middle of the 128 sensor aperture. As a result, the incoherent averaging of the subarray angular spectra smears the peaks in the spectrum [Tran; 1989b].

### **3.4.3. Conclusions**

These simulations on a very large vertical line array indicates that using curved wavefront replica vectors with the conventional processor can enhance the resolution of some arrivals, especially the ones with small angles with respect to the horizontal. Full aperture MV processing using the eigensteering vectors produces, as expected, a resolution enhancement in this pure signal environment. Subaperture processing with the MV processor and the eigensteering vectors appears to be viable scheme. It indicates the large variability with depth of the multipath arrivals which characterizes the particular simulated geometry. Thus, averaging incoherently the subapertures does not necessarily enhance the peaks.

### **3.5. Processing A Large Vertical Line Array**

#### **3.5.1. Modeling Results**

The simulated environment is the same as in the previous Section. But the propagation experiment now involves a shorter aperture array with 128 sensors, cut for 107 Hz with an interelement spacing of 7 m. The vertical line array is deployed from 300 to 1189 m. The source is deployed at 5 m depth and 56 km range, and projects a 100 Hz CW tone with a level of 200 dB re  $\mu\text{Pa}$  at 1 m. The geometry of the propagation experiment is summarized in Figure 3.3. As before, the acoustic modeling is performed with the ATLAS normal mode model and the GSM ray model [Tran; 1989b]. Both models indicate a convergence zone between 50 and 60 km, which is better defined in the ray solution than in the normal mode results. The GSM eigenrays that connect the source to the array receivers are plotted in Figure 3.10, where positive angle eigenrays are upgoing. The eigenray arrival structure does not vary significantly over depth as in the case of the very large array which was three times larger.

#### **3.5.2. Processing Results**

##### **3.5.2.1. Conventional Beamforming**

The array aperture is smaller, hence the effects of the wavefront curvature have a lesser impact. The angular spectra referenced to the sound axis produced by the conventional beamformer, using planar and curved wavefront replica vectors are overlaid in Figure 3.11 with the GSM eigenrays. The angular spectra are identical whether curved or plane wavefront replica vectors are used, except for the spurious horizontal arrival due to the partial insonification of the aperture by curved wavefront arrivals. The  $0^\circ$  curved arrival insonifies only three sensors [Tran; 1989b]. The ATLAS angular spectra closely match the GSM eigenray structure. In addition to the good fit of the directions of arrival, the absolute power levels of the ATLAS spectral peaks and the GSM eigenrays are similar.

##### **3.5.2.2. MV Processing**

The angular spectrum produced by the MV beamformer processing the full aperture and using eigensteering vector that correspond to a spatial smoothing on 64 sensors, is overlaid in Figure 3.12 with the spectrum of the conventional processor using curved wavefront replica vectors and the GSM eigenrays. In this pure signal simulation, using the adaptive processor yields much better resolution. The peak power levels produced by the adaptive processor are up to 20 dB lower than the conventional processor levels. As mentioned already, this is probably mismatch loss resulting from an insufficient  $0.7^\circ$  sampling in angle. The slight increase of power at low arrival angles corresponds to the partial insonification of the equivalent smoothed aperture, only 32 sensors of the equivalent smoothed aperture are insonified.

The results of processing 32-sensor subapertures with the MV method using the eigensteering vector for a spatial smoothing on 20 sensors, are presented in Figure 3.13. These 48 spectra, corresponding to 32 sensor subarrays sliding by two sensors from the top to the bottom of the full aperture, are referenced to the sound



axis. The reduction of the aperture limits the amount of spatial smoothing, hence, the number of peaks in Figure 3.13 is roughly half of what is detected with full aperture coherent processing. Mismatch is apparent with peak levels up to 20 dB below the conventional processor peak levels. The stronger and lower angle arrivals are stable with depth and they are enhanced when the incoherent average of the 48 angular spectra is computed. The composite angular spectrum is plotted in Figure 3.14 and has low angle arrival levels on the same order as the full aperture MV processor levels.

### **3.5.2.3. Conclusions**

These simulations show that for a shorter aperture and for a typical arrival structure with arrivals steeper than  $10^\circ$ , there is no need to use curved wavefronts with the Bartlett (conventional) processor. Beamforming the full aperture with the adaptive processor and curved wavefronts produces a large increase in resolution compared to conventional beamforming. Subaperture processing seems to perform as indicated in Section 3.2. The main features of the arrival structure are stable with depth, therefore incoherent averaging produces some processing gain.

### **3.5.3. Signal-Plus-Noise To Noise Ratio Performance Study**

#### **3.5.3.1. Introduction**

Until now, no component of noise has been included. Since the MV processor is very sensitive to mismatch in a high signal-to-noise ratio environment, only curved wavefronts (modified to account for spatial smoothing) have been used. The conventional beamforming results are identical whether or not plane or curved wavefront replica vectors are used. Thus, one can question if using curved wavefront replica vectors is actually necessary. A way to answer this question is to measure, for a realistic input signal-to-noise ratio (SNR) the mismatch loss (if any) when curvature is neglected. This is performed through a peak level performance study, which will also indicate the relative processing gain performance of the various processors. This study is performed only on the 900 m aperture case in preparation to processing real data from the MPL digital array (Chapter 4).

#### **3.5.3.2. Description of the Simulation**

The synthetic pressure field, created by the ATLAS model, is embedded in a spatially white noise or sensor noise with three different input signal-to-noise ratio (SNR): -18 dB, -11 dB and 9 dB. A spatially white noise structure corresponds to a noise field dominated by strong surface generated noise produced by high wind speed conditions. To measure the potential mismatch caused by using planar wavefront replica vectors, the number of beams in this study is increased to yield a very fine sampling in angle. A  $0.022^\circ$  quantization, which corresponds to 4096 beams between  $-45^\circ$  and  $45^\circ$  was found sufficient [Tran; 1989c]. For each input SNR, the field is processed by the conventional FFT beamformer, the MV processor operating on the full aperture after spatial smoothing on 92, 78 or 64 sensors, and finally by the MV processor operating on two non-overlapping subapertures after spatial smoothing on 48 or 32 sensors. For each processing scheme, the peak level or output signal-plus-noise level of each arrival is measured relative to the output

noise level. This relative peak level is a biased measure of the output SNR at low input SNR, but is a reliable indicator of the output SNR at high input SNR. Since in this simulation the covariance matrices are perfectly known, very low level arrivals with negative output signal-to-noise ratio can be detected against the flat background noise, and are included in the analysis for completeness, although in a real situation, these arrivals would be covered by the noise fluctuations. The signal-plus-noise to noise ratios of the arrivals detected with the various methods are compared to the corresponding arrival peak levels produced by the conventional FFT beamformer. The results are summarized in Figures 3.15, 3.16 and 3.17 for the -18, -11 and 9 dB input SNR.

### **3.5.3.3. Results**

#### **Plane Versus Curved Wavefronts**

A first inspection of the simulation results shows that there is no noticeable difference whether planar or curved (modified to account for spatial smoothing) wavefront replica vectors are used. There is no mismatch associated with planar wavefront replica vectors, even for high input SNR, for this typical arrival structure and 900 m aperture. Thus, plane wavefronts can be used with the Minimum Variance processor.

#### **Full Aperture Processing Analysis**

The output signal-plus-noise to noise ratio (relative peak level) produced by the MV processor is generally below the conventional processor relative peak level. This loss increases with increasing relative peak levels which is not surprising since the sensitivity of the MV processor to mismatch increases with SNR. At low and medium input SNR, the reduction in output signal-plus-noise to noise ratio is on the order of half a dB and a dB, respectively. The multipaths have been well decorrelated by spatial smoothing, since in those two cases, there is more loss when the spatial smoothing length is decreased. The high input SNR case has the same behaviour, except for arrivals above 20 dB, where the relative peak level reduction is largest, on the order of 8 dB, for a smoothing length of 92. That loss is reduced to 3 dB when larger smoothing lengths are used, which indicates a signal cancellation limited situation. The largest arrival around 15° actually corresponds to a cluster of arrivals (c.f. Figure 3.11).

#### **Subaperture Processing**

Processing two subapertures with the MV beamformer produces a reduction of the output signal-plus-noise to noise ratio, compared to the Bartlett processor operating on the full aperture. The loss is on the order of half a dB for low level arrivals (i.e. arrivals with a relative peak level below 2 dB) and on the order of a few dB for medium level arrivals (arrivals with relative peak levels between 3 and 10 dB), and up to 6 dB for large level arrivals (arrivals with relative peak levels above 10 dB).

### 3.5.3.4. Array Gain Calculations

Assuming that the detection of the signals is based on the highest peak level arrival, one can estimate the array gain achieved by the array processed by the various beamformers. The array gain is given by the signal-to-noise ratio at the output of the beamformer divided by the input signal-to-noise ratio at the individual phones. The input signal-to-noise ratios are fixed in the simulation. The highest output signal-to-noise ratio can be easily derived from the highest relative peak level measured in the angular spectra by subtracting the contribution of the noise. The estimates of the array gain are plotted in Figure 3.18 for the various methods. They are always lower than  $10 \log M$ , or 21 dB, the theoretical array gain assuming uncorrelated arrivals of a known wavefront in an incoherent noise field [Urick; 1983, p. 37, Ziomek; 1985, p. 121]. The array gain of the Bartlett processor is constant with input SNR and equal to 14 dB. For low and medium SNRs (-18 and -11 dB), the array gain of the MV processor is close to the Bartlett processor array gain, and essentially the same for the low and medium input SNRs (-18 and -11 dB), with a reduction on the order of 2 dB and 3.5 dB when processing two subarrays with spatial smoothing lengths equal to 48 and 32. This degradation of the array gain is consistent with the estimates of the reduction of the processing gain obtained using the conventional formulas of  $10 \log m$  for coherently processing  $m$  sensors and of  $5 \log n$  for incoherently averaging over  $n$  estimates. The estimated processing gain reductions are 2.7, and 4.5 dB for processing two subapertures with spatial smoothing lengths equal to 48 and 32 sensors. In the case of the high input SNR, the array gain of the Minimum Variance processor is lower as a result of mismatch. The poor performance of the processor may also be due to a signal cancellation problem. As noted earlier, the highest level arrival actually corresponds to a cluster of arrivals very close together which is hard to decorrelate even after heavy spatial smoothing. The reduction of the array gain is on the order of 6 dB when processing two subapertures.

### 3.5.4. Resolution Study

Using the MV processor results in some processing gain degradation which, in some cases, is compensated for by a better resolution. To quantify when enhanced resolution is achieved compared to the conventional processor, a simulation focussed on resolution is now presented.

#### 3.5.4.1. Description of the Study

As in the previous sections, the Bartlett processor is used as a reference against which is compared the MV processor, operating on the full aperture (after spatial smoothing on 92, 78 and 64 sensors) and on two non-overlapping subapertures (after spatial smoothing on 48 and 32 sensors). Resolution for each arrival is measured here through a relative resolution measure with respect to the conventional beamformer. The relative resolution factor for a particular arrival is defined as

$$\frac{BW(X) - BW(\text{Bartlett})}{BW(\text{Bartlett})} \quad (3.6)$$

where  $BW(X)$  is the 0.1 dB beamwidth of the considered arrival for method  $X$ . When the relative resolution factor is negative, method  $X$  yields better resolution than the conventional processor. A relative resolution factor of -1 means that the resolution of method  $X$  is two times better than the conventional processor.

Since it was found that there is no advantage of using curved wavefront replica vectors for the 900 m aperture array, only plane wavefront replicas are used in this resolution study. As before, 4096 beams between  $-45^\circ$  and  $45^\circ$  are used, yielding a sampling interval in angle of  $0.022^\circ$ . The relative beamwidth is computed from the 0.1 dB beamwidths of each arrival (interpolated if necessary) and plotted against the Bartlett signal-plus-noise to noise ratios for each input SNR in Figure 3.19, 3.20 and 3.21.

#### **3.5.4.2. Results**

##### **Full Aperture Processing**

The MV processor produces a much better resolution than the Bartlett processor at high signal-to-noise ratios. This is illustrated by the 9 dB input SNR case where the arrivals with output signal-plus-noise to noise ratios larger than 5 dB are much better resolved with the MV processor, whatever the spatial smoothing length. In the medium input SNR case (-11 dB), the resolution has decreased to the same order as the Bartlett processor. Using a spatial smoothing length of 64 results in a degradation of resolution, compared to full aperture conventional processing. This trend is confirmed by the lower input SNR case (-18 dB), where a larger spatial smoothing length would be more appropriate. Therefore, the reduction of the efficient aperture length because of spatial smoothing may result in no resolution improvement, even at medium input SNRs.

##### **Two Subaperture Processing**

The separation of the array into two subapertures results in large degradation of resolution as shown in Figure 3.20. The MV processor operating on the subapertures is able to produce a better resolution than the conventional processor only for arrivals with high output signal-plus-noise to noise ratios. At low input SNR, the MV processor produces a rather poor resolution.

#### **3.5.5. Conclusions**

This study shows that full aperture MV processing can provide a substantial improvement in resolution compared to conventional processing at high (9 dB) and medium (-11 dB) input SNR, but that it does not for the low (-18 dB) input SNR case. The improvement in resolution for large level arrivals is associated with a large reduction of output signal-plus-noise to noise ratio, as a result of mismatch and signal cancellation. Slight degradation of the relative peak levels for low level arrivals was observed as a result of the reduction of the efficient aperture due to spatial smoothing.

Subaperture processing on two subarrays has better resolution than conventional beamforming for the highest level arrivals in the high input SNR case. Splitting the array in two halves results in some degradation of the resolution and also some loss in output signal-plus-noise to noise ratios, with a half dB loss for the low input SNR case, a few dB loss for the medium input SNR case, and up to a 6 dB loss for the high input SNR case.

Angle (deg)	Loss (dB)
0°	0
10°	0.4
20°	3.20
30°	5.20
40°	6.80
50°	7.60
60°	8.20
70°	8.20
80°	8.40
90°	8.40

**Table 3.1:** Bottom Loss Table (GSM Province Type 3 [Weinberg; 1985]).

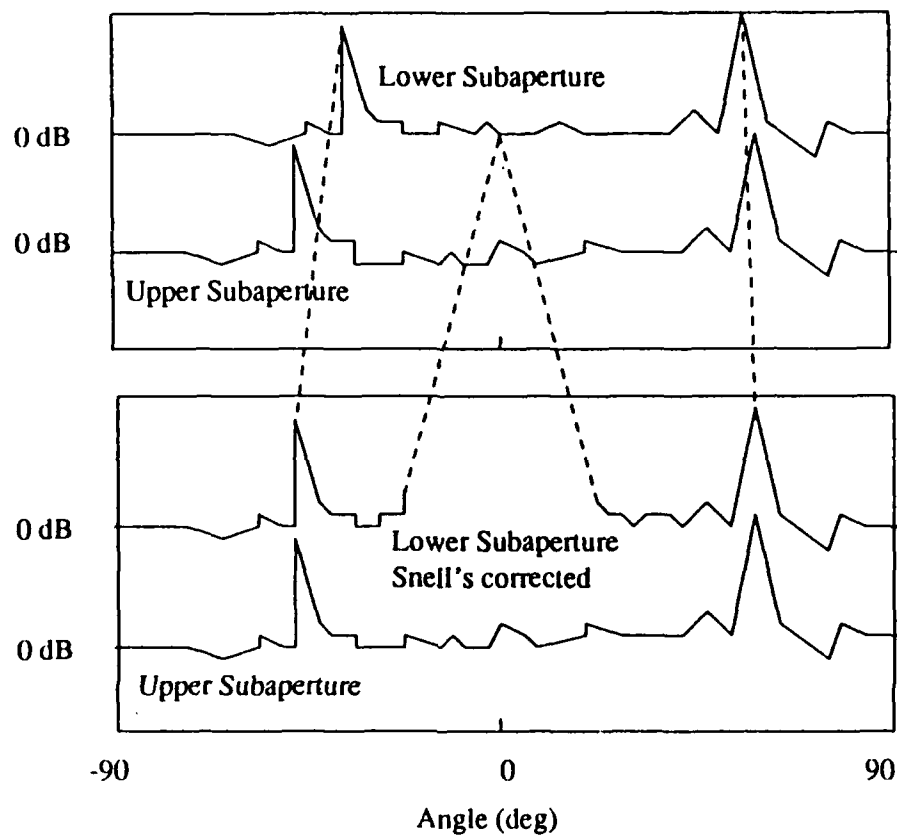


**Figure 3.1:** Snell's law remapping.

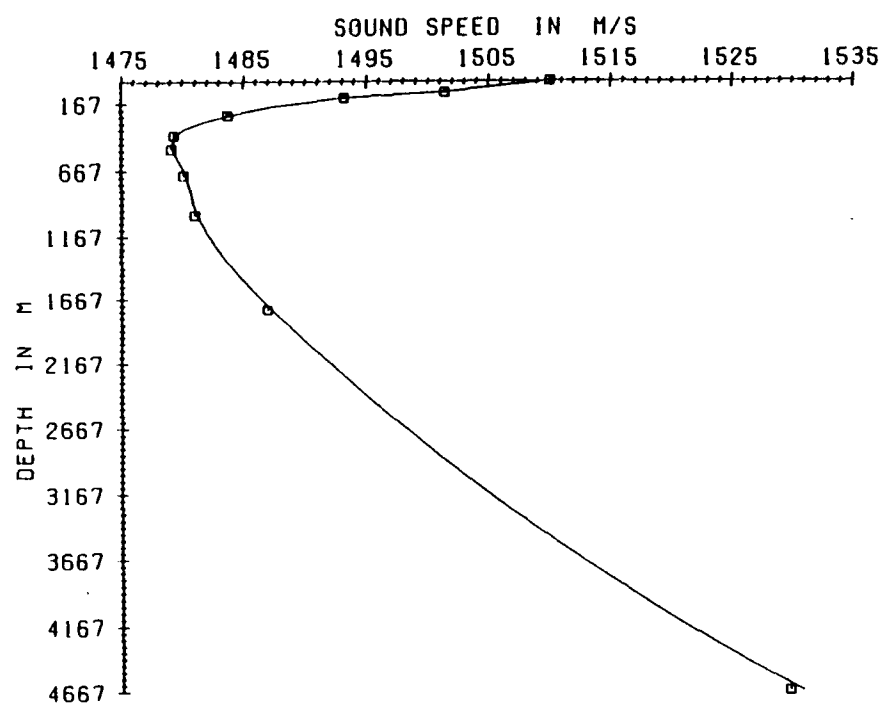


**Figure 3.2:** North-East Pacific historical sound speed profile.

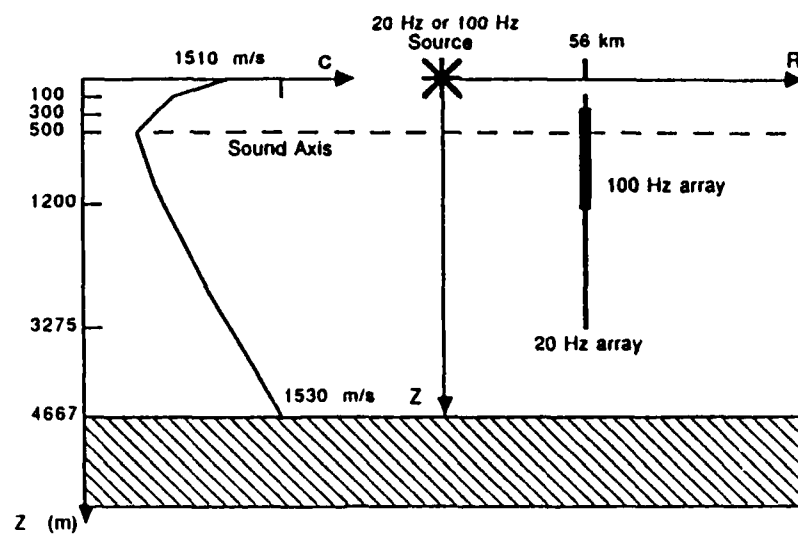
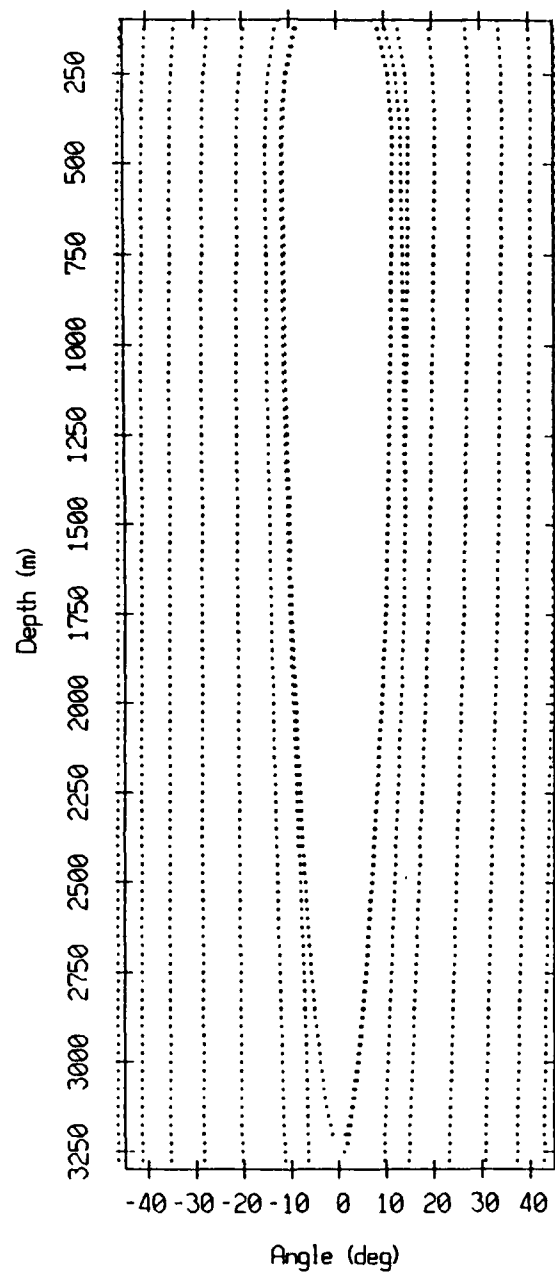
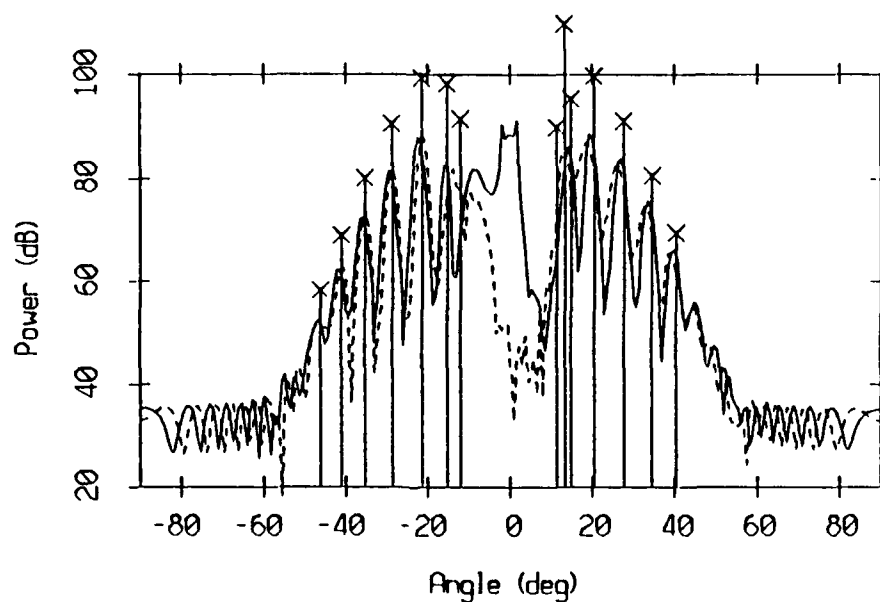


Figure 3.3: Propagation experiment geometry.





**Figure 3.4:** GSM eigenrays across the very large vertical line array.



**Figure 3.5:** Conventional beamformer output. The curved (solid line) and plane wavefront (dotted line) angular spectra are overlaid with the GSM eigenrays.

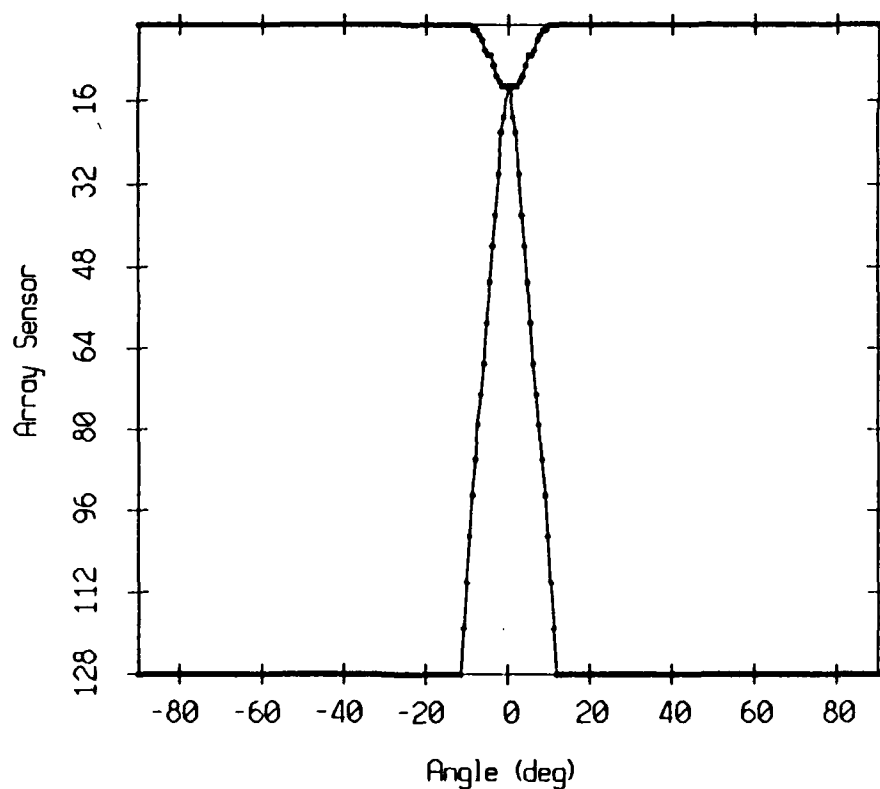


**Figure 3.6:** Full aperture curved wavefront array manifold.

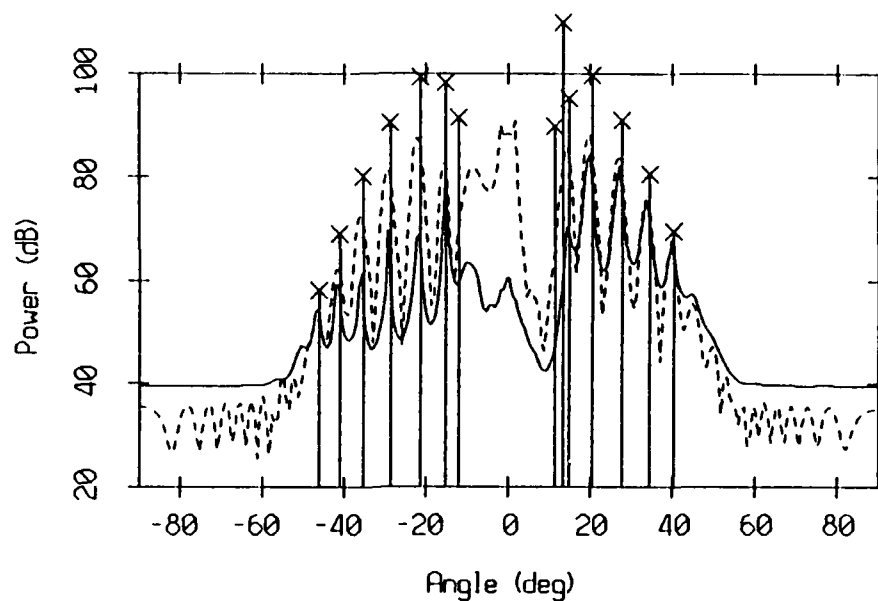


**Figure 3.7:** MV processor output after spatial smoothing on 64 sensors. The curved wavefront MV processor output (solid line) is overlaid with the curved wavefront conventional processor output (dotted line) and the GSM eigenrays.

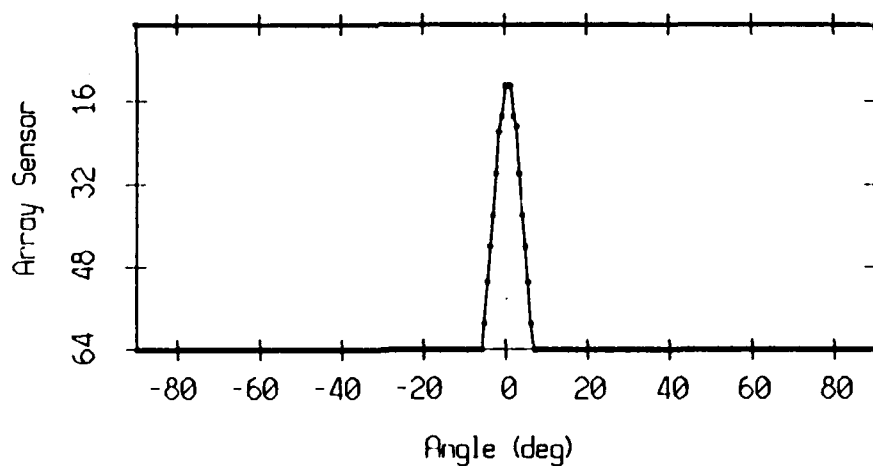


**Figure 3.8:** Equivalent Array manifold after spatial smoothing on 64 sensors.

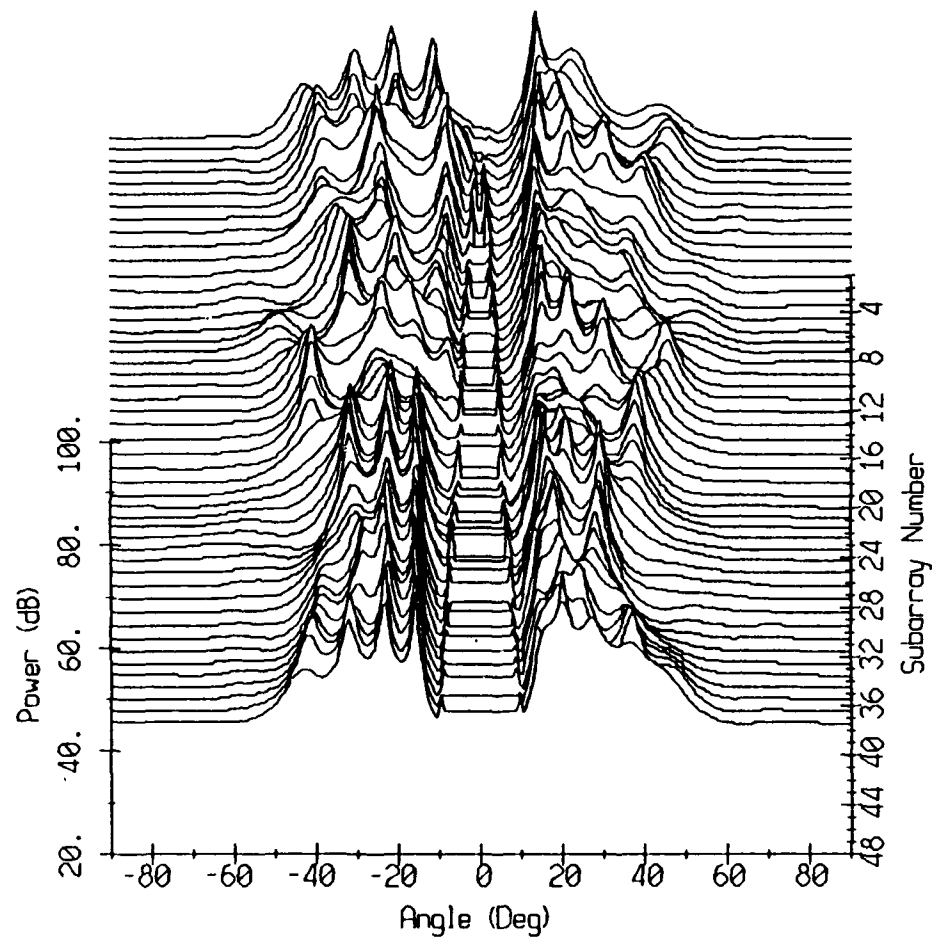


**Figure 3.9:** Spectra waterfall calculated by the MV processor on 32-sensor subarrays (after spatial smoothing on 20 sensors).

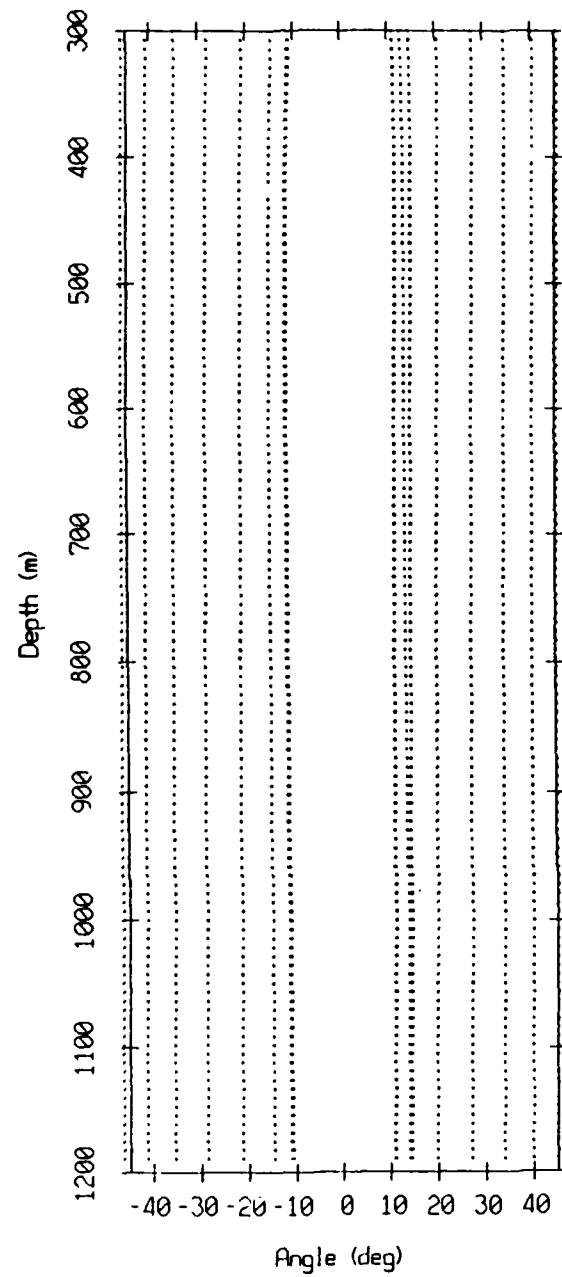


**Figure 3.10:** GSM eigenrays across the large vertical line array.

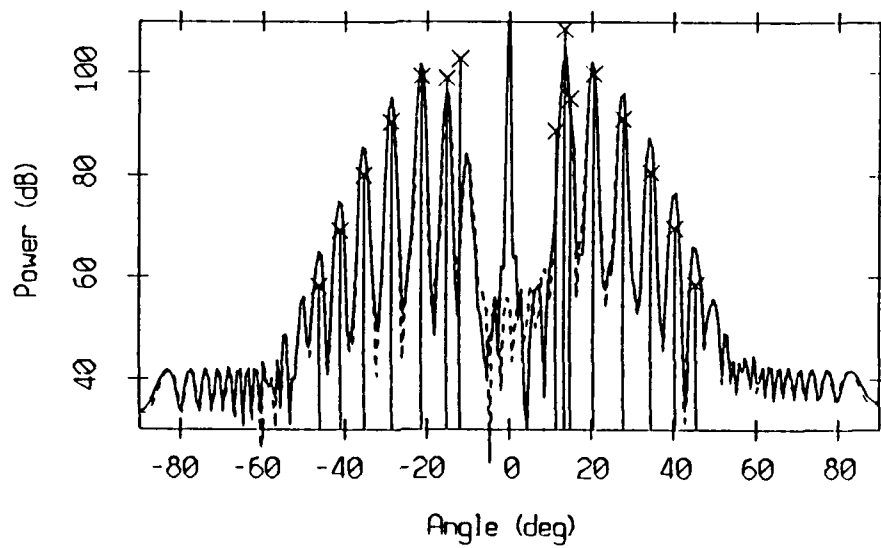


**Figure 3.11:** Conventional beamformer output. The curved (solid line) and plane wavefront (dotted line) angular spectra are overlaid with the GSM eigenrays.

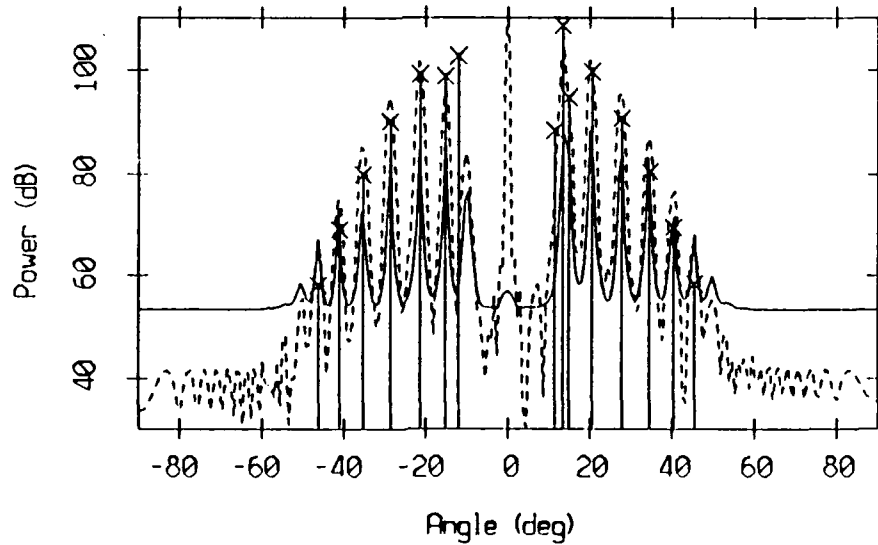


**Figure 3.12:** MV processor output after spatial smoothing on 64 sensors. The curved wavefront MV processor output (solid line) is overlaid with the curved wavefront conventional processor output (dotted line) and the GSM eigenrays.

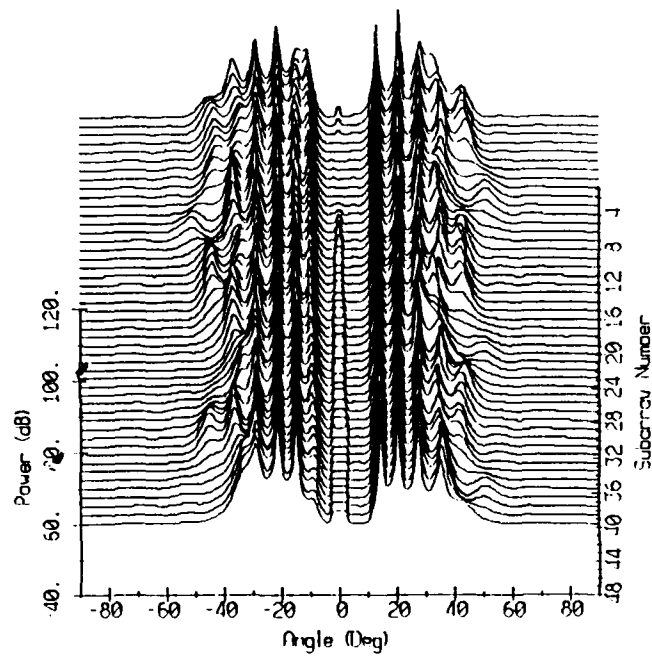


**Figure 3.13:** Spectra waterfall computed by the MV processor on 32-sensor subarrays (after spatial smoothing on 20 sensors).

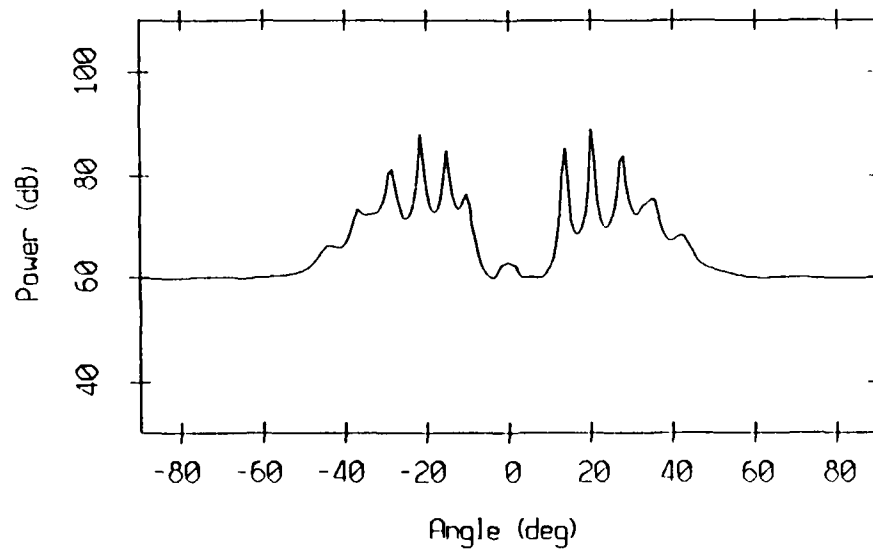


**Figure 3.14:** Average of the subaperture MV spectra.

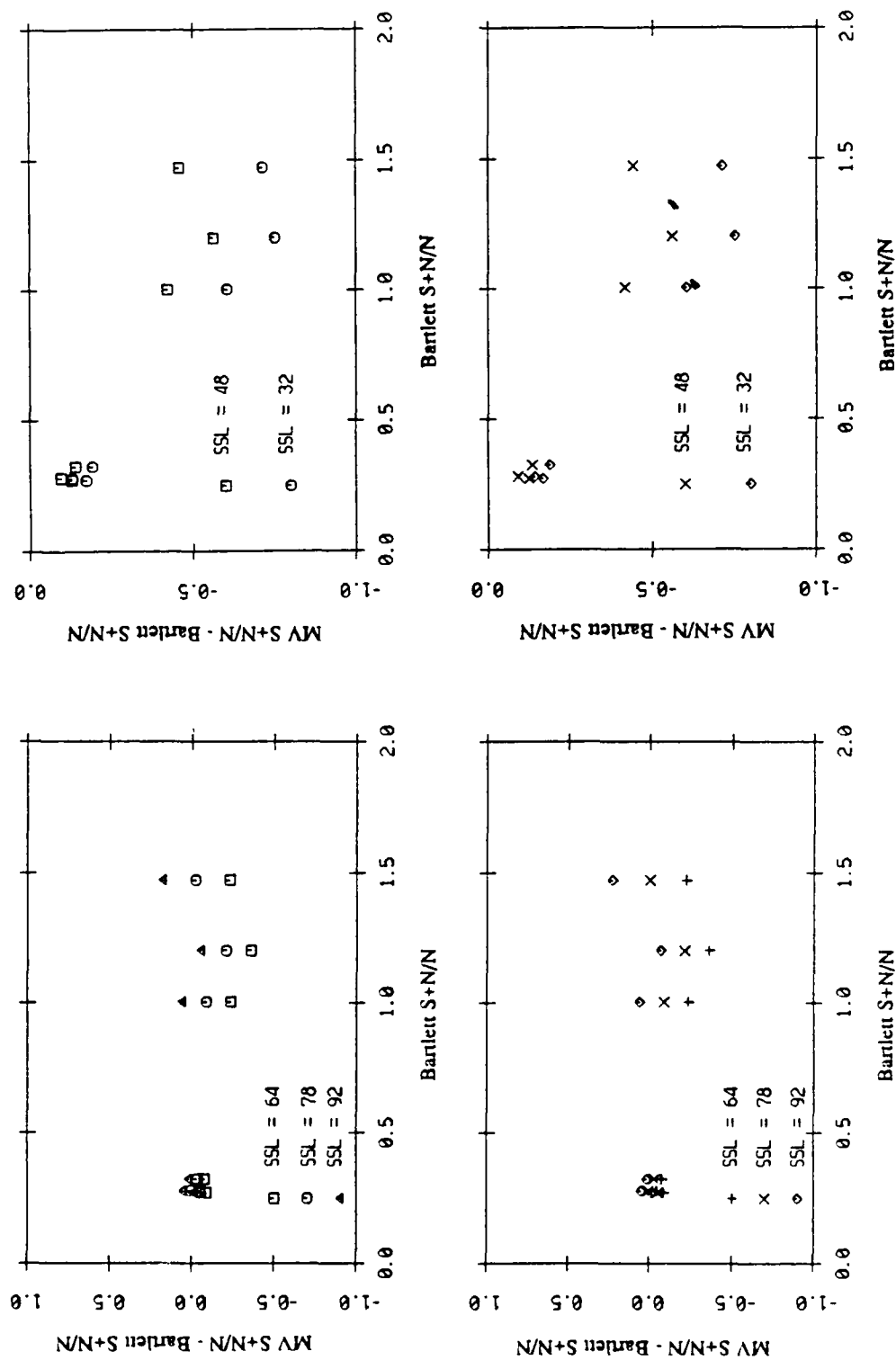


**Figure 3.15:** Peak level performance study for a -18 dB input SNR. Left panels: full aperture processing, right panels: subaperture processing. Upper panels: eigensteering vectors, lower panels: plane wave replicas.



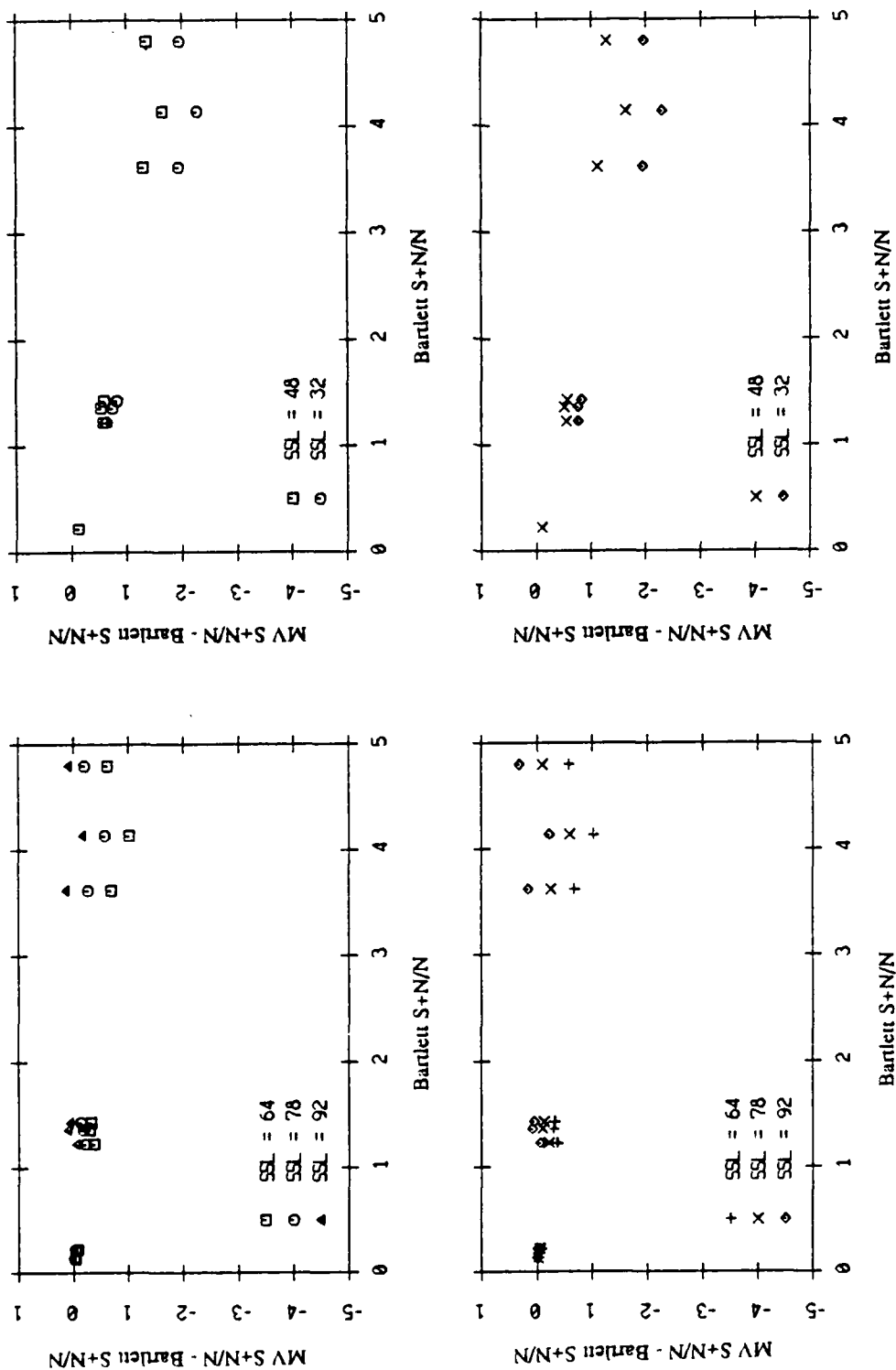


**Figure 3.16:** Peak level performance study for a -11 dB input SNR. Left panels: full aperture processing, right panels: subaperture processing. Upper panels: eigensteering vectors, lower panels: plane wave replicas.

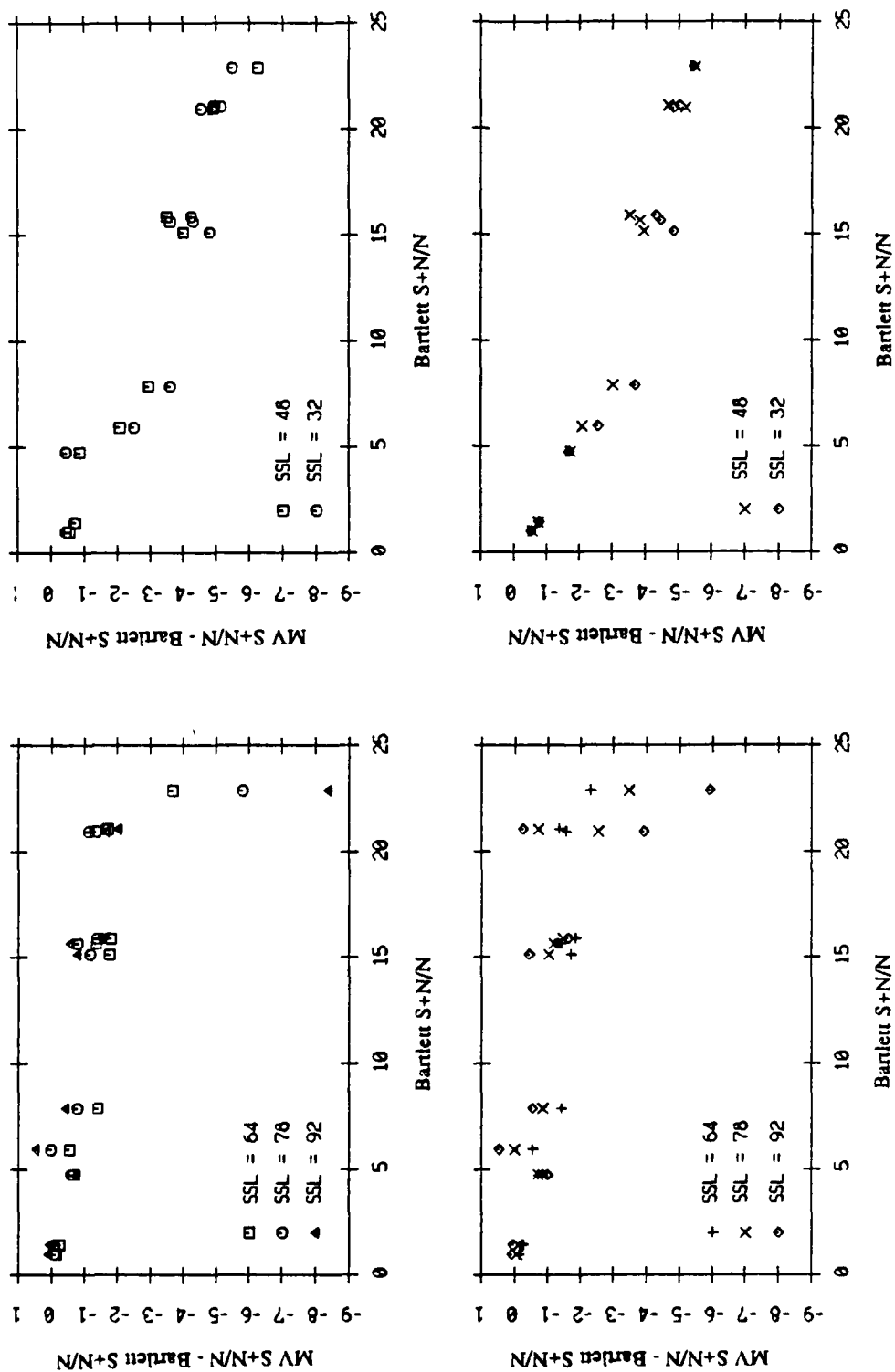


**Figure 3.17:** Peak level performance study for a 9 dB input SNR. Left panels: full aperture processing, right panels: subaperture processing. Upper panels: eigensteering vectors, lower panels: plane wave replicas.

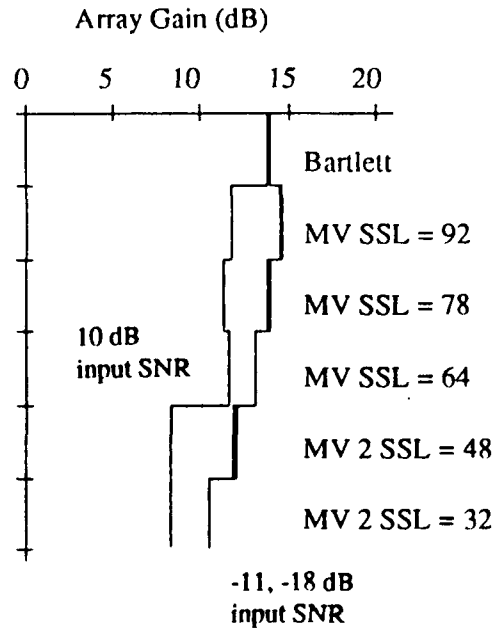
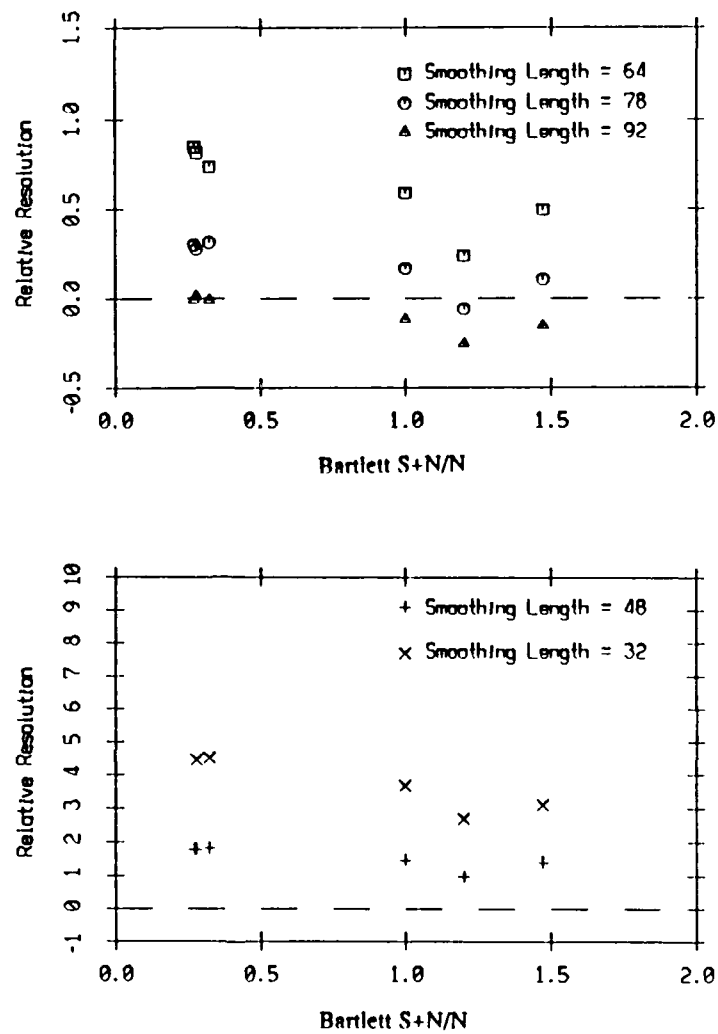
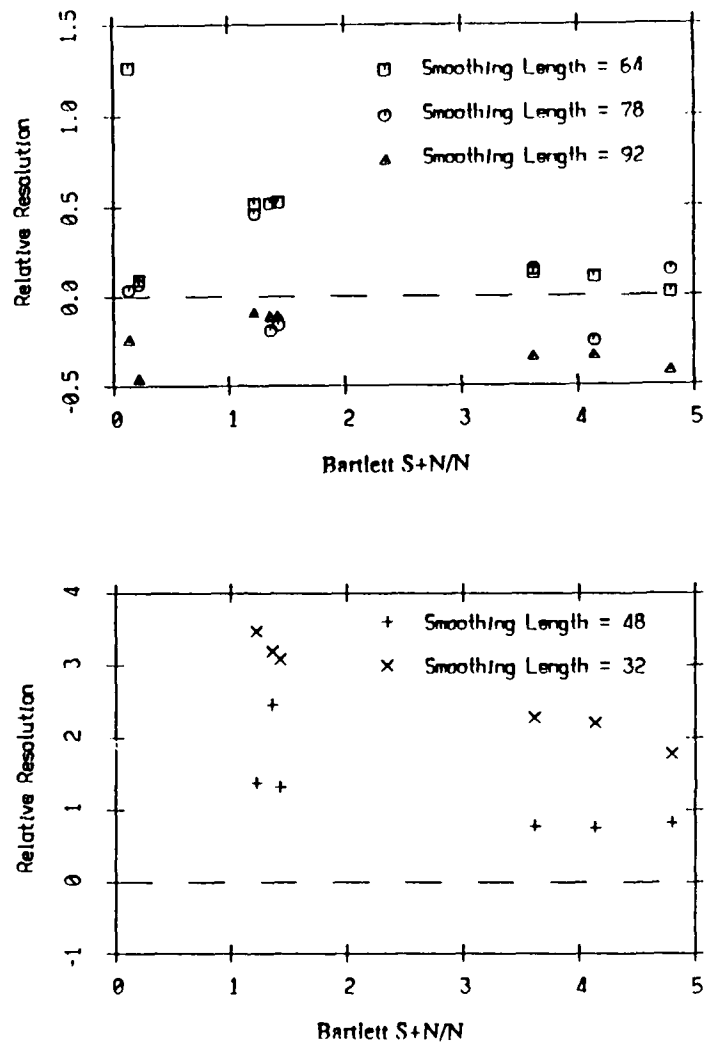


Figure 3.18: Array Gain.



**Figure 3.19:** Resolution performance study for a -18 dB input SNR. Upper panel: full aperture processing, lower panel: subaperture processing.



**Figure 3.20:** Resolution performance study for a -11 dB input SNR. Upper panel: full aperture processing, lower panel: subaperture processing.

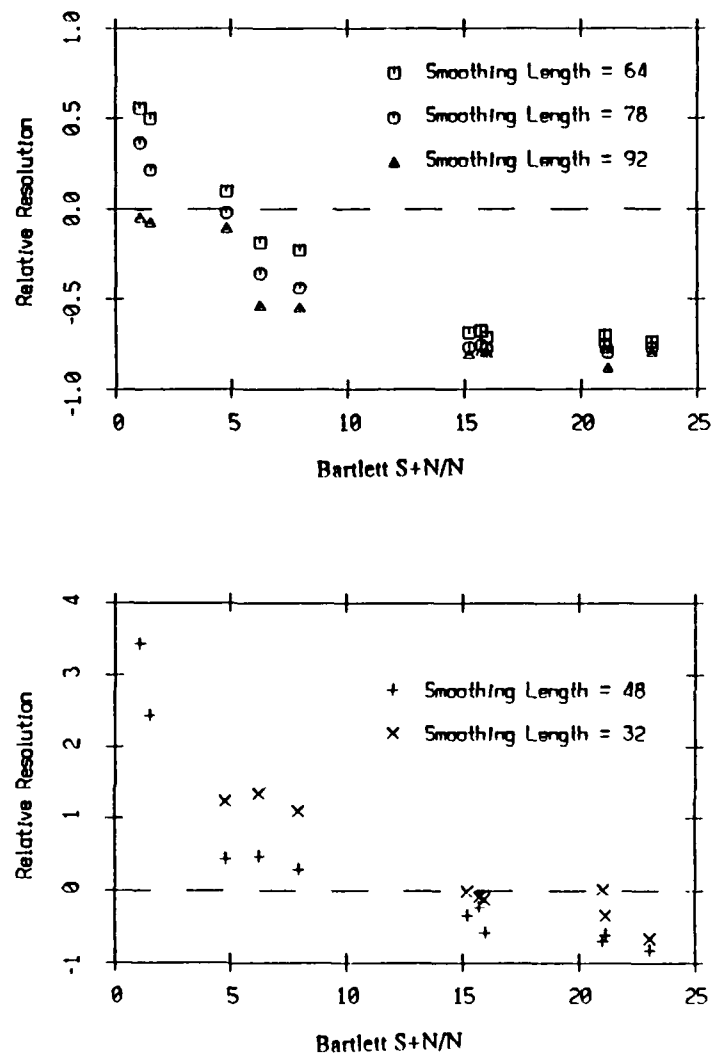


**Figure 3.21:** Resolution performance study for a 9 dB input SNR. Upper panel: full aperture processing, lower panel: subaperture processing.

## **4. Processing Real Data**

### **4.1. Overview**

The various processing techniques proposed in Chapter 3 are used to process real data, collected at sea by the Marine Physical laboratory digital acoustic array, a 900 m long aperture with 120 sensors. First, the data set is presented and the acoustics modelled with ray and normal mode models. The data are processed by the conventional FFT beamformer, the MV processor operating on the full aperture and on two non-overlapping subarrays with various modified spatial smoothing lengths and plane wavefront replica vectors. Qualitative results are presented and analyzed for a high input signal-to-noise ratio case (11.8 dB). A quantitative study completes this work on real data by showing that in both high and low input SNRs (11.8 dB and -9.2 dB), processing gain and resolution are similar to the patterns found in the simulations of Chapter 3. Full aperture MV processing provides more resolution but less processing gain than conventional processing. Subaperture processing does not perform as expected because of the great multipath variability of the particular field processed here. An assumption on the homogeneity of the pressure field has been implicitly made when subaperture processing has been formulated. Experimental results using these techniques indicate that real pressure fields can be highly inhomogeneous.

### **4.2. Presentation of the Data Set**

#### **4.2.1. Introduction**

The data were recorded by the Marine Physical Laboratory (MPL) digital acoustic array during the September 1987 Vertical Line Array (VLA) Experiment in the North-East Pacific [Sotirin; 1989]. The vertical line array, 900 m long and filled with 120 hydrophones with 7.5 m interelement spacing, was deployed for several weeks from the Research Platform FLIP in a three-point moor at 34°58.69' N 125°58.43' W, approximately 400 km southwest of Monterey, California. The VLA was in a transponder net consisting of three near-bottom transponders to enable acoustic navigation of the array [Sotirin; 1989]. This work deals with the 200 Hz CW tone propagation data recorded by the VLA when the source ship, the USNS NARRAGANSETT, kept a fixed station 89 nm from the R/P FLIP on 27 September 1987 or Julian Day 270 [Tran; 1989d]. The top sensor of the VLA was at a nominal depth of 400 m. The acoustic source was deployed at 20 m depth and projected a 200 Hz CW tone with a nominal source level of 184 dB ref 1  $\mu$ Pa at 1 m for 18 minutes from 21:57 GMT. The data were recorded on Tape 918 (which starts at 21:58:27 GMT).

#### **4.2.2. Description of the VLA System**

The characteristics of the MPL digital array are summarized here, more detailed information can be found in [Sotirin; 1988]. The vertical line array has 12 sections, each section contains 10 acoustic transducers and a microprocessor-based processor which samples and telemeters the data to topside on a serial link. The acoustic channels are numbered from bottom to top and a processor samples the 5 transducers immediately below and above. The signal in a given channel is the output of a set of two Benthos Aquadyne AQ-1 hydrophones wired in series. The

resulting acoustic transducer has a sensitivity of  $-197 \text{ dB}/\mu\text{Pa}$ . The transducer output, then, is amplified with a pre-amplification stage with 40 dB gain and filtered between 10 and 220 Hz (with a nominal bandpass gain of 0 dB). A differential line driver transmits the signal to the processor producing a 6 dB gain. In the processor, the analog signal is amplified by a software controlled variable gain (selectable from 0 to 60 dB). The 10 acoustic channels are multiplexed and sampled by a 12 bit bipolar A/D converter with a  $\pm 10 \text{ V}$  reference voltage. The sampling rate is 500 Hz. The two channels immediately adjacent to a processor are low-pass filtered in the processor to allow the 12 kHz acoustic navigation signals to enter into the detection circuitry in the telemetry module.

#### **4.2.3. Environmental Data**

Environmental data were collected during the experiment on the R/P FLIP. Swell heights on Julian Day 270 were visually measured between 5 and 10 feet. A northern wind was blowing with speeds between 20 and 25 knts. A CTD was collected in the vicinity of the R/P FLIP on Julian Day 267, up to a depth of 3885 m. Another CTD, collected at  $37^{\circ}04.19' \text{ N } 134^{\circ}46.75' \text{ W}$  on Julian Day 264, was used to extend the CTD at the R/P FLIP down to the nominal bottom depth, 4667 m. The sound speed profile, based on the CTD, was derived using the UNESCO equations relating conductivity to practical salinity and sound speed to temperature, salinity and pressure [Fofonoff; 1983]. XBT casts were collected at the R/P FLIP before and after the fixed station transmissions on Julian Day 270 at 13:00 GMT (a 400 m XBT) and on Julian Day 271 at 03:00 GMT (a 750 m XBT). These XBT data were used in the state equation of [Mackenzie; 1981] to produce sound speed profiles. This information allows the synthesis of a composite sound speed profile that will be used in the acoustic modeling. A desampled version of the 400 m XBT sound speed profile is used from 0 to 250 m. Then, a desampled version of the 750 m XBT is used down to 700 m where it blends with the CTD sound speed profile. A desampled version of the CTD sound speed profile is then used down to the bottom. The model sound speed profile is plotted in Figure 4.1 for the whole water column and for the top 750 m. The two XBT sound speed profiles are also plotted in dashed lines. A 30 m deep mixed layer was observed at the R/P FLIP, followed by a shallow and weak duct above 100 m, which evolves with time, as shown by the two XBT sound speed profiles taken only 14 hours apart. The environment has a deep sound axis around 550 m.

#### **4.2.4. Data Quality Checks**

Preliminary data quality checks included time series plots, power spectra for selected array channels and conventional FFT beamformer outputs. The power spectra, computed between DC and 250 Hz and plotted in Figure 4.2, are obtained by processing 2 minutes and 11 seconds of data. They are derived from the incoherent addition of 15, 50 % overlapped, 8192-point FFTs (61 mHz bin width). A Kaiser-Bessel window with  $\alpha$  parameter of 2.5, yielding a sidelobe level of  $-57 \text{ dB}$  [Harris; 1978], weights the data prior to each FFT. Power values are calibrated in dB re  $1 \mu\text{Pa}$ , to yield the power for sinusoidal signals. The 90 % confidence interval in these spectra is  $\pm 2/-1.6 \text{ dB}$ . The power spectra illustrate the good quality of the recorded data. The 200 Hz signal appears as a strong line component. The 60 Hz line and its harmonics (120 Hz, 180 Hz and 240 Hz) are the result of power line contamination. Some variability in the noise levels at high frequency is observed, the channels have different self noise characteristics.



The distributions of power in the vertical, plotted in Figure 4.3, correspond to the 200 Hz signal bins 7373 and 7374 (199.951 Hz and 200.134 Hz), and the noise bins 7368 and 7380 (199.646 Hz and 200.378 Hz). They are computed by incoherently averaging thirty 50 % overlapped 8192-point FFTs obtained by processing two data segments of 2 minutes and 11 seconds. As before, the data are weighted by a Kaiser-Bessel window with  $\alpha$  parameter of 2.5 prior to the FFT. The 90 % confidence interval in Figure 4.3 is +1.4/-1.2dB. The maximum signal power varies between 80 and 90 dB re 1  $\mu$ Pa which is consistent with a source level of 184 dB// $\mu$ Pa at 1 m that suffers spherical transmission loss over a range on the order of a water depth (5000 m) and then cylindrical loss over the remaining range. The distribution of noise power across the array shows a somewhat large variability, with peaks 5 to 15 dB above the noise floor between 60 and 65 dB (re 1  $\mu$  Pa). The normalization factor to pass from the sinusoidal component normalization to a noise spectral density normalization is on the order of 10 dB so the noise floor level at 200 Hz is between 70 and 75 dB// $\mu$ Pa/ $\sqrt{\text{Hz}}$ . Such levels are consistent with the common noise levels summarized in [Urick; 1986] for the wind speeds observed at the R/P FLIP (20 to 25 knts). The peaks in the distribution of noise power in the vertical are not the result of a statistical artifact given the large number of averages in the estimator. As mentioned earlier, they indicate channels with high self noise characteristics. The peaks generally correspond to the channels which are physically the closest or the farthest to the processors. The sensors which are closest to the processors are used for the array navigation and are known to be more noisy. The sensors farthest from the processor in each 75 m section suffer the most cross-talk with other telemetry and transmission lines.

The FFT beamformer processes a signal and a noise FFT bins (the signal bin is 7373 and the noise bin is 7368) to obtain preliminary information on the vertical arrival structure. The array is cut for 100 Hz with an interelement spacing of 7.5 m and is therefore spatially aliased at the operating frequency of 200 Hz. The beamforming results are thus plotted between  $\pm 29.5^\circ$  with respect to the horizontal in Figure 4.4. Since the array is numbered from bottom to top, positive angles correspond to downgoing sound or uplooking beams. The noise arrival structure is uniform with angle. The 90 % confidence interval is 2/-1.6 dB except for the spectra referenced at 22:00:38, 22:13:48 and 22:19:12 GMT where it is 2.5/-1.8, 3.3/-2.3 and 1.8/-1.44 dB, respectively. The arrival structure is stationary since the ship was keeping fixed station. Only steep arrivals around  $\pm 15^\circ$  are observed, they correspond to refracted surface-reflected (RSR) paths.

#### **4.2.5. Acoustic Modeling**

##### **Modeling with the GSM**

The CONGRATS ray tracing program of the Generic Sonar Model [Weinberg; 1985] is utilized to model the sound field. The model sound speed profile of Section 4.2.3 is used and the bottom corresponds to the GSM Province Type 3 (c.f. Table 3.1). The ray traces in Figure 4.5 for a 20 m deep source shows that convergence zone propagation takes place with refracted surface-reflected rays. At 165 km from the source, the array receives sound that travelled over 3 convergence zones. Although the nominal source level is 184 dB re 1  $\mu$ Pa at 1 m, the calibrated received levels obtained from the experimental data indicate that the source level is actually closer to 174 dB re 1  $\mu$ Pa at 1 m [Tran; 1989d]. This latter source level will be used in the following. Using a trial and error procedure, a best fit between the experimental data and the modeling is obtained for a source range of 162 km. The

distribution of power computed by GSM, plotted in Figure 4.6, exhibits a strong interference pattern similar to the data. The GSM eigenray angles at the sound axis (550 m) are plotted in Figure 4.7 at 162 km. Once again, a good correspondence with the FFT beamformer output is observed.

### Modeling with ATLAS

The modeling is now performed with the ATLAS normal mode model [Gordon; 1984]. The environmental parameters are the same as with the GSM. The power as a function of range, computed by the ATLAS model, is plotted in Figure 4.8 for a receiver at the same depth as the 200 Hz source (i.e. 20 m). This shallow depth enhances the appearance of the convergence zones. The sound propagates over three convergence zones from the source to the receiving array, assumed at 165 km in the trailing edge of the third convergence zone. The model distribution of power across the array is plotted in Figure 4.9 for a source at 161.4 km from the VLA, and the modeling is excellent as with the GSM. The ATLAS normal mode program produces the complex wavefield across the vertical array which can be beamformed to yield the model vertical arrival structure. The synthetic wavefield for a 165 km range is beamformed as with the experimental data and plotted in Figure 4.10. A very good match of the arrival structures is observed. The pair of arrivals above  $10^\circ$  corresponds to downgoing sound, which is consistent with having the receiving array in the trailing edge of the third convergence zone.

### 4.3. Processing Real Data

The three processing approaches proposed in Chapter 3 are now used on these data collected at sea. Only plane wavefront replica vectors will be used with the Minimum Variance processor operating on the full aperture and on two non-overlapping subapertures. 4096 beams are used between  $-29.5^\circ$  and  $29.5^\circ$ . The first step of the processing is to do a time to frequency domain transformation. The time series of each channel are divided into 50 % overlapped data blocks called time snapshots and Fourier transformed using a Fast Fourier Transform (FFT). The FFT is performed here with a Kaiser-Bessel window with  $\alpha$  parameter of 2.5 (-57 dB sidelobe level). The FFT length determines the input signal-to-noise ratio (SNR), i.e. the signal-to-noise ratio at the input of the beamformer. The preliminary analysis presented in Section 4.2 showed that the input SNR is on the order of 17 dB for a 8192-point FFT. Since coherent processing with a FFT length  $N_{fft}$  yields a processing gain of  $10 \log N_{fft}$ , the FFT length is reduced to 2048 and 16 points so that the input SNRs are on the order of 11 and -10 dB, respectively, and similar to those of Chapter 3. For a 2048-point FFT, the bin width is 244 mHz and the 200 Hz signal lays in bin 1844 (natural frequency of 200.2 Hz). For a 16-point FFT, the bin width is 31.25 Hz and the 200 Hz signal is in bin 15 (center frequency of 218.75 Hz).

The conventional beamformer does an across FFT on the selected frequency bin with a Kaiser-Bessel window with  $\alpha$  parameter of 1.5 (to yield a 35 dB sidelobe level rejection). The dyad vector formed by the signal frequency bin across the array is Fast Fourier Transformed to produce a periodogram. The periodograms are averaged for a number of snapshots to obtain a statistically stable angular spectrum. Here, fifteen averages are performed and the 90 % confidence interval is  $\pm 2/-1.6$  dB.

The Minimum Variance processor requires the estimation of the array covariance matrix. The covariance matrix is computed by averaging over time

snapshots the dyad vectors computed by the time to frequency transform. At least as many dyads as sensors must be averaged to ensure full rank. The MV processor, when it processes the full aperture, requires at least 120 averages in the estimate the array covariance matrix. Here, 126 snapshots are used. When the MV processor beamforms the two 60-sensor subapertures, at least 60 averages are required to estimate the array covariance matrices and 63 snapshots are used here. In all cases the matrix is readily invertible after stabilization with a fraction of noise equal to  $10^{-6}$ . The time duration of the data blocks processed by the three methods is summarized in Table 4.1.

Since the array receives multipath arrivals, spatial smoothing is performed prior to using the MV processor. When the full aperture is processed, three spatial smoothing lengths are used: 92, 78 and 64. When the two 60-sensor subapertures are processed, two spatial smoothing lengths are used: 48 and 32.

The actual count of operations for each processing step of the Minimum Variance processor is examined in [Tran; 1989d]. Given the large number of beams, the most computationally intensive operation is the quadratic form. Neglecting the additional load required to map one of the subaperture angular spectra using Snell's law before incoherently averaging, subaperture processing after spatial smoothing on 48 sensors was found to reduce the computational load by 25 % compared to full aperture MV processing after spatial smoothing on 78 sensors.

Method	Number of FFTS	Data block length for	
		2048-point FFT	16-point FFT
Conventional FFT Beamformer	15	32.8 sec.	0.256 sec.
MV processor on full aperture	126	4 min. 20 sec.	2 sec.
MV processor on two subapertures	63	2 min. 11 sec.	1 sec.

**Table 4.1:** Length of the data blocks

#### **4.4. Qualitative Study of the MV Processing Results: 11 dB Input SNR**

##### **4.4.1. Conventional Processing**

The conventional FFT beamformer output corresponding to the FFT bin 1844 (center frequency of 200.2 Hz), is plotted in Figure 4.11. The plane wave replica vectors are referenced to the sound axis sound speed (1479.1 m/s). There are two main downgoing arrivals in the spectrum. The relative signal level in Figure 4.11 is only on the order of 25 dB and sidelobe leakage is experienced, although a Kaiser-Bessel window with  $\alpha$  parameter of 1.5 with a 35 dB sidelobe rejection is used. The array beampattern is degraded because of phase and gain errors from channel to channel [Sotirin; 1989].

##### **4.4.2. Full Aperture MV Processing**

Full aperture MV processing is performed on bin number 1844 after spatial smoothing on the array covariance matrix. Plane wavefront replica vectors are used and referenced to the sound axis sound speed. When the spatial smoothing length is 64, a large number of averages is performed to decorrelate the multipath arrivals.

One observes that the MV estimate in Figure 4.12 still suffers large signal cancellation. The arrivals between  $10^\circ$  and  $15^\circ$  are close together and difficult to decorrelate. Since plane wavefront replica vectors are used, modified spatial smoothing should produce better results and be used. The MV processor output, obtained after modified spatial smoothing is plotted in Figure 4.13. The power levels are now closer (at most a few dB lower) to the ones produced by the FFT beamformer. Therefore, modified spatial smoothing will be used in the following. When the modified spatial smoothing lengths are respectively 78 and 92, resolution is enhanced at the cost of more signal cancellation as shown in Figure 4.14 and 4.15. The arrival around  $12^\circ$  as well as the one around  $14^\circ$  actually corresponds to a cluster of at least two arrivals very close in angle. A subjective inspection of the full aperture MV processing results suggests that a modified spatial smoothing length of 78 is optimal.

### **4.4.3. Subaperture MV Processing**

#### **4.4.3.1. Experimental Results**

Subaperture MV processing is performed on two non-overlapping 60-sensor subarrays. The upper half of the array extends from 400 to 842.5 m, and is referenced to a harmonic sound speed on the order of 1479.1 m/s (the sound axis sound speed). The lower half of the array extends from 850 m to 1292.5 m and is referenced to a harmonic sound speed of 1481.4 m/s. The two subarrays are processed separately using their respective plane wavefront replica vectors. A modified spatial smoothing length of 48 is used. Since the lower aperture is referenced to a lower sound speed, its angular spectrum is remapped from a reference sound speed of 1481.4 to 1479.1 m/s using Snell's law. The upper subarray angular spectrum and the remapped lower subarray angular spectrum are plotted in Figure 4.16 and 4.17, respectively. The composite angular spectrum is obtained by incoherently averaging the two subaperture spectra and is plotted in Figure 4.18. Three arrivals are resolved between  $10^\circ$  and  $15^\circ$  instead of the two groups of closely separated arrivals detected by the full aperture MV processor. These results are unexpected, the upper and lower subaperture angular spectra are not aligned, even using Snell's law. Subaperture and full aperture processing produce different arrival structures. The upper half of the array receives a high power level arrival around  $14^\circ$  and a lower level one around  $12.7^\circ$ . The lower half receives two arrivals around  $12.3^\circ$  and  $12.7^\circ$ .

Using a modified spatial smoothing length of 32 produces similar results, although the estimate of the angular spectrum is of poor quality as a result of the short smoothing length. Between  $10^\circ$  and  $15^\circ$ , the upper subaperture detects steeper arrivals than the lower aperture as with smoothing on 48 sensors. The resulting composite spectrum exhibits a peak around  $-15^\circ$  and a broad conglomerate of peaks between  $10^\circ$  and  $15^\circ$ . A subjective look at these results suggests that using a spatial smoothing length of 32 sensors is not adequate. The emphasis is now put on the acoustic modeling, in an attempt to understand the behaviour of the subaperture processor.

#### 4.4.3.2. Acoustic Modeling

##### Using GSM

The preliminary acoustic modeling, presented in Section 4.2.5, is complemented by a more detailed study of the eigenrays between  $10^\circ$  and  $15^\circ$  for receiver depths between 200 to 1600 m. As before, the source is at 20 m depth and a 162 km range. All possible eigenrays within the  $[10^\circ, 15^\circ]$  interval are plotted as a function of depth in Figure 4.19. Because of the variations of sound speed with depth, the eigenrays at each receiver depth arrive at different angles which stay within the studied angular interval. Figure 4.19 shows that four dominant arrivals impinge on the array, they correspond to two pairs of closely separated arrivals which are not resolved. At 400 m depth, the first arrival pair has arrival angles equal to  $11.21^\circ$  and  $11.24^\circ$  and power levels equal to 67. dB and 70. dB. The two other arrivals are steeper at  $13.3^\circ$  and  $13.4^\circ$  and have levels of 75. and 76. dB. The steeper pair in the  $[10^\circ, 15^\circ]$  interval dominates the upper half of the array. Over the lower half, both pairs are present.

Ray traces for take-off angles between  $-15^\circ$  and  $15^\circ$  with a  $1^\circ$  increment, plotted in range between 160 and 164 km and in depth between 200 to 1600 m in Figure 4.20, show the same phenomena. An aperture deployed at 162 km receives steeper rays between 400 to 842.5 m than in the 850 to 1292.5 m depth interval. This modeling with the GSM indicates that the variability observed in the experimental arrival structure is real.

##### Modeling with ATLAS

The ATLAS normal mode model is now used to check these preliminary conclusions. The environmental model is the same as in the preliminary acoustic modeling. First, the implementation of the Snell's law remapping operation is investigated. A canonical ATLAS pressure field corresponding to a single mode is beamformed with the two subaperture MV processor. The normalized modal eigenfunctions, gray-level displayed in Figure 4.21 for the whole water column and for mode number 3 to 303, summarizes a great deal of the acoustics. It shows which modes are excited by the 20 m source (modes around mode number 147) and which ones are bottom interacting. The field corresponding to mode number 147 is used to create a simulated array covariance matrix

$$\mathbf{R} = \sigma_s^2 \mathbf{d} \mathbf{d}^H + \sigma_n^2 \mathbf{I} \quad (4.1)$$

where the  $\mathbf{d}$  is the normalized ATLAS pressure field such that  $\mathbf{d}^H \mathbf{d} = 1$ , and  $\mathbf{I}$  is the identity matrix. An input signal-to-noise ratio of 10 dB and a noise level of 50 dB are assumed so that the simulated noise power is  $\sigma_n^2 = 120 \cdot 10^5$  and the simulated signal level is  $\sigma_s^2 = 14.4 \cdot 10^9$ . Since a single mode is excited, the pressure field has a constant phase modulo  $\pi$ . Each mode corresponds to an upgoing ray and a downgoing ray [Boyles; 1984] as observed in Figure 4.22 where are plotted the upper and lower subaperture spectra produced by the MV processor after spatial smoothing on a 48 sensors. Since the lower aperture is referenced to a lower sound speed, its arrival angles are shallower. The Snell's law remapping aligns perfectly the peaks of the upper and lower subaperture spectra, as shown in Figure 4.23 where the two subaperture spectra are overlaid.

The transmission loss from 10 to 1600 m in depth and from 163 to 167 km in range is gray-level displayed between 40 and 65 dB in Figure 4.24. Dark areas correspond to regions of strong attenuation and light colored areas correspond to

region of weak attenuation. The best fit between the ATLAS angular spectrum and the data was found for a range of 165 km. There, the array is in the trailing edge of the third convergence zone. White lineations, which are downgoing with range, correspond to the downgoing ray paths of the GSM. The 400-850 m depth interval is insonified by a sharp and steep light colored line while the 850-1300 m interval is insonified by a broad light-colored area which has smaller slope with range. The ATLAS field plot is in very good agreement with the GSM ray traces: steeper arrivals dominate the upper half of the array. To confirm further the agreement between the modeling and the data, the field produced by the ATLAS model across the array at 165 km is beamformed by the subaperture MV processor (with a modified spatial smoothing length of 48). The simulated field covariance matrix is given by Equation (4.1), using the same noise and signal power. The simulated upper and lower subapertures are processed separately and their angular spectra plotted in Figure 4.25. The composite spectrum is plotted in Figure 4.26. In the  $[10^\circ, 15^\circ]$  interval, the phenomenon observed in the data is also present in the simulated data. Steeper arrivals dominate in the upper half of the array while both shallower and steeper arrivals are present in the lower half of the array.

#### **4.4.4. Conclusions**

Full aperture processing produces a large increase of resolution, as expected in this high signal-to-noise ratio. The cost is a reduction of the processing gain. The arrivals between  $10^\circ$  and  $15^\circ$  are composed of a cluster of arrivals very close together and difficult to decorrelate with spatial smoothing and modified spatial smoothing is the preferred smoothing procedure. Subaperture processing does not behave as expected. An assumption on the homogeneity of the field has been implicitly made when subaperture processing was proposed. A great variability in the multipath structure was found in the experimental data and was successfully modeled using the GSM and the ATLAS models. The angular spectra, computed across the upper and lower halves of the array, can be so different that averaging does not enhance the peaks. The composite subaperture angular spectrum, for a spatial smoothing length of 48, have three peaks instead of two between  $10^\circ$  and  $15^\circ$ . Two distinct arrivals are reported around  $12^\circ$  where an unresolved cluster of arrivals is reported by full aperture processing. On the other hand, subaperture processing resolves a single arrival around  $14^\circ$  while full aperture processing MV processing indicates very closely separated arrivals.

#### **4.5. Quantitative Study**

Performance aspects are now studied as in the simulations presented in Chapter 3, for the 11 and -9 dB input signal-to-noise ratios. Two performance indices are examined: for each arrival, the signal-plus-noise to noise ratio and a relative resolution factor which is the relative difference in 0.1 dB beamwidth between the MV and the Bartlett angular spectra. Here, the goal of the study is to relate the performance measures on real data to the performance patterns outlined through simulations in Chapter 3. Since the signal frequencies, arrival structures, and the array geometries are different in the data and in the simulations, only a partial agreement is expected.

#### 4.5.1. 11 dB Input SNR

The three arrivals around  $-15^\circ$ ,  $12^\circ$  and  $14^\circ$ , modelled with GSM and ATLAS, are considered here. Their peak power is easily measured from the angular spectra presented in the previous Sections. In the case of subaperture MV processing with a modified spatial smoothing length of 48, three arrivals are detected instead of two between  $10^\circ$  and  $15^\circ$ . Based on the acoustic modeling described in Section 4.4.3.2, the pair of peaks around  $12^\circ$  is considered to correspond to the  $12^\circ$  cluster of arrivals, and its higher level peak is selected as the  $12^\circ$  arrival and used to measure signal-plus-noise level and 0.1 dB beamwidth.

The estimation of the output noise power requires a 200 Hz signal free noise data. Signal which is, in frequency, five bins away from the 200 Hz signal bin (number 1844) is used to compute an estimate of the noise covariance matrix. The plane wavefront replica vectors are computed to match the frequency of the noise bin (number 1839) or 198.73 Hz. The beamformed noise field is evenly distributed in angle (spatially white) which is consistent with the mid-frequency considered here, a spatially aliased array and measured wind speed around 25 knts. The signal-plus-noise to noise ratios for the three detected arrivals are compared to the corresponding signal-plus-noise to noise ratios of the FFT beamformer. Their difference is plotted in Figure 4.27 together with the simulations results of [Tran; 1989b], where the input SNR was 10 dB. The simulation data are plotted with the small size symbols which corresponds to a given spatial smoothing length. Original spatial smoothing was performed in the simulations while modified spatial smoothing is used with the experimental data. Although signal frequencies, arrival structure and array geometries are different, good consistency is observed between the experimental and the simulation results. The relative peak levels have the same order as in the simulations. For full aperture MV processing, the drop in signal-plus-noise to noise ratio, compared to conventional beamforming, is at most 6 dB. The experimental results suggest that there is still some signal cancellation for the high level arrivals since the relative peak levels increase when the spatial smoothing length increases. The subaperture MV processing results are in good agreement with the simulation, with slightly worse performance for the low power  $-15^\circ$  arrival. The relative peak levels of the highest power arrivals are consistent with the simulation results, differences may be due to the multipath variability observed in the data.

The relative resolution factor is derived from the 0.1 dB beamwidth measured in the angular spectra using Equation (3.6). It is plotted against the corresponding signal-plus-noise to noise ratios at the output the conventional FFT beamformer in Figure 4.27. The simulation results (corresponding to the 10 dB input SNR) are overlaid with smaller symbols. Once again, one observes a good consistency between the experimental results and the data, with a slightly worse resolution in the experimental results. Still, full aperture MV processing produces an improvement in resolution. Subaperture processing produces mixed results as a result of the multipath variability.

#### 4.5.2. -10 dB Input SNR

Only two arrivals are detected by the various beamformers between  $10^\circ$  and  $15^\circ$  in this lower input SNR case. Since the FFT used here is only 16 point long, the FFT binwidth is 30 Hz wide and the noise power cannot be calculated as in the previous Section. The 200 Hz transmissions lasted for 18 minutes and stopped at 22:17:01 GMT. The data at 22:20:17 GMT, free from the 200 Hz CW tone, are used to estimate the noise angular spectra. The data are Fourier transformed with a 16

point FFT and bin number 15 is beamformed, as with the 200 Hz signal. Although noise data were recorded 18 minutes after the signal data, this estimate of the noise power should have limited bias and be reliable.

The signal-plus-noise to noise ratios are computed and plotted in Figure 4.28 against the conventional FFT beamformer signal-plus-noise to noise ratios. The experimental results are close to the simulation results in the case of full aperture MV processing, with very limited processing gain degradation. The two subaperture MV processing results produces slightly better performance than conventional beamforming on the full aperture for the arrival with relative peak level equal to 4.5 dB. When a subsegment length of 32 is used, only the 12° arrival is resolved.

The relative resolution factor is computed as before and plotted in Figure 4.28. Once again, the experimental results are in good agreement with the simulation results (plotted in small size). Full aperture processing produces an increase in resolution for the 6 dB signal-plus-noise to noise ratio arrival. The two subaperture MV processor operating on the data has resolution characteristics similar to the simulation results. But the highest arrival is slightly better resolved than with the conventional FFT beamformer.

#### **4.6. Array Gain Calculation**

The array gain obtained by the various beamformers can be computed assuming that the detection is based on the highest level arrival. The input and output signal-to-noise ratios (SNR) are calculated from the signal-plus-noise and noise powers at the input and the output of the various processors. The signal-only power levels are estimated by subtracting the noise-only power from the signal-plus-noise levels. When the 2048 point FFT is used, the average noise-only power at 198.73 Hz is 71.979 dB (126 snapshots) at the input of the processors, while the signal-plus-noise power is 84.054 dB (126 snapshots). Then, the input SNR is on the order of 11.8 dB, which is close to the estimated input SNR of 11 dB. When a 16 point FFT is used, the input signal-to-noise ratio has been theoretically reduced by 21 dB and should be on the order of -9.2 dB. Because of the very short FFT, 200 Hz signal free data collected 18 minutes after the signal data are used to estimate noise powers at the input and output of the beamformers. The average noise power at the input of the processors is equal to 93.6 dB (126 snapshots) while the signal-plus-noise average power across the array is 94.87 dB (126 snapshots). Using these raw data, the input signal-to-noise ratio is found equal to -4.7 dB, which is too large compared to its expected value. One should note at this point that the input signal-to-noise ratio is very sensitive to small errors in the noise and signal values. For instance an increase of one dB in noise power produces an input SNR of -12 dB. Since signal and noise data do not correspond to the same absolute time, irreducible errors will be found in the power estimates. The array gain will be estimated in the following with signal-plus-noise levels from data starting at 22:02:49 GMT, noise-only levels from data starting at 22:20:17 GMT and an input signal-to-noise ratio equal to -9.2 dB. Table 4.2 summarizes the array gain values produced by each method.

The values of the array gain for the conventional FFT beamformer should be independent of the input signal-to-noise ratio and the 1 dB error found is due to the erroneous estimation of the noise powers in the lower input SNR case. Given the time elapsed between the signal-plus-noise power estimates and the noise-only power estimates, such an error can be considered acceptable. The array gains produced by full aperture and subaperture MV processing schemes are very close to the conventional FFT beamformer array gain in the case of the -9.2 dB input SNR.



When the input SNR is 11.8 dB, the array gain varies depending on the method used and is lower than the conventional FFT beamformer array gain by at least a few dB. This is expected because of mismatch. For both input SNRs, the experimental results are consistent with the simulations of Chapter 3. The array gains obtained with the beamformers on real or simulated data have the same order and have values below the theoretical array gain value predicted by the  $10 \log M$  rule, or 21 dB.

#### 4.7. Conclusions

The processing schemes proposed in Chapter 3 were used to process real data. Resolution improvements, compared to conventional FFT beamforming, are obtained with the adaptive MV processor. The finer structure in the angular spectra gives some insights on the propagation physics. Using the MV processor on subaperture indicates that the pressure field is highly inhomogeneous and multipath arrivals insonify only part of the 900 m aperture. These complicated propagation characteristics were successfully modelled with both the Generic Sonar Model and the ATLAS normal mode model. After a qualitative study of the various estimates of the angular spectra, resolution and signal-plus-noise to noise ratios are quantified for a high and medium input signal-to-noise ratio (11 dB and -9 dB). The performance indices are consistent with the patterns outlined in the simulations of Chapter 3.

Method	Array Gain (dB)	
	Input SNR 11.8 dB	Input SNR -9.2 dB
Bartlett	14.9	13.9
MV SSL = 92	8.0	13.2
MV SSL = 78	12.8	13.4
MV SSL = 64	12.9	13.1
MV 2 SSL = 48	8.4	12.9
MV 2 SSL = 32	11.2	12.3

**Table 4.2:** Array Gain.

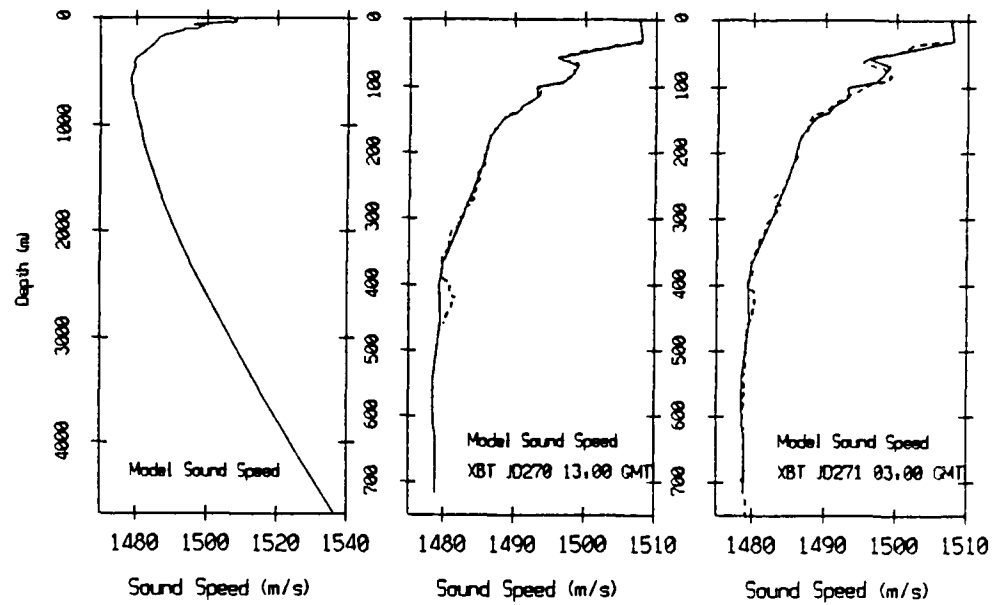


Figure 4.1: Sound speed profile at the R/P FLIP.

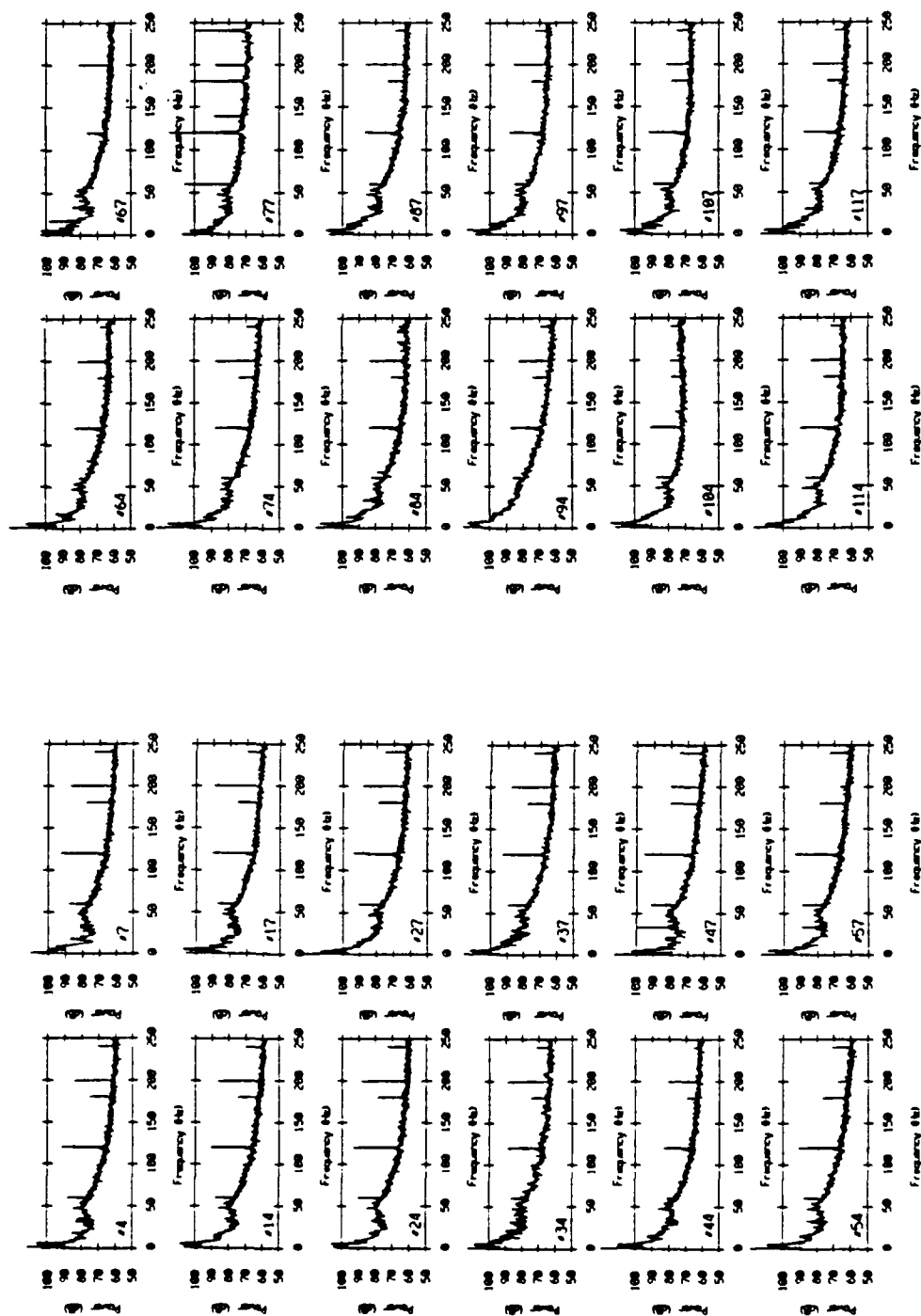


Figure 4.2: Power spectra for selected channels of the VLA.

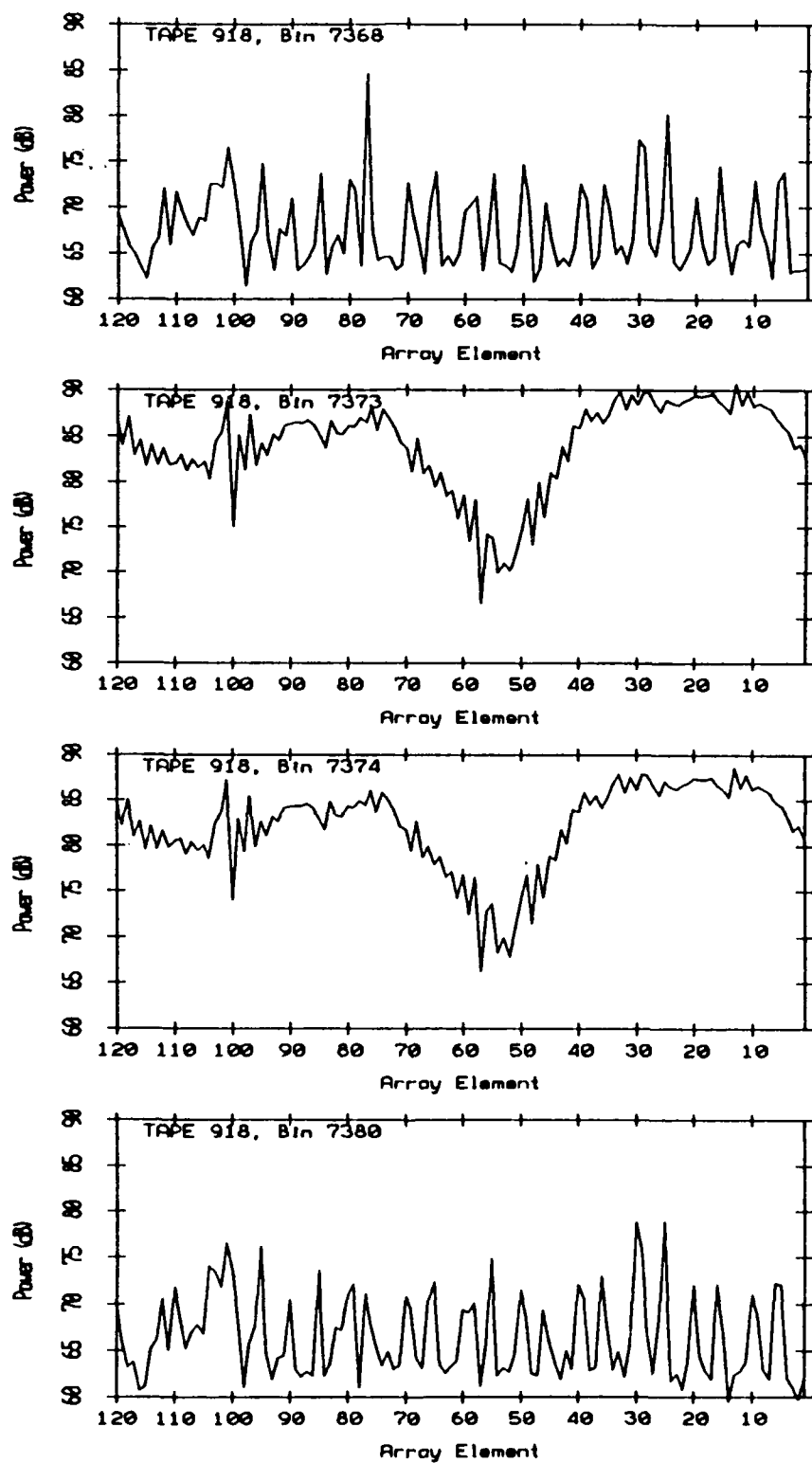
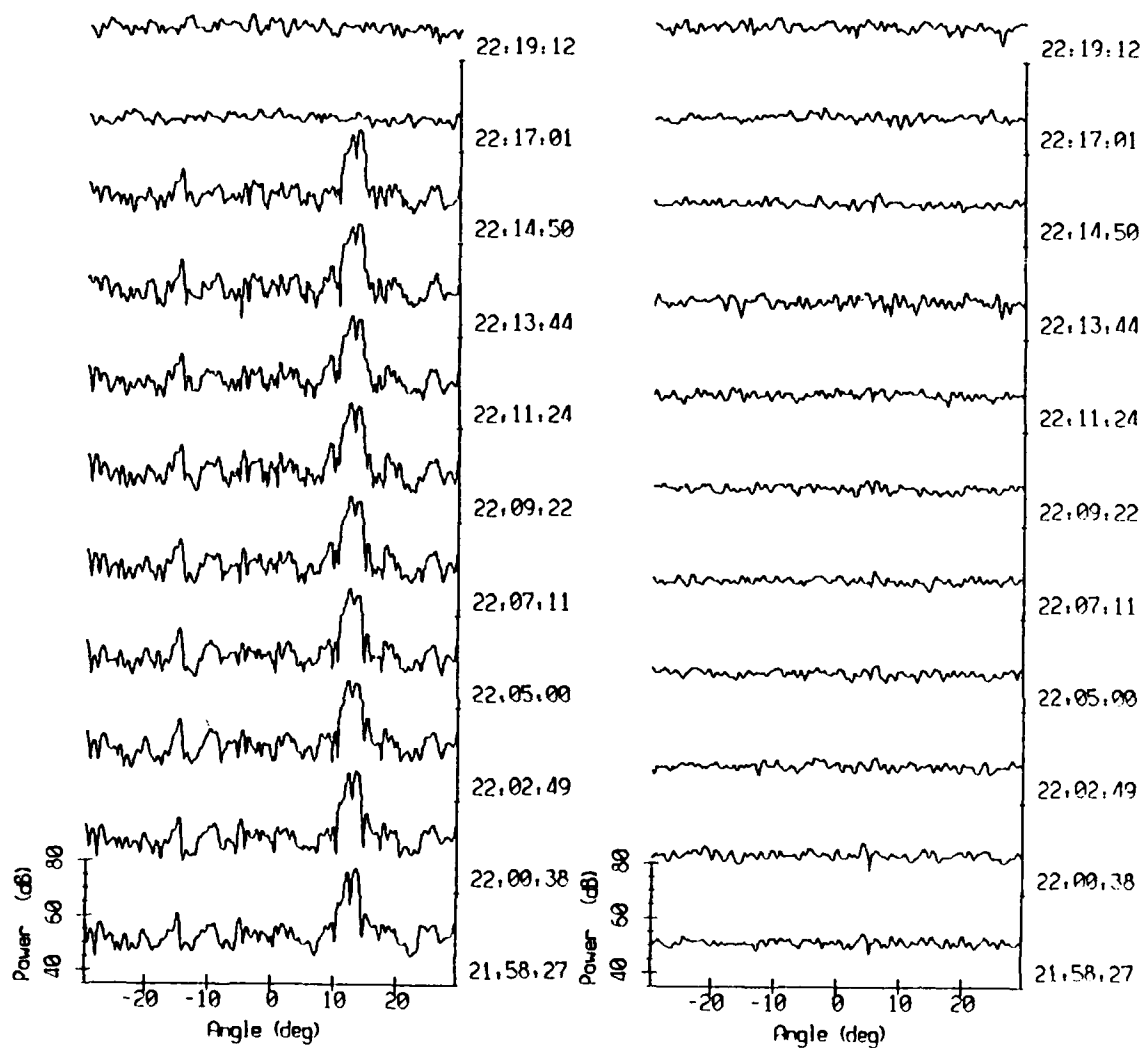


Figure 4.3: Distribution of signal and noise power across the VLA.



**Figure 4.4:** Conventional FFT beamformer output for signal (left) and noise (right) at 200 Hz.

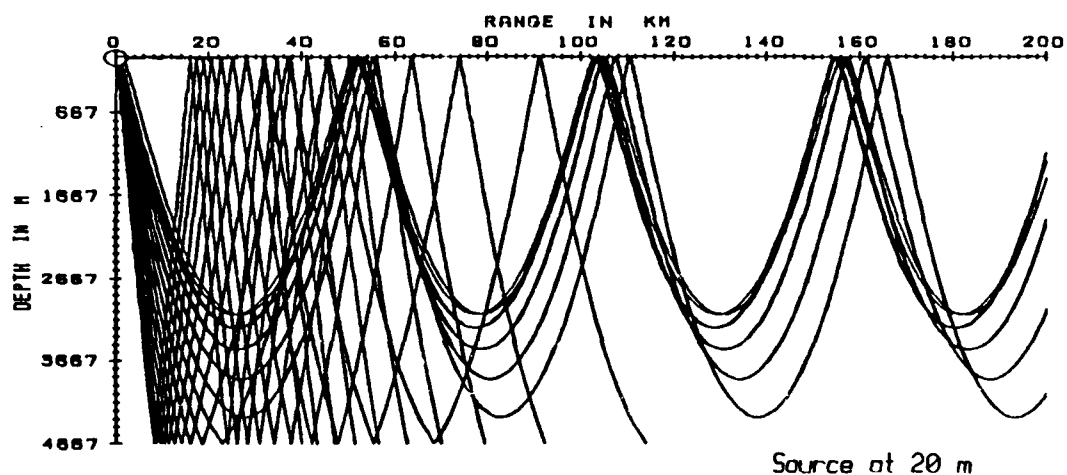


Figure 4.5: GSM ray traces.

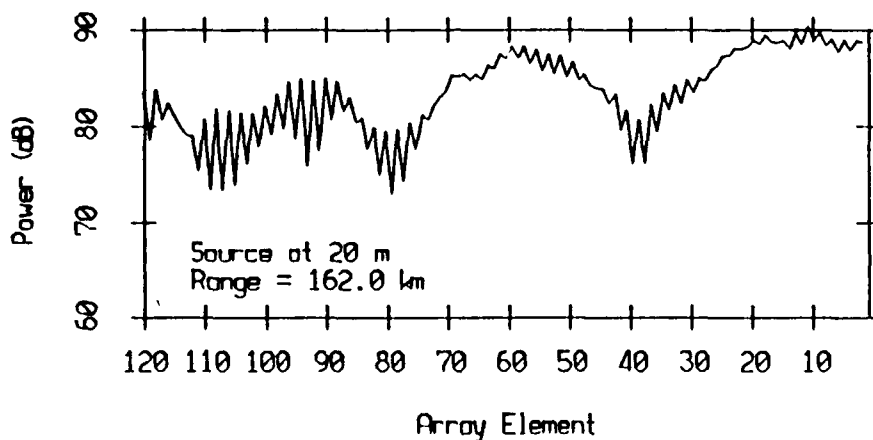


Figure 4.6: GSM power distribution across the VLA.

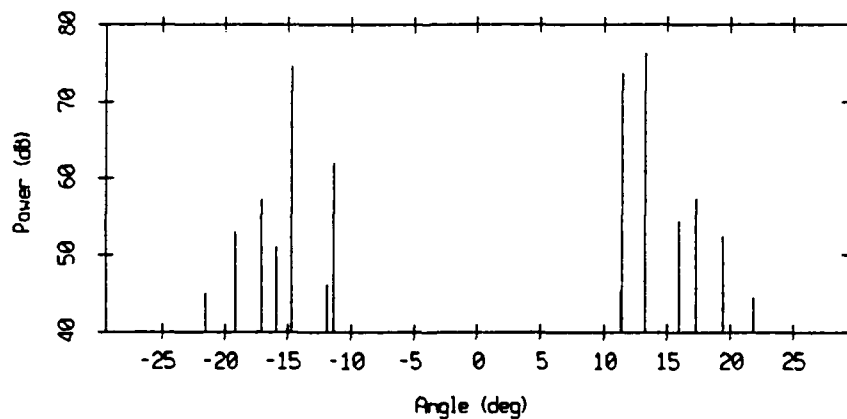


Figure 4.7: GSM eigenrays at 162 km and at the sound axis.

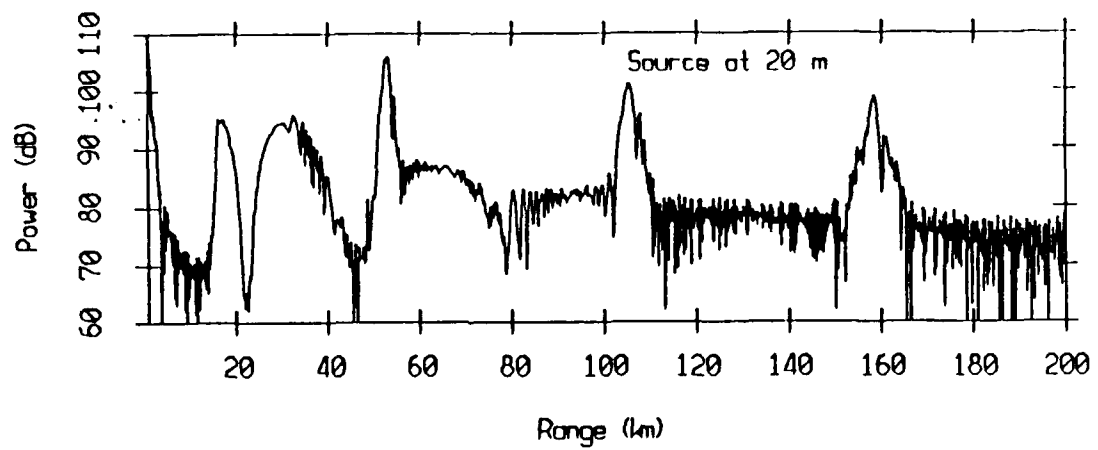


Figure 4.8: ATLAS transmission loss versus range at 20 m depth.

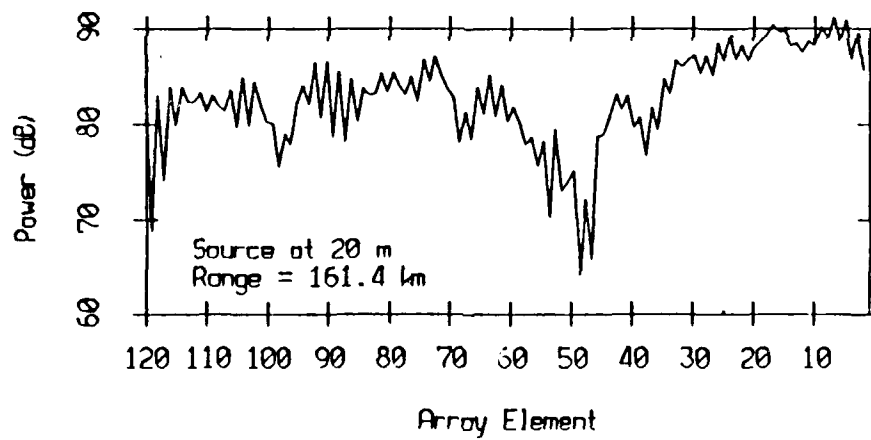
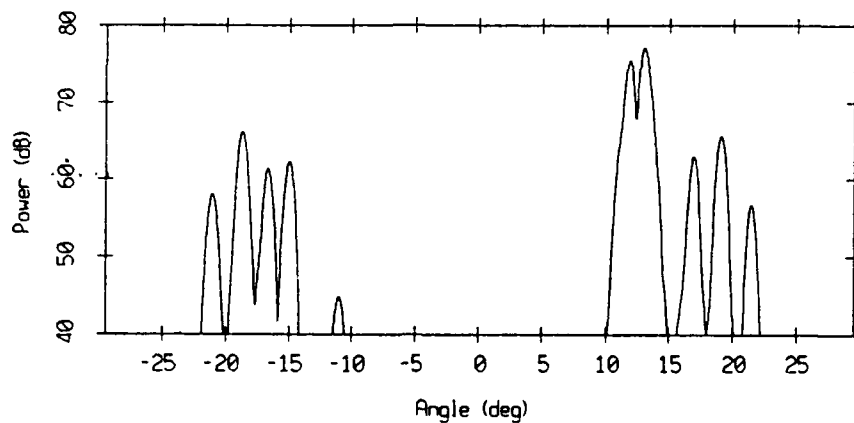
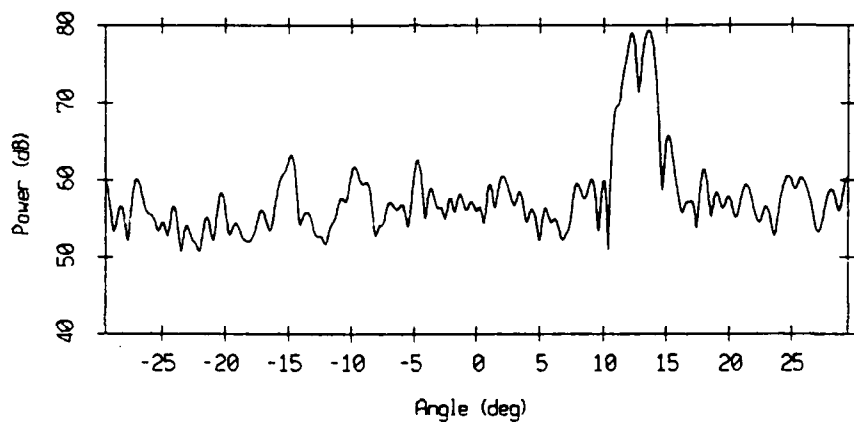


Figure 4.9: ATLAS power distribution across the VLA.



**Figure 4.10:** Conventional FFT beamformer output on the ATLAS field.



**Figure 4.11:** Conventional FFT beamformer output.

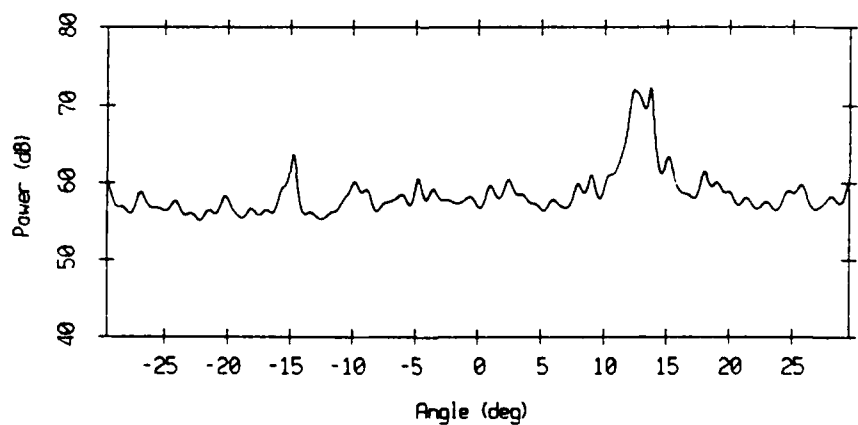


**Figure 4.12:** MV processor output after spatial smoothing on 64 sensors.



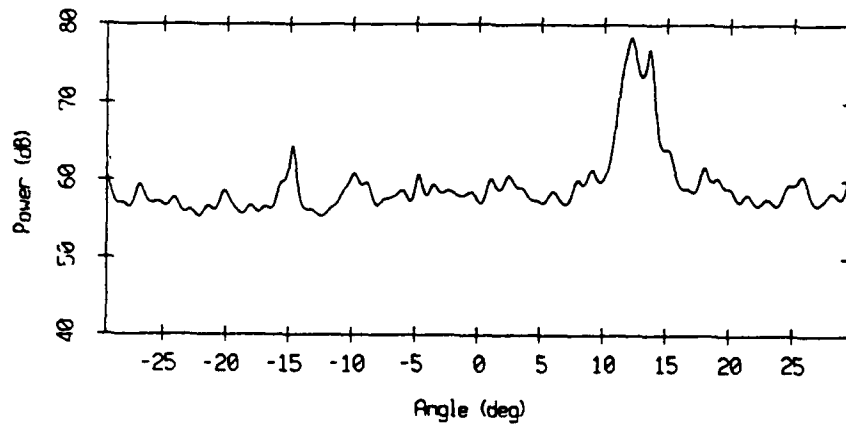


**Figure 4.13:** MV processor output after modified spatial smoothing on 64 sensors.

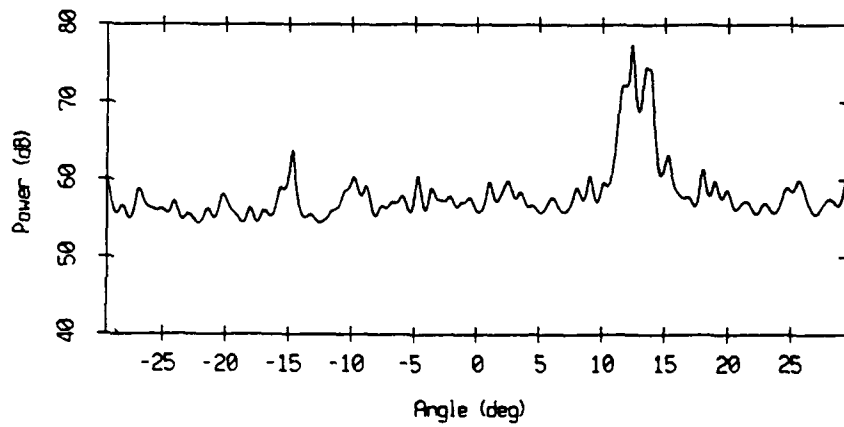


**Figure 4.14:** MV processor output after modified spatial smoothing on 78 sensors.

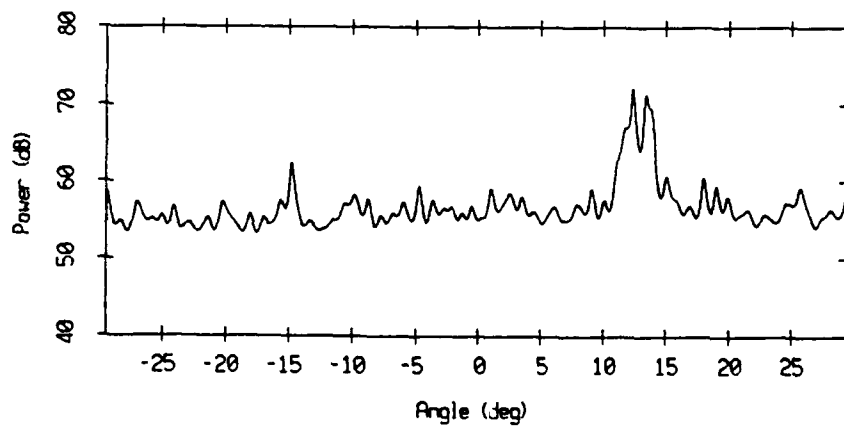


**Figure 4.15:** MV processor output after modified spatial smoothing on 92 sensors.

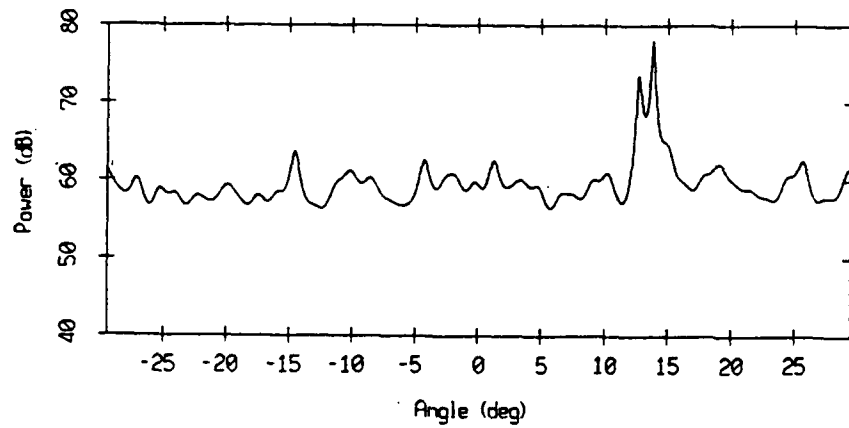


**Figure 4.16:** Upper subaperture MV spectrum (modified smoothing length of 48).

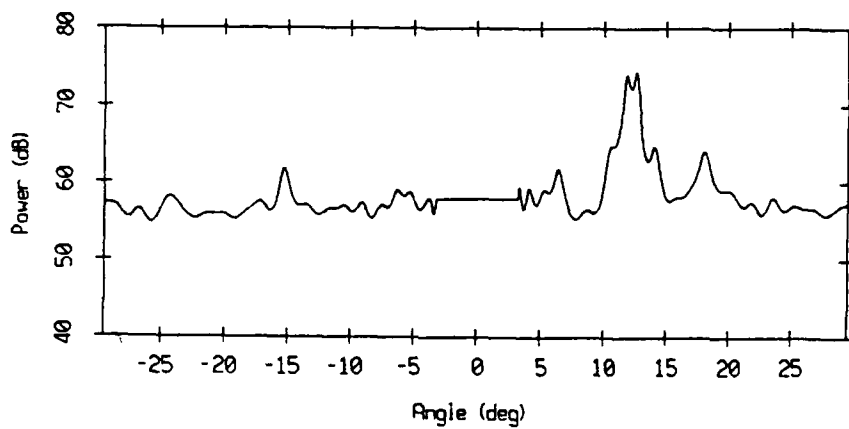


**Figure 4.17:** Lower subaperture MV spectrum (modified smoothing length of 48).

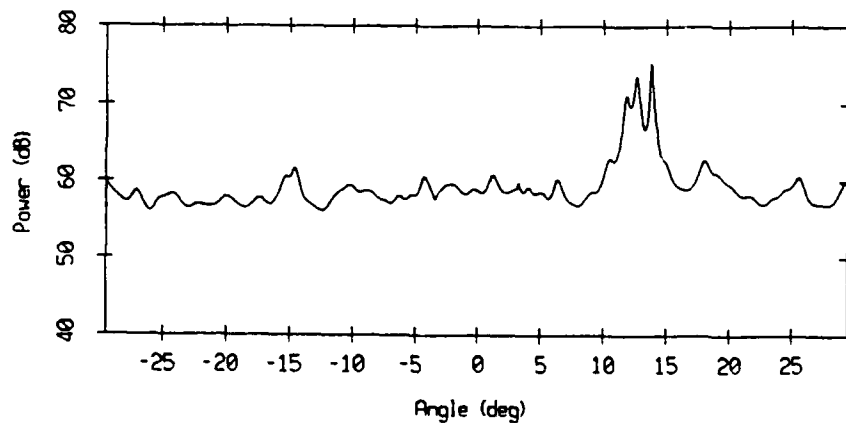


**Figure 4.18:** Average of the two non-overlapping subaperture MV angular spectra.

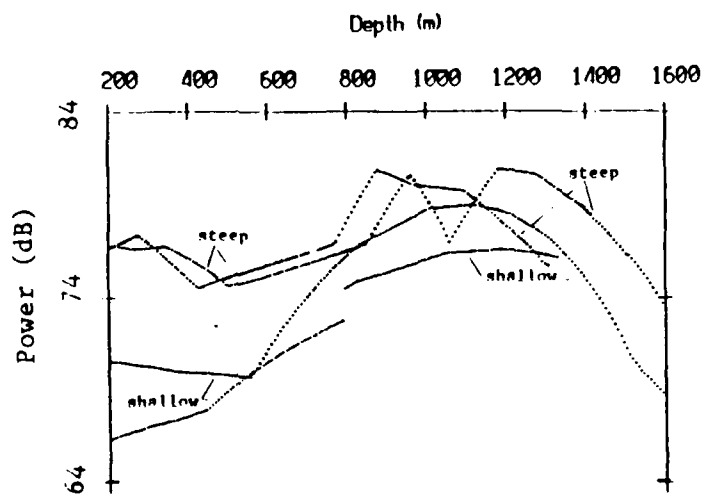


Figure 4.19: GSM eigenrays between  $10^\circ$  and  $15^\circ$ .

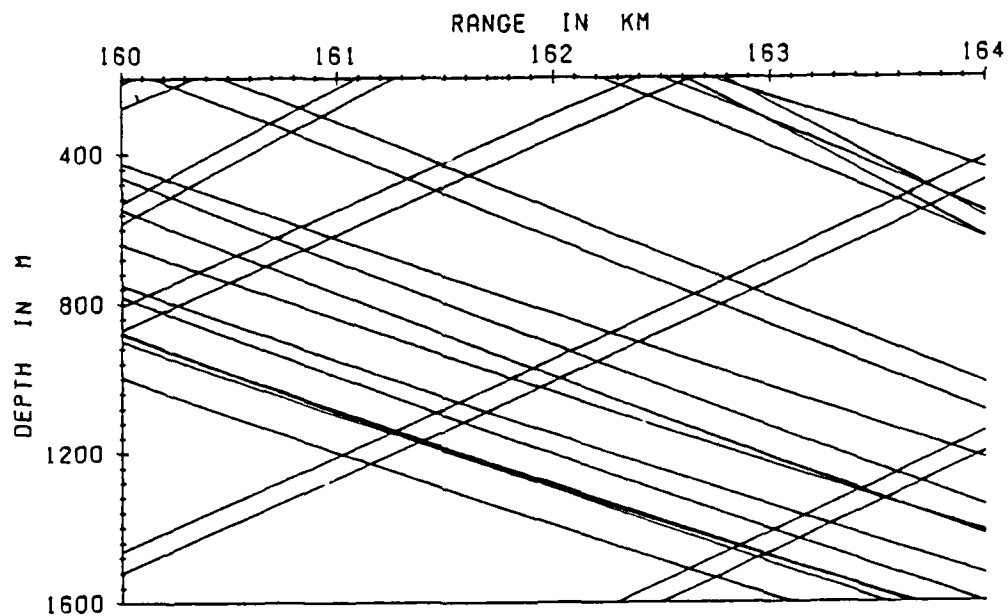


Figure 4.20: GSM ray traces between 160 and 164 km.

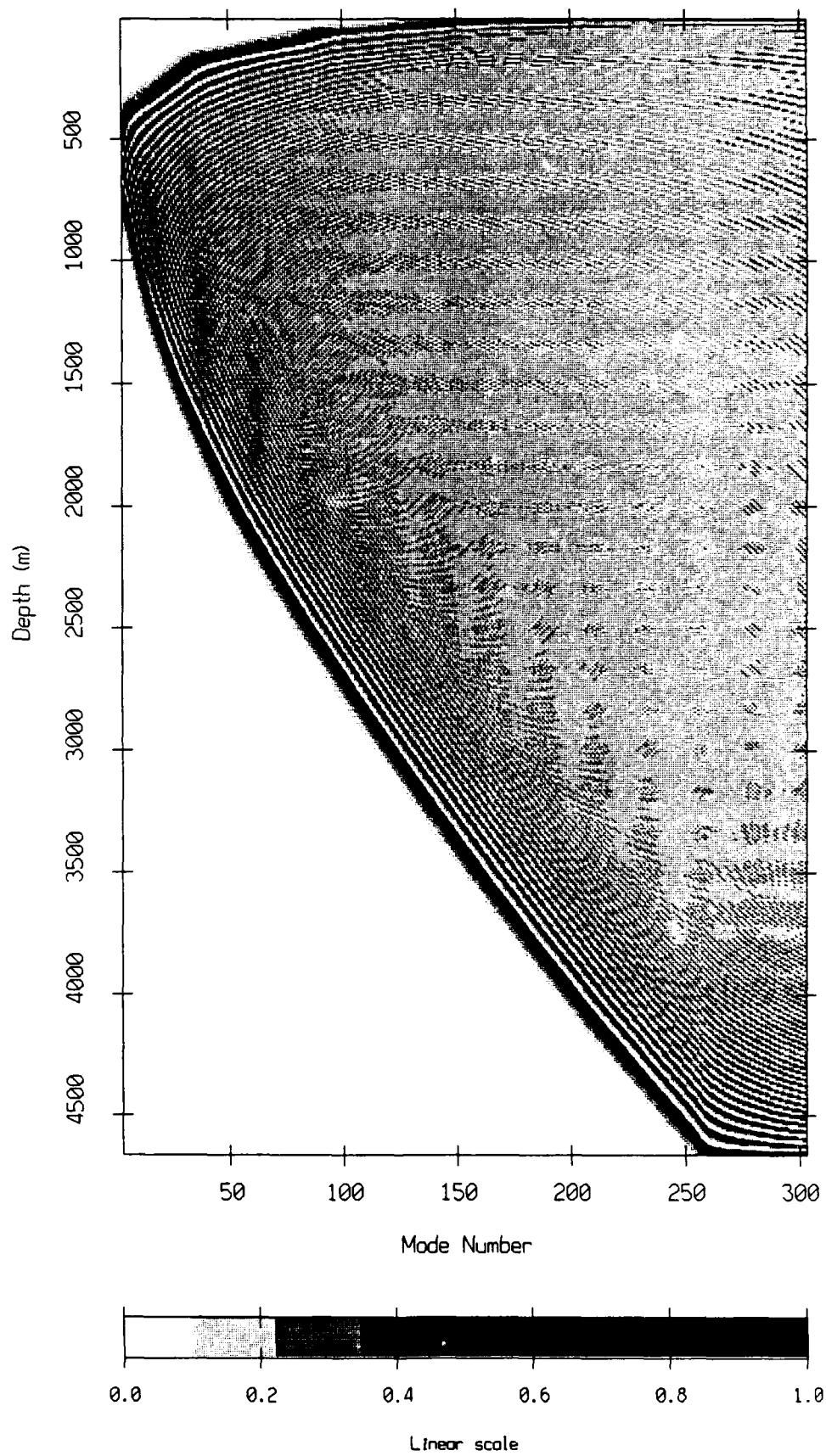
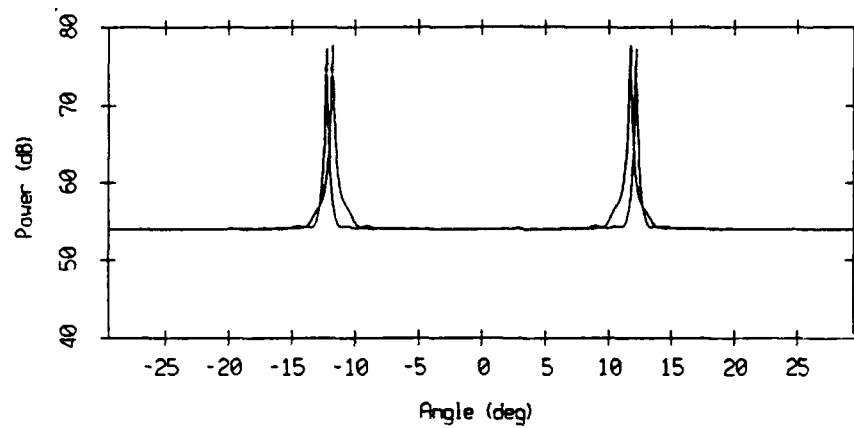
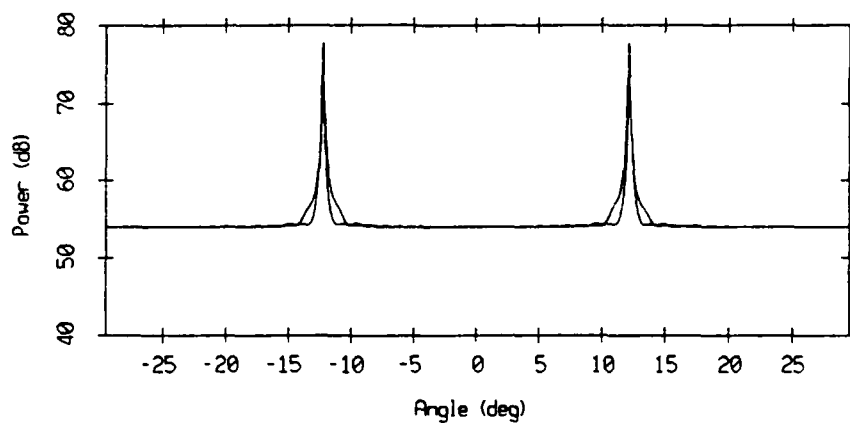


Figure 4.21: ATLAS modal eigenfunctions.



**Figure 4.22:** Upper and lower subaperture MV spectra for a single mode pressure field.



**Figure 4.23:** Upper and lower subaperture MV spectra after the Snell's law remapping.

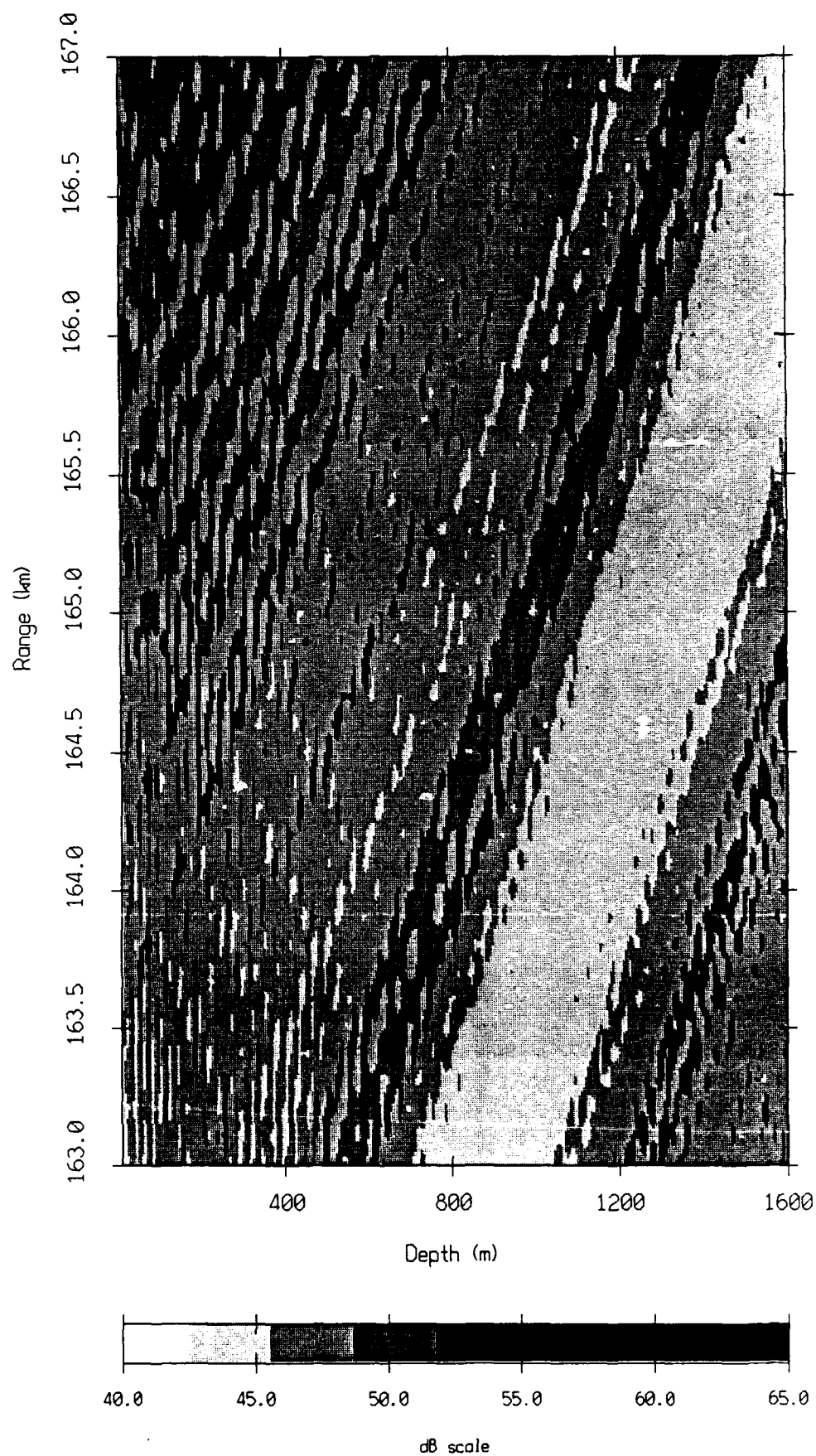
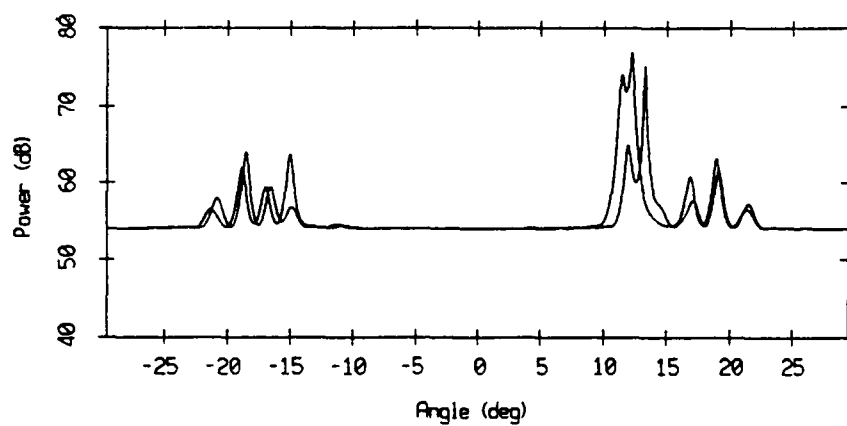
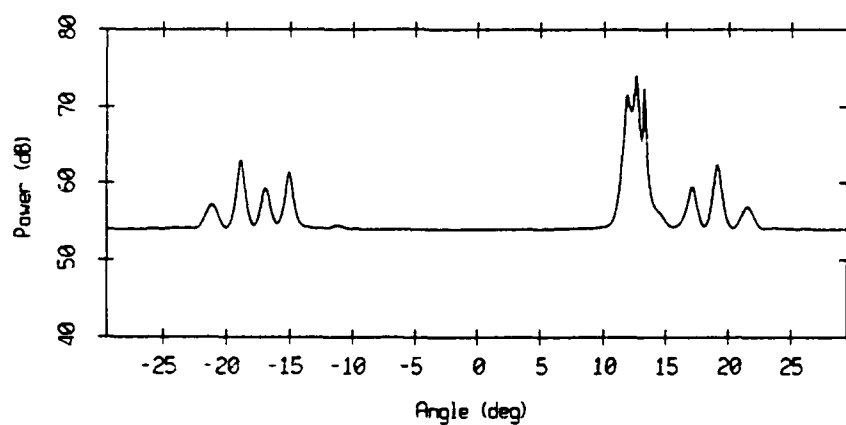


Figure 4.24: ATLAS transmission loss



**Figure 4.25:** Upper and lower subaperture MV spectra of the ATLAS field at 165 km.



**Figure 4.26:** Average of the subaperture MV angular spectra of the ATLAS field.

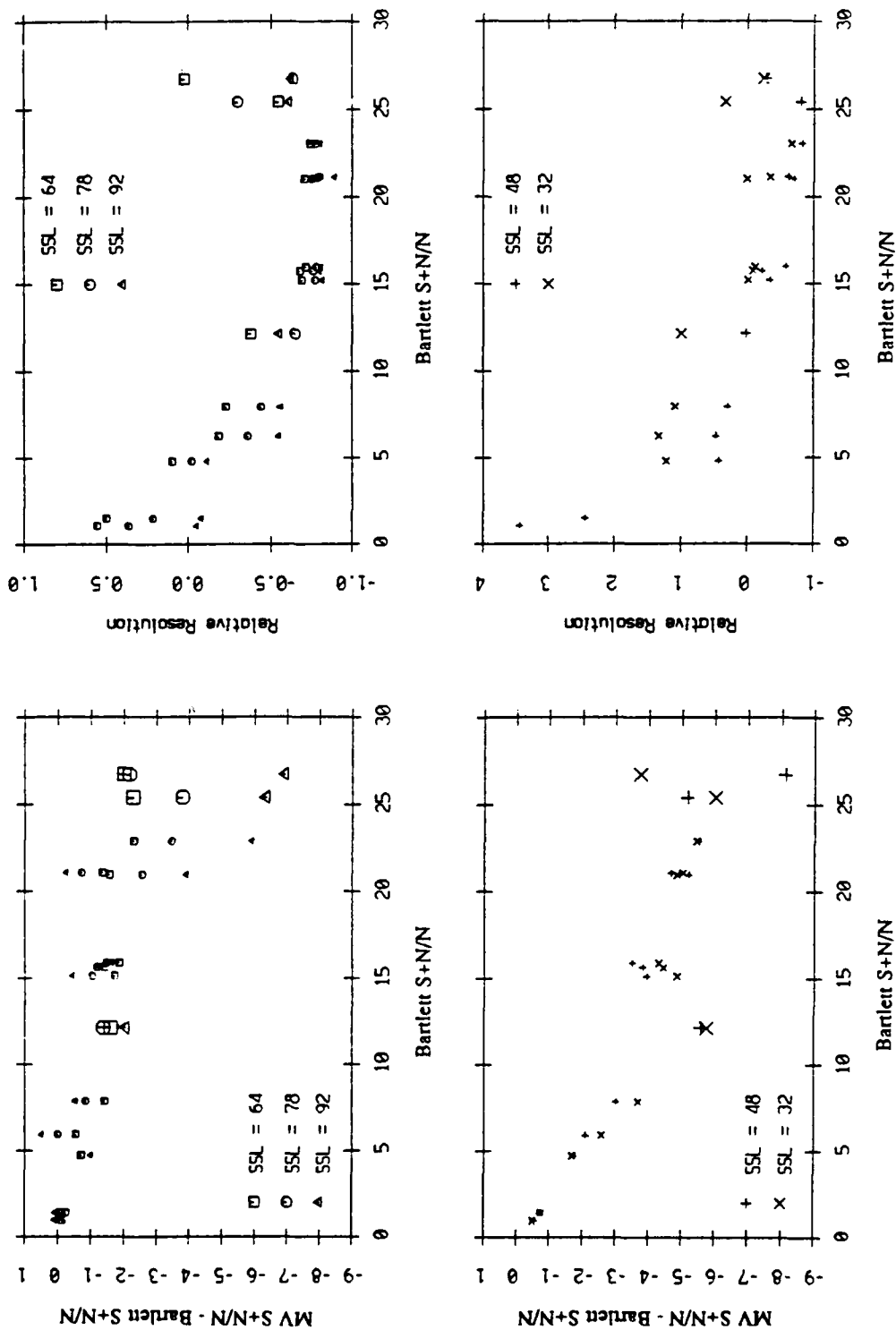


Figure 4.27: Peak level and resolution performance study: 11 dB input SNR.



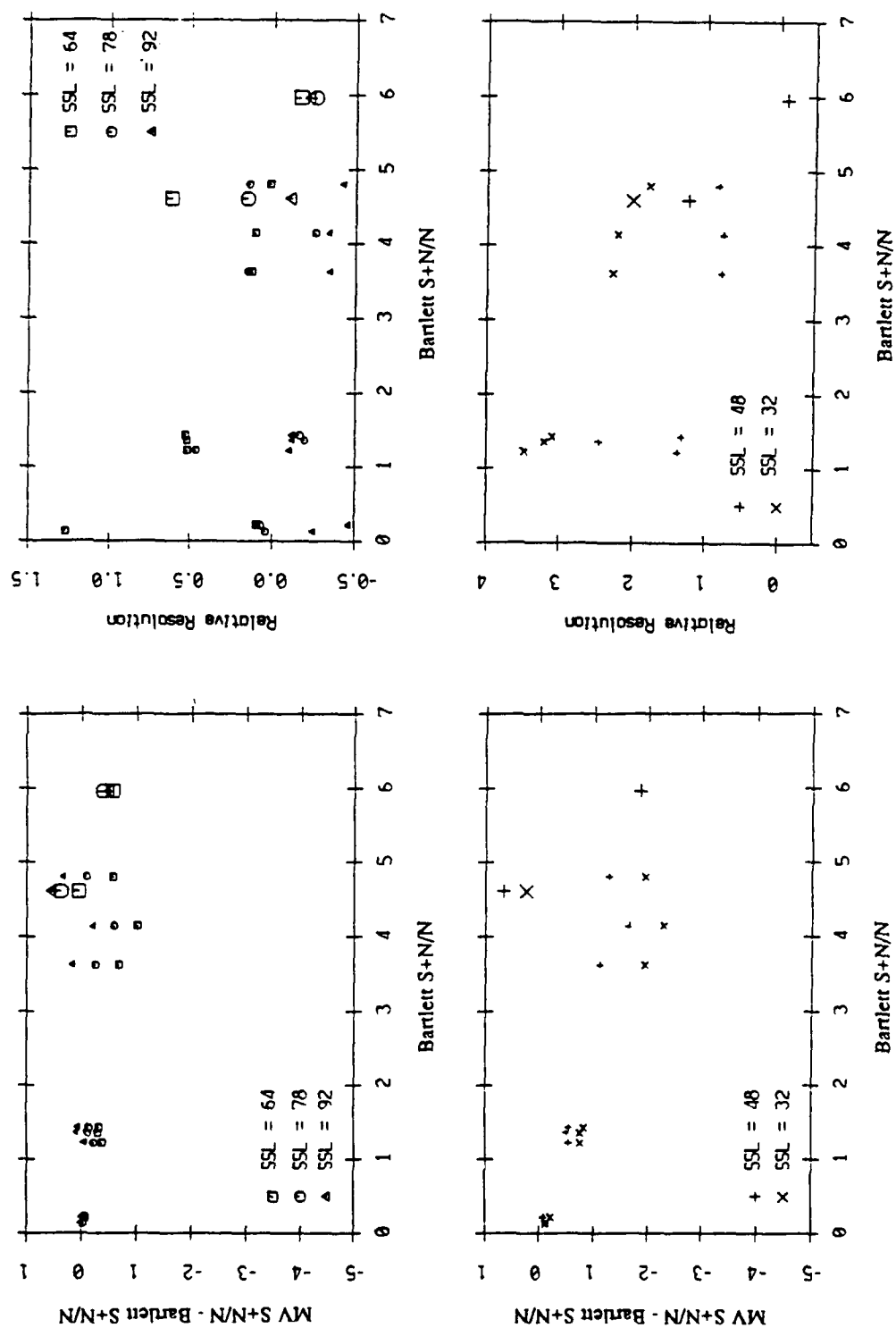


Figure 4.28: Peak level and resolution performance study: -9 dB input SNR.

## 5. Matched Field Processing on the VLA Data

### 5.1. Overview

Based on experimental data collected by the MPL digital array, this chapter demonstrates that matched field processing (MFP) is a viable processing technique at 200 Hz for a 900 m aperture array. The available knowledge of the environment facilitates good acoustic modeling which leads to the detection and localization of a source at 20 m depth and 165 km range. The Minimum Variance processor performs poorly as a result of mismatch due to a 1° array tilt (which is severe at 200 Hz). The array gain estimates obtained with the MFP Bartlett processor at high (11.8 dB) and low (-9.2 dB) input signal-to-noise ratio are higher than the array gain estimates of the conventional FFT beamformer. Based on these experimental results, matched field processing is shown to be a better beamforming approach for signal detection than is conventional processing.

### 5.2. Introduction to Matched Field Processing

A conventional beamformer which processes the data from a vertical line array to estimate an angular spectrum, addresses both the detection and estimation problems. The first function of a beamformer is to detect sound sources such as ships by taking advantage of the spatial processing gain. The detection problem is solved by inspecting the peaks of the angular spectrum. These same peaks also allow the estimation of the directions of arrival. A vertical line array processed in the conventional fashion does not provide a direct answer to the localization problem. To localize the sound sources, one has to compare the experimental vertical angular spectrum with a predicted arrival structure which assumes a known acoustic environment and source position. This "matched filtering" approach, which is implemented indirectly through the use of conventional beamformers, is carried out directly by matched field processing (MFP) [Bucker; 1976, Baggeroer; 1988, Fizell; 1987, Smith; 1989].

Instead of assuming a simple propagation model involving planar and uncorrelated arrivals, matched field processing is based on a more general model which includes wavefront curvature and multipath arrivals. It performs a global search to detect and localize signals by relating a single pressure contribution to each source. The model array covariance matrix for  $k$  uncorrelated sources is

$$\mathbf{R} = \sum_{i=0}^{k-1} \sigma_i^2 \mathbf{d}_i \mathbf{d}_i^H + \mathbf{Q} \quad (5.1)$$

where  $\mathbf{Q}$  is the noise covariance matrix,  $\sigma_i^2$  is the power of the  $i^{\text{th}}$  signal. The normalized vector  $\mathbf{d}_i$  ( $\mathbf{d}_i^H \mathbf{d}_i = 1$ ) does not contain simple plane wave phase relationships indexed on a local angle as in conventional beamforming, but is the total pressure field corresponding to the  $i^{\text{th}}$  source. Matched field processing uses a synthetic pressure field corresponding to a particular source range and depth as a replica vector. Direct localization is obtained from the resulting ambiguity surface peaks, since the search space is indexed on source range and depth. Matched field processing involves complex modeling in order to compute the array manifold but uses the same processing structures as conventional beamforming to measure the correlation between the data and the predicted pressure fields. For this reason, matched field processors are called generalized beamformers.

The MFP signal model, which includes wavefront curvature and multipath arrivals, is closer to reality than the simple signal model of the conventional

beamformers discussed in the previous chapters. This suggests that matched field processing produces a larger array gain and is a better detection tool than the conventional beamformers, in addition to providing direct source localization. The array gain achieved by coherently processing  $M$  sensors is  $10 \log M$  [Pillai; 1989] assuming coherent signals and incoherent noise. Such array gain values cannot be expected by the conventional beamformers since multipath arrivals are searched in angle, as if they were uncorrelated. Matched field processing, which uses the full wavefield and recombines the energy of all the multipaths to calculate the correlation between the measured and the predicted field, theoretically will yield this  $10 \log M$  array gain [Heitmeyer; 1985, Yang; 1989]. The issue of the array gain achieved by conventional beamformers such as the FFT beamformer, was addressed in simulations in Chapter 3 and on real data in Chapter 4. The simulations presented in Chapter 3 involved a 100 Hz CW source deployed at 5 m depth and at 56 km range from a 128 sensor VLA cut for 107 Hz. A realistic ocean waveguide was considered with a sound speed profile characteristic of the North-East Pacific. The matched field signal model was used to produce simulated data using a normal mode model. The synthetic wavefield, then, was beamformed with the conventional beamformers (the FFT beamformer and the Minimum Variance beamformer). The array gain was computed and found to at most 14 dB, i.e. 7 dB below the expected array gain of  $10 \log M$  or 21 dB for  $M = 128$ . Array gain estimates on real data in Chapter 4 were found to be at most 14 to 15 dB on 200 Hz CW signals recorded by the MPL digital acoustic array, a 120 sensor vertical line array, also with a 21 dB expected array gain.

The ability to detect and localize with the matched field processing techniques is highly dependent on the knowledge of the environment and the subsequent acoustic modeling involved in the computation of the array manifold [Porter; 1987, Del Bazo; 1988, Feuillade; 1989, Tolstoy; 1989, Baxley; 1989]. Matched field processing requires a detailed knowledge of the sound speed structure of the waveguide, its eventual range dependence as well as other environmental parameters. An erroneous modeling produces mismatch which can severely degrade the matched field processing performances. In comparison, conventional beamformers require no or little knowledge of the environment. The curved wavefront beamformers, proposed in Chapter 2 and 3, only requires knowledge of the sound speed across the array. An issue with matched field processing is to determine whether or not a sufficient knowledge of the environment is available before attempting to process real data.

Good environmental information was collected during the September 1987 VLA Experiment and allowed an accurate acoustic modeling of the data of Chapter 4. Matched field processing is attempted here on the same data set. Localization and processing gain performances are examined.

### **5.3. Matched Field Processing on Real Data**

#### **5.3.1. Description of the Processing**

Matched field processing techniques blend signal processing and acoustic modeling as shown in Figure 5.1. These two areas were investigated in Chapter 4. After data quality checks, the array covariance matrix was generated and processed by the beamformers to produce angular spectra. Acoustic modeling with the ATLAS normal mode model has been performed using the available environmental data, compared to the experimental results and is now used to create the MFP array manifold. The matched field techniques, then, process the data covariance matrix

with the set of replica vectors generated by the normal mode model, using the conventional or Bartlett processor and the MV processor.

The same data segments, as in the case of the conventional beamformers of Chapter 4, are used to estimate the data covariance matrix. The covariance matrix is obtained by averaging 126 snapshots computed with 2048 point FFTs to get a 11.8 dB input SNR and or a 16 point FFT to obtain a -9.2 dB input SNR. Both signal-plus-noise and noise-only data are processed by the MFP. When a 2048 point FFT is used, the signal-plus-noise and noise-only data correspond to the same absolute time but have slightly different frequencies. The signal FFT bin is # 1844 or 200.2 Hz, and the noise FFT bin is five FFT bins away (# 1839) or 198.73 Hz. In the case of the 16 point FFT, the bin width is on the order of 30 Hz and one uses noise-only data recorded 18 minutes after the transmissions, at the same center frequency (Section 4.6). The array covariance matrix, for both input SNR, can be easily inverted with a small stabilization factor as in Chapter 4, but will be stabilized here with a fraction of noise  $\gamma$  equal to 0.001, 0.01 and 0.1 to enhance the robustness of the MV processor (Section 1.6.3.2).

The replica vectors are computed for a source in a spatial window extending in range from 152.5 to 177.5 km, and in depth from 5 and 600 m. The sampling rates in range and in depth are respectively 250 m and 5 m. The sound speed profile is derived from the CTD and XBT data recorded at the R/P FLIP at the time of the experiment. The bottom is characterized by a GSM Bottom Province Type 3, its influence is weak because the propagation experiment takes place in deep water. The ambiguity surfaces computed by the Bartlett and MV processors are plotted in logarithmic gray levels. In each case, the gray levels span the full dynamic range of the surface which is normalized to its highest peak. The peak value is recorded and normalized to yield power in dB re  $\mu\text{Pa}$ .

### 5.3.2. 11.8 dB Input SNR Case

The signal with 11.8 dB input SNR is processed by the matched field processor and the results presented in Figure 5.2 and 5.3. The source at 20 m is detected at the expected source location as shown in Table 5.1.

Processor	Highest Peak Power dB	Highest Peak Location	
		Range (km)	Depth (m)
Bartlett	79.0	163.50	25
MV ( $\gamma = 0.001$ )	49.6	164.25	20
MV ( $\gamma = 0.01$ )	54.4	164.25	20
MV ( $\gamma = 0.1$ )	60.0	164.25	20

**Table 5.1:** Matched field processing (11.8 dB input SNR).

The ambiguity surfaces are granular with a large number of sidelobes. One recognizes in the Bartlett ambiguity surface the usual pattern which is similar to a field plot at a convergence zone. Using the MV reduces these sidelobes, which have less and less structure as the fraction of white noise  $\gamma$  increases. The dynamic range in the ambiguity surfaces of the MV processor is small compared to the one of the Bartlett processor. The MV processor suffers large loss due to mismatch in this high signal-to-noise ratio case. As the amount of stabilization in the covariance matrix increases, the robustness is increased and the highest peak absolute level

increases.

Matched field processing on the noise-only data are presented in Figures 5.4 and 5.5. The ambiguity surfaces indicate darker areas below 300 m, deep in the water column. The highest peak appears at large depths at 440 m or at 550 m. The MV processor also indicates a surface source at the source range. Since a Kaiser-Bessel window with 57 dB sidelobe rejection level is used in the time to frequency transform, this is not the results of 200 Hz signal leakage. This peak in the ambiguity surface probably correspond to the radiated noise of the support ship from which the source was deployed. It could also be a sidelobe from a distant (unknown) source. The noise data are processed with 198.7 Hz replica vectors, although using the 200 Hz replica vectors of the signal-plus-noise case would produce negligible differences in the ambiguity surface structure and peak levels. On the other hand, simulations involving a source in a spatially white noise with 10 dB input SNR show that the mismatch due to a frequency offset of 2 Hz has a major impact on the MV processor with mismatch losses on the order of tens of dB.

### 5.3.3. -9.2 dB Input SNR Case

The results for the low input SNR case are presented in Figures 5.6 and 5.7 for the signal data and in Figures 5.8 and 5.9 for the noise-only data. The source is detected at its correct location by the Bartlett processor. The conventional processor ambiguity surface for signal data is similar to the high input SNR case. Some structure appears in the surface below a depth of 300 m and corresponds to the noise field. Below 300 m, a great similarity is observed between the signal-plus-noise and noise-only ambiguity surfaces. The highest peak in the ambiguity surface produced by the Minimum Variance processor does not corresponds to the expected source (20 m depth and 165.5 km range). Nevertheless, a peak can be found next to the expected source position at a depth of 20 m and a range of 166.25 km, with a power level close to the highest power level. This signal becomes better defined as the amount of stabilization in the array covariance matrix is increased and will be used in the performance study. Table 5.2 summarizes the signal information with the highest peak power level and location as well as the probable source strength and location, based on the ambiguity surfaces. Matched field processing on the noise-only data which were recorded 18 minutes after the signal data produces ambiguity surfaces which have a similar noise structure as in the high signal-to-noise ratio. The ambiguity surfaces have darker areas below 300 m in the deep sound channel. Since the input SNR is lower by 20 dB compared to the previous section, no signal is detected at the support ship range.

Processor	Highest Peak			Probable Target		
	Level (dB)	Range (km)	Depth (m)	Level (dB)	Range (km)	Depth (m)
Bartlett	80.97	166.5	20	80.97	166.5	20
MV ( $\gamma = 0.001$ )	62.85	156.25	220	61.54	166.25	20
MV ( $\gamma = 0.01$ )	65.56	161.75	190	65.33	166.25	20
MV ( $\gamma = 0.1$ )	70.64	165.25	95	70.61	166.25	20

**Table 5.2:** Matched field processing (-9.2 dB input SNR).

#### **5.4. Matched Field Processing Simulations**

After these qualitative experimental results, which show excellent localization performance, simulations are now presented in an effort to understand the experimental ambiguity surfaces.

##### **5.4.1. No Mismatch Simulations**

A perfect situation is now assumed where there is no noise and no mismatch (i.e. the replica vectors computed by the ATLAS model constitute the "truth"). A 200 Hz source is simulated at a range of 165 km and a depth of 20 m. The ambiguity surfaces for the Bartlett processor and the three different implementations of the MV processor are computed and plotted in Figures 5.10 and 5.11. The source is correctly localized. Since there is no mismatch and no noise, the dynamic range of the ambiguity surfaces is much larger than in the case of the real data. The Bartlett processor produces, in all these simulation cases, a large number of sidelobes. It exhibits the hat shape, also observed in the real data ambiguity surfaces. The MV processor has a great sensitivity to mismatch in this noise-free simulations and produces a single peak in the range-depth cell of the simulated source. These simulation results indicate that there is some mismatch between the replica vectors and the data.

##### **5.4.2. Analysis of Mismatch**

There are several potential causes for the large mismatch observed in the matched field processing results. Although sound speed information at the R/P FLIP is very good, a range independent medium is assumed which may not be accurate for ranges on the order of 165 km. There is no available range dependent information to improve the processing. As mentioned earlier, the bottom should have only a weak influence in the processing results since this is a deep water environment. Another cause for mismatch is the position errors of the array sensors. The VLA array was deployed in a three transponder network and one channel per array section was navigated during the experiment [Sotirin; 1989]. Unfortunately navigation data are not available during the data segment processed here (Tape 918) because of temporary hardware problems. Navigation information is available for Tape 915, 40 minutes earlier and is summarized in Figure 5.12. The array shapes are plotted in the North-South and East-West vertical planes. These typical navigation data indicate that the array behaves, to the first order, like a pendulum and the largest horizontal displacement across the array aperture is bounded by 15 m. Such displacement, corresponding to a  $1^\circ$  tilt, represents two wavelengths at 200 Hz and is likely to have a major impact on the matched field processing results. This source of mismatch is now investigated.

##### **5.4.3. Tilted Array Simulation**

A tilted line array is simulated with horizontal displacement of 15 m. The source is assumed at 165 km from the array top element and at a depth of 20 m. This tilted array matched field processing simulation is summarized in Figure 5.13. The replica vectors, which were used earlier, assume a straight line vertical array. The impact of mismatch due to array tilt is investigated in a noise free case, and the ambiguity surfaces are plotted in Figure 5.14 and 5.15. The matched field

processing results also are summarized in Table 5.3. Array tilt results in enough mismatch to significantly reduce the maximum peak power and shift the position of the peak in range and depth. The mismatch is sufficient to reduce in a dramatic way the signal-to-background-noise ratio. The estimated position of the source is not the true one and is offset by 4 km in range. These simulated results suggest that array tilt can be held responsible for the large mismatch observed in the real data ambiguity surfaces.

	Bartlett	Processor		
		MV $\gamma = 10^{-3}$	MV $\gamma = 10^{-2}$	MV $\gamma = 10^{-1}$
Range of Max.	160.75 km	161 km	161 km	161 km
Surface Max.	-8.7 dB	-49.8 dB	-39.8 dB	-29.8 dB

**Table 5.3:** Tilted array matched field processing simulation

### 5.5. Matched Field Performance Study

In addition to the localization performance criteria, one is interested in performance measures that characterize matched field processing. Several performance criteria have been proposed in the literature, such as the relative peak to mean background level given by  $\frac{P - \mu}{\mu}$  where  $P$  is the peak level and  $\mu$  the mean level [Del Bazo; 1989], or the peak level above the mean level relative to the standard deviation of the ambiguity surface  $\sigma$ ,  $\frac{P - \mu}{\sigma}$  [Feuillade; 1989], or the peak relative to the highest sidelobe level. None of these common performance criteria is satisfying because they do not fully characterize the ambiguity surface and, given the complexity of the experimental ambiguity surfaces, they would indicate poor quality results most of the time. In the following, the emphasis is put on the array gain or processing gain produced by matched field processing. A main advantage of using array gain as a performance index is that it allows an intercomparison between matched field processing and the conventional beamformers. The array gain is estimated as in Chapter 4. The peak indicating the signal (generally the highest level peak) is used to measure the output signal-plus-noise level. The output noise level is measured for the same range and depth cell from the noise-only ambiguity surfaces. The array gain can then be computed using the estimate of the input signal-to-noise ratio.

#### 5.5.1. 11.8 dB Input SNR Case

Signal-plus-noise and noise-only data are summarized in Table 5.4 together with the array gain. The array gain of the Bartlett processor is on the order of 16 dB, 1 dB above the array gain achieved by the conventional FFT beamformer in Chapter 4, on the same data set. This computed array gain is lower than expected since it is 5 dB below the 21 dB maximum expected array gain. The MV processor is very sensitive to mismatch at high signal-to-noise ratios and its processing gain is poor. It increases with the covariance matrix stabilization thus indicating serious problems.

Processor	S+N dB	N dB	AG dB
Bartlett	79	51.47	15.7
MV ( $\gamma = 0.001$ )	49.6	36.1	1.5
MV ( $\gamma = 0.01$ )	54.4	39.9	2.5
MV ( $\gamma = 0.1$ )	60	45.3	2.7

**Table 5.4:** Array gain calculation (11.8 dB input SNR)

### 5.5.2. -9.2 dB Input SNR Case

The probable target is used to measure the signal-plus-noise peak levels. The MFP output for noise-only data are computed at the probable source range and depth for all four processors. The signal-plus-noise and noise-only levels are summarized in Table 5.5. The signal-only power levels are estimated and the output signal-to-noise ratios and array gains computed. The array gain for the Bartlett processor is on the order of 17.5 dB which is higher than the array gain for the high input SNR case. The presence of a peak in the ambiguity surface at the source location even with the source turned off explains perhaps such a discrepancy. The MFP Bartlett processor has an array gain 3 dB higher than the conventional FFT beamformer. Because of the lower input SNR, the MV processor is less sensitive to mismatch and performs more reasonably than in the high input SNR case. The MV array gain is between 11 and 13 dB and decreases as the amount of stabilization in the covariance matrix increases. This is consistent with the fact that additional artificial noise is added in the process.

Processor	S+N dB	N dB	AG dB
Bartlett	80.97	72.13	17.43
MV ( $\gamma = 0.001$ )	61.54	56.23	13.0
MV ( $\gamma = 0.01$ )	65.33	60.86	12.35
MV ( $\gamma = 0.1$ )	70.61	66.58	11.05

**Table 5.5:** Array gain calculations (-9.2 dB input SNR)

## 5.6. Conclusions

This chapter shows that matched field processing is a viable processing technique at 200 Hz with a 900 m long aperture array. The source at 20 m depth and 165 km range is detected at two input signal-to-noise ratios equal to 11.8 and -9.2 dB. The source localization is excellent in both range and depth. The environmental information collected at the time of the experiment at the R/P FLIP allows an appropriate modeling of the acoustic transmissions. Mismatch exists because of a severe 1° array tilt. The lack of robustness of the MV processor is observed with these real data. The estimated array gain of matched field processing using the conventional processor is found larger than the processing gain estimates of the conventional FFT beamformer. Even under large mismatch conditions, matched field processing appears to be a better beamforming approach for signal detection than is conventional processing.



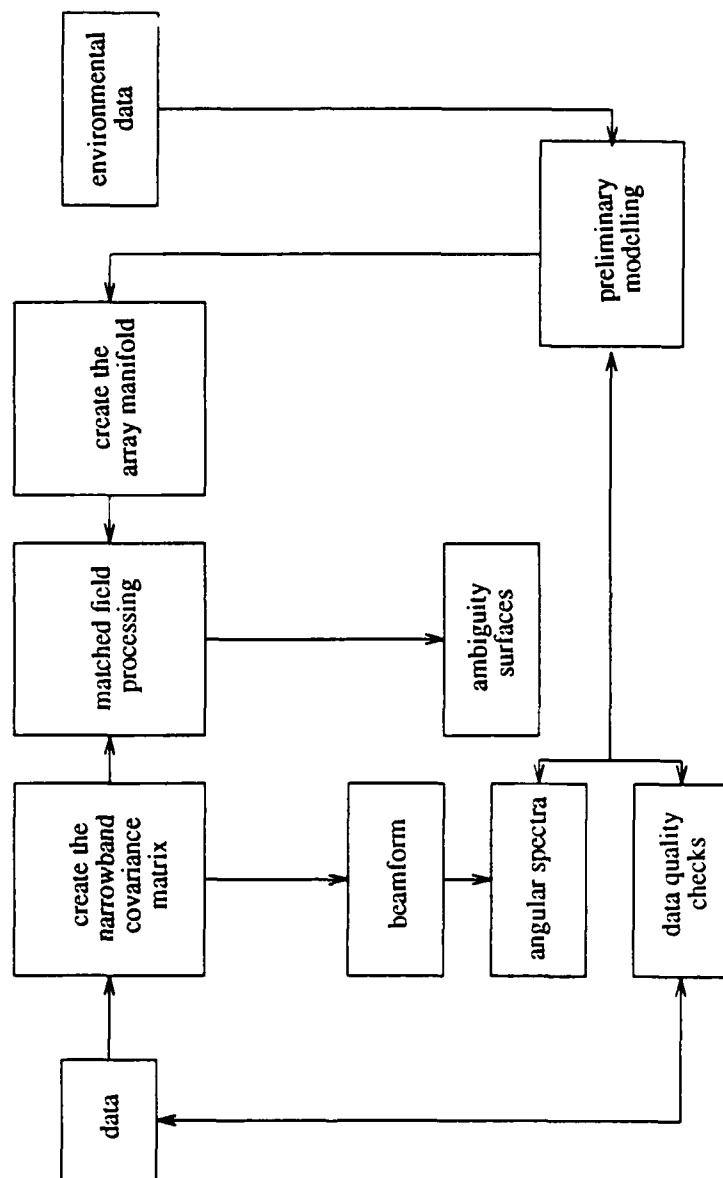
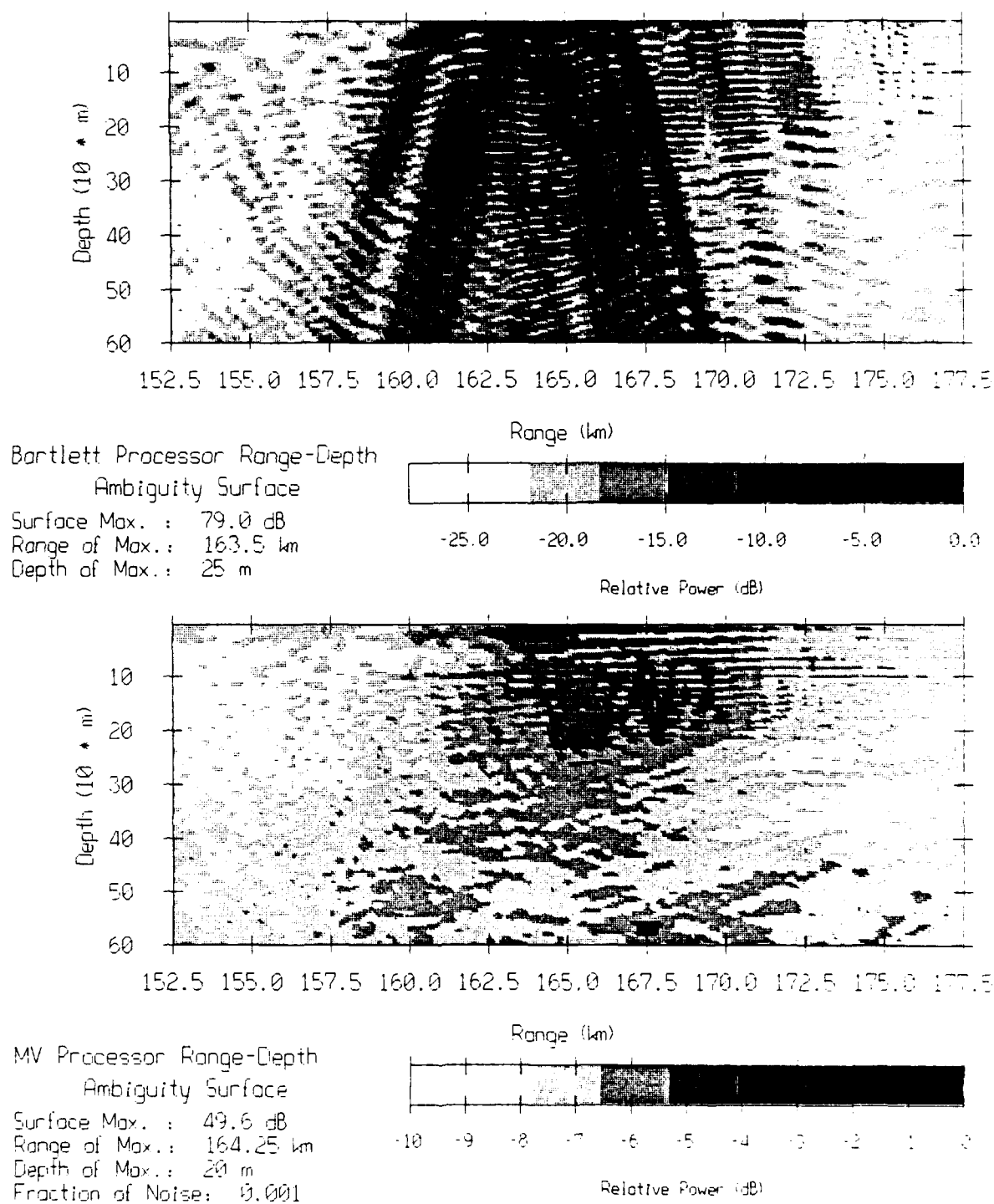
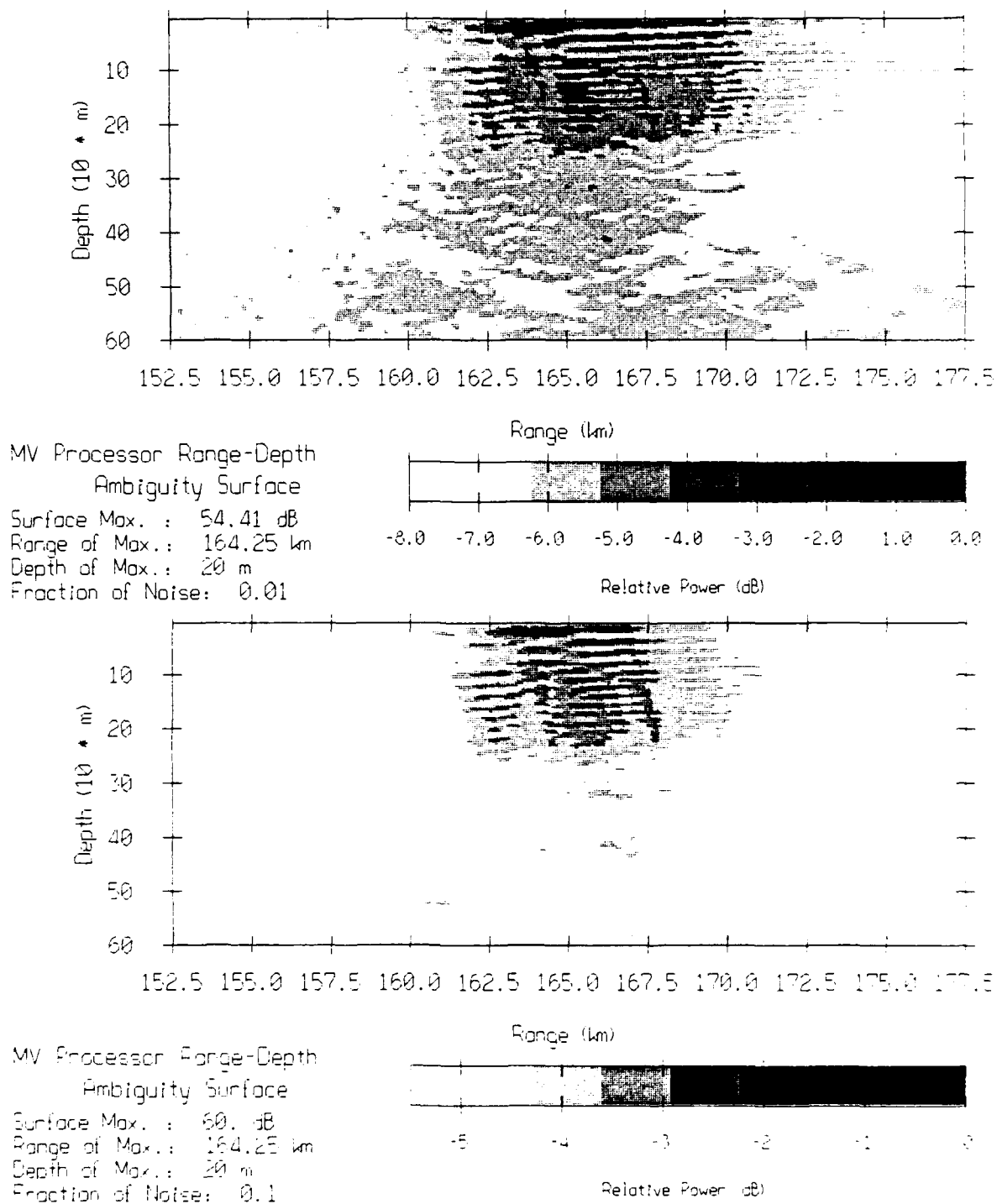


Figure 5.1: Matched Field Processing.



**Figure 5.2:** Matched field processing results on signal, part 1, (11.8 dB input SNR case).



**Figure 5.3:** Matched field processing results on signal, part 2, (11.8 dB input SNR case).

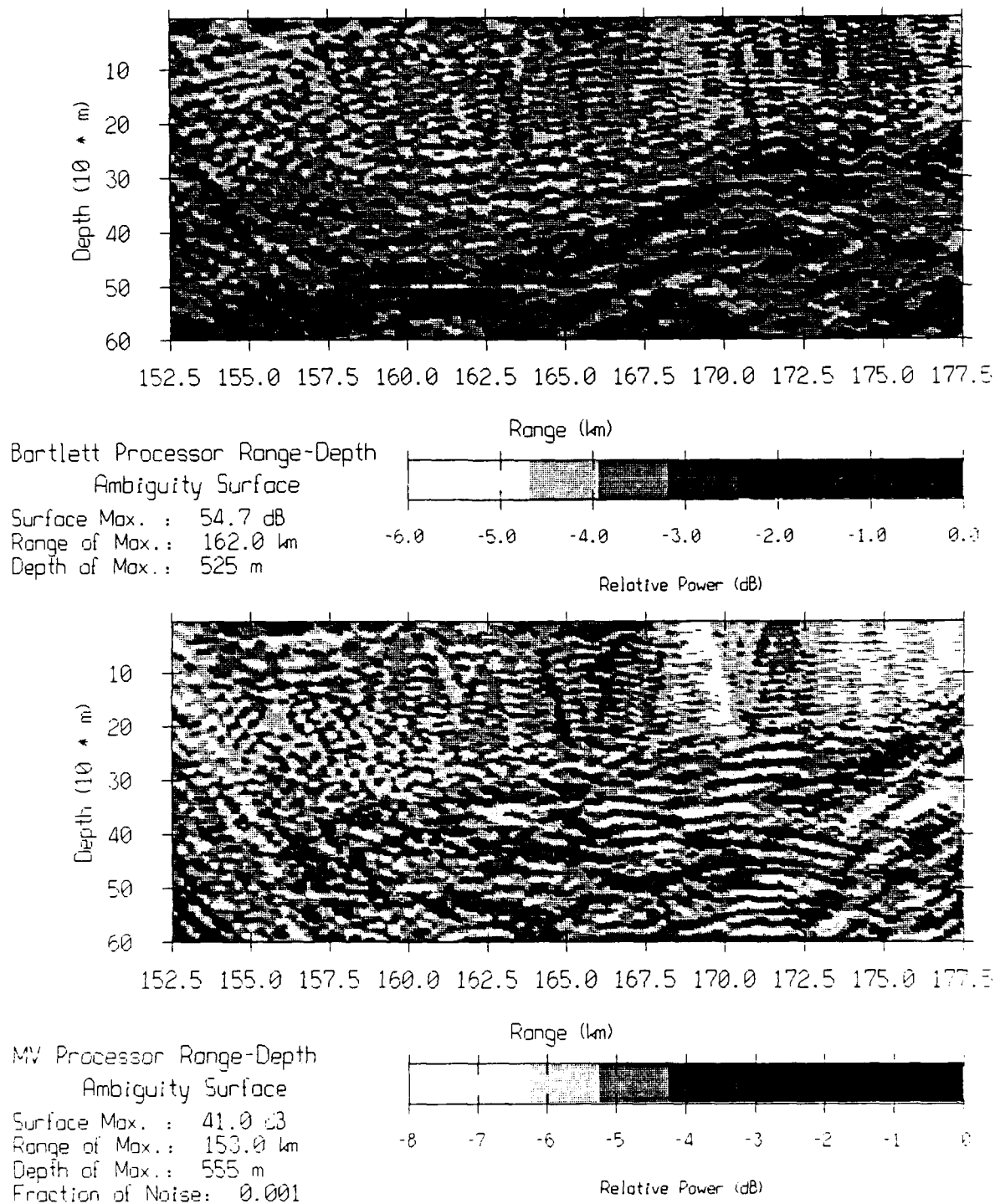


**Figure 5.4:** Matched field processing results on noise, part 1, (11.8 dB input SNR case).

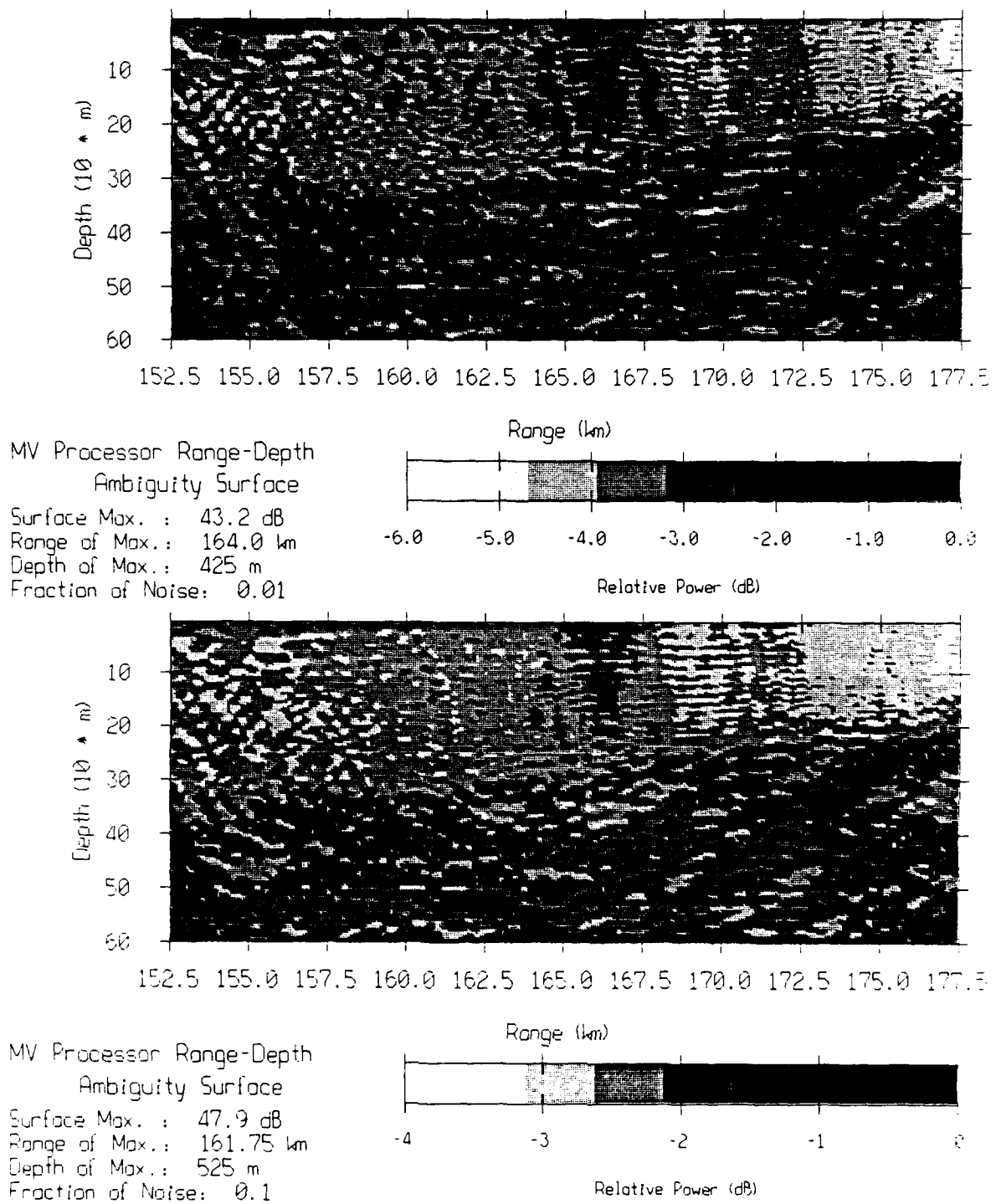


**Figure 5.5:** Matched field processing results on noise, part 2, (11.8 dB input SNR case).

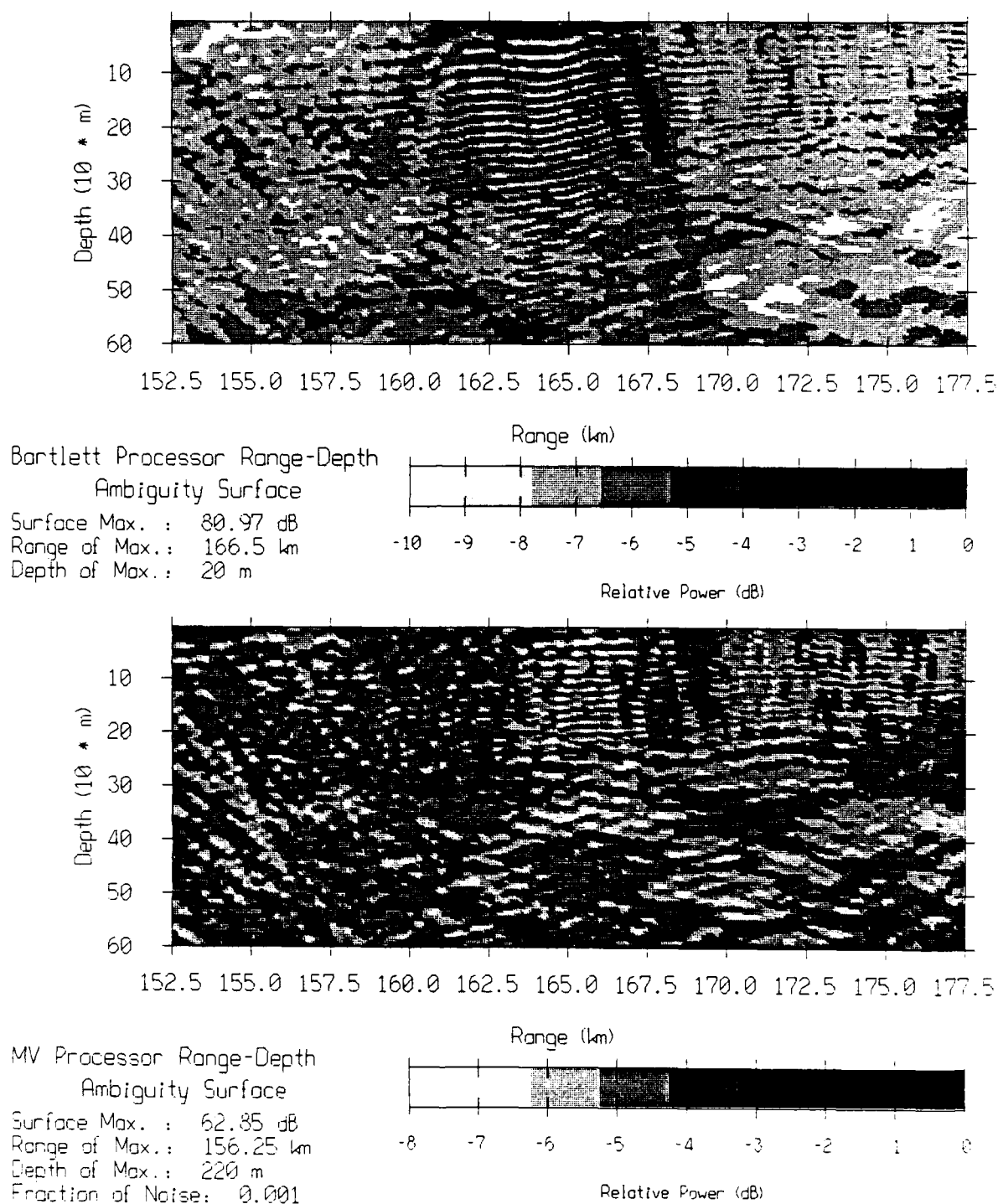


**Figure 5.6:** Matched field processing results on signal, part 1, (-9.2 dB input SNR case).

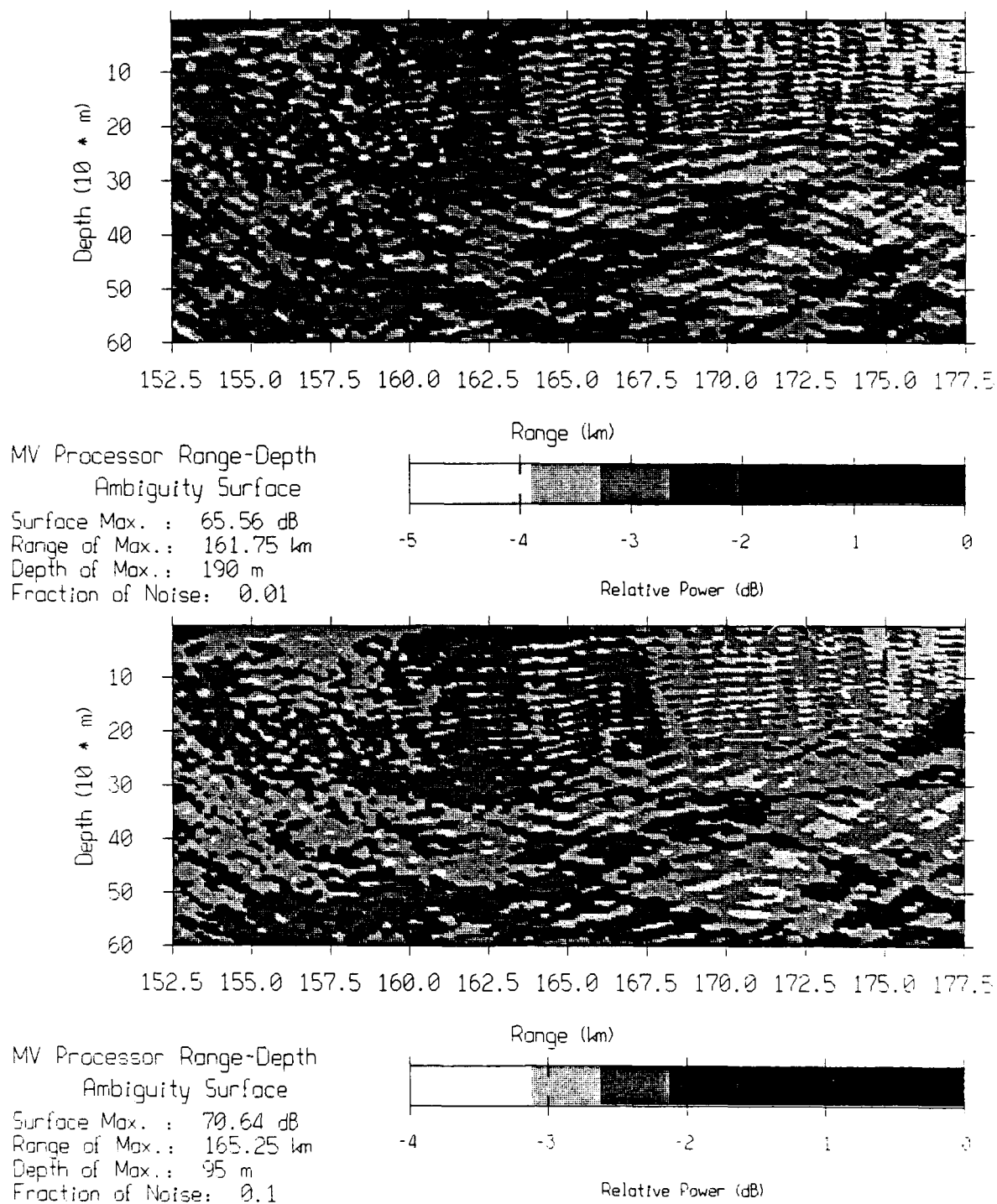


**Figure 5.7:** Matched field processing results on signal, part 2, (-9.2 dB input SNR case).

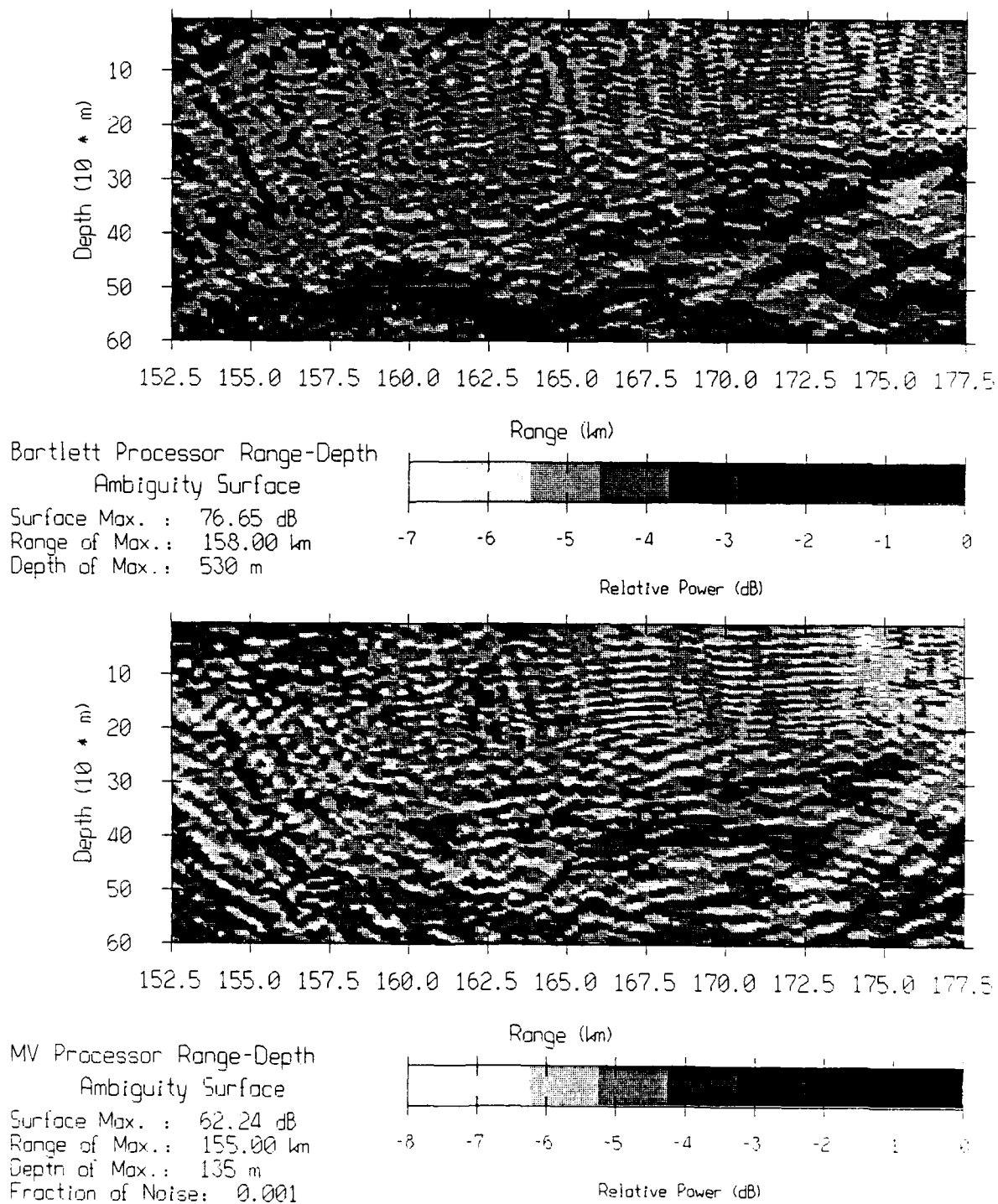


**Figure 5.8:** Matched field processing results on noise, part 1, (-9.2 dB input SNR case).



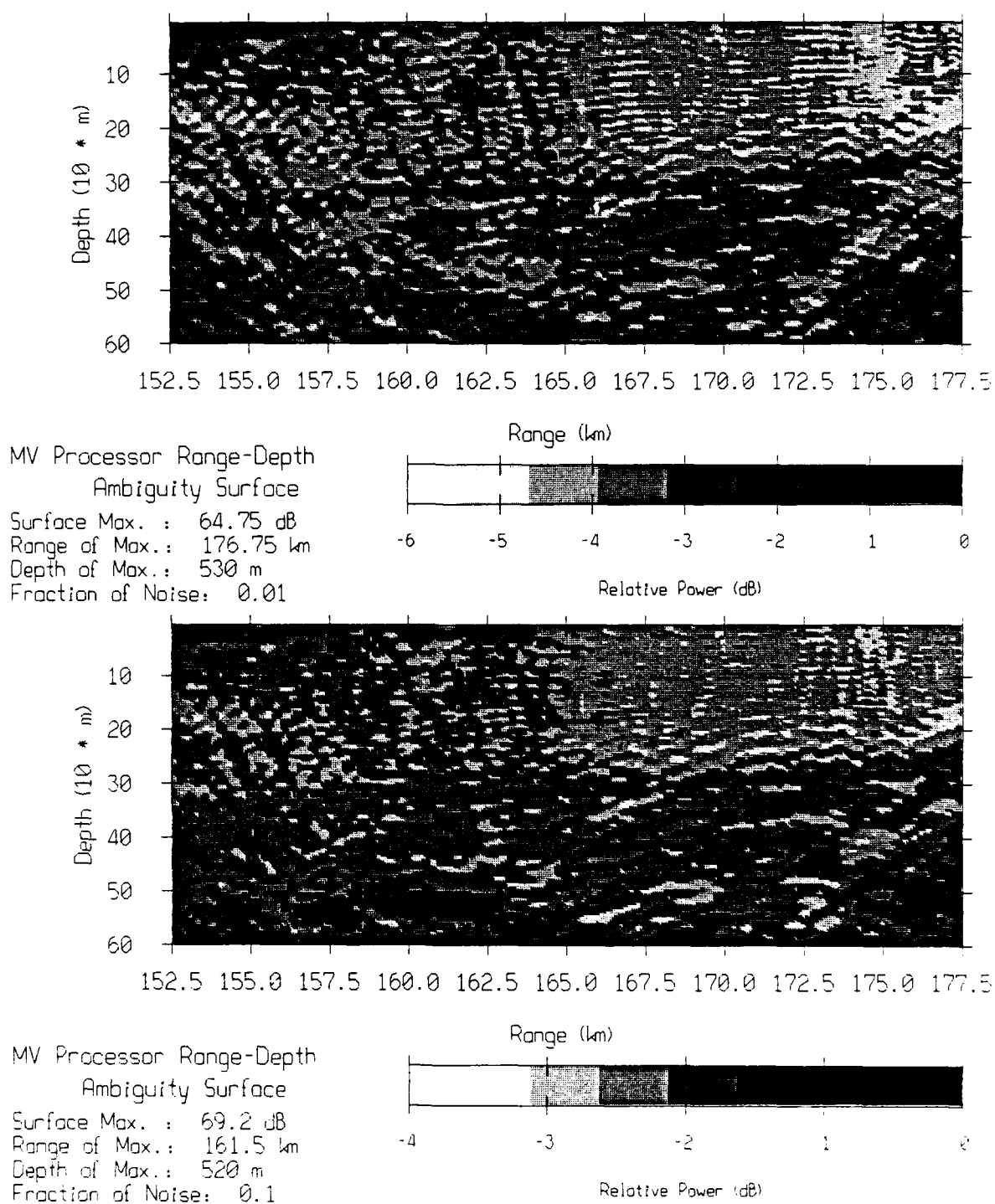


**Figure 5.9:** Matched field processing results on noise, part 2, (-9.2 dB input SNR case).

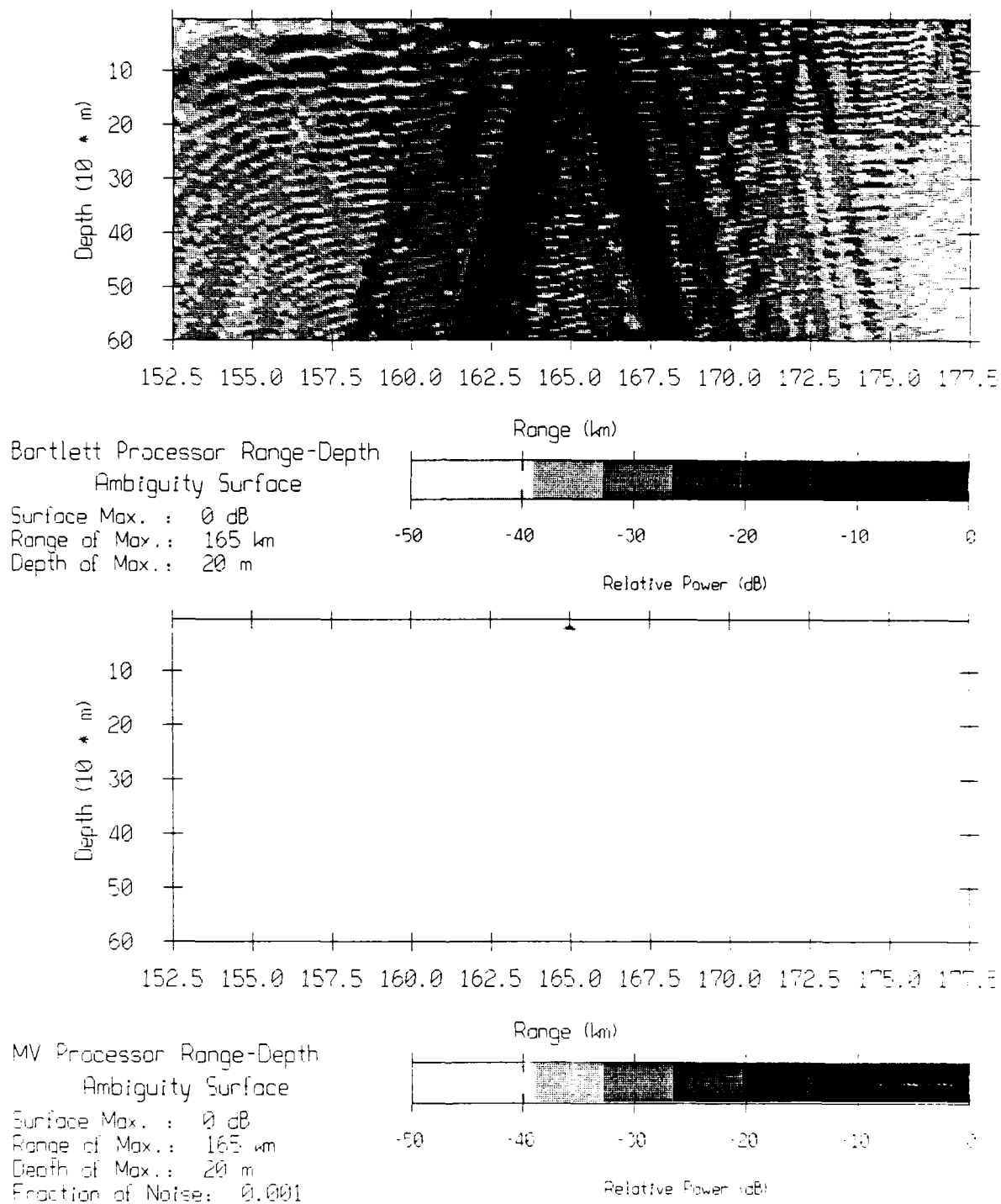


**Figure 5.10:** Matched field processing simulation, part 1, (no mismatch, no noise).

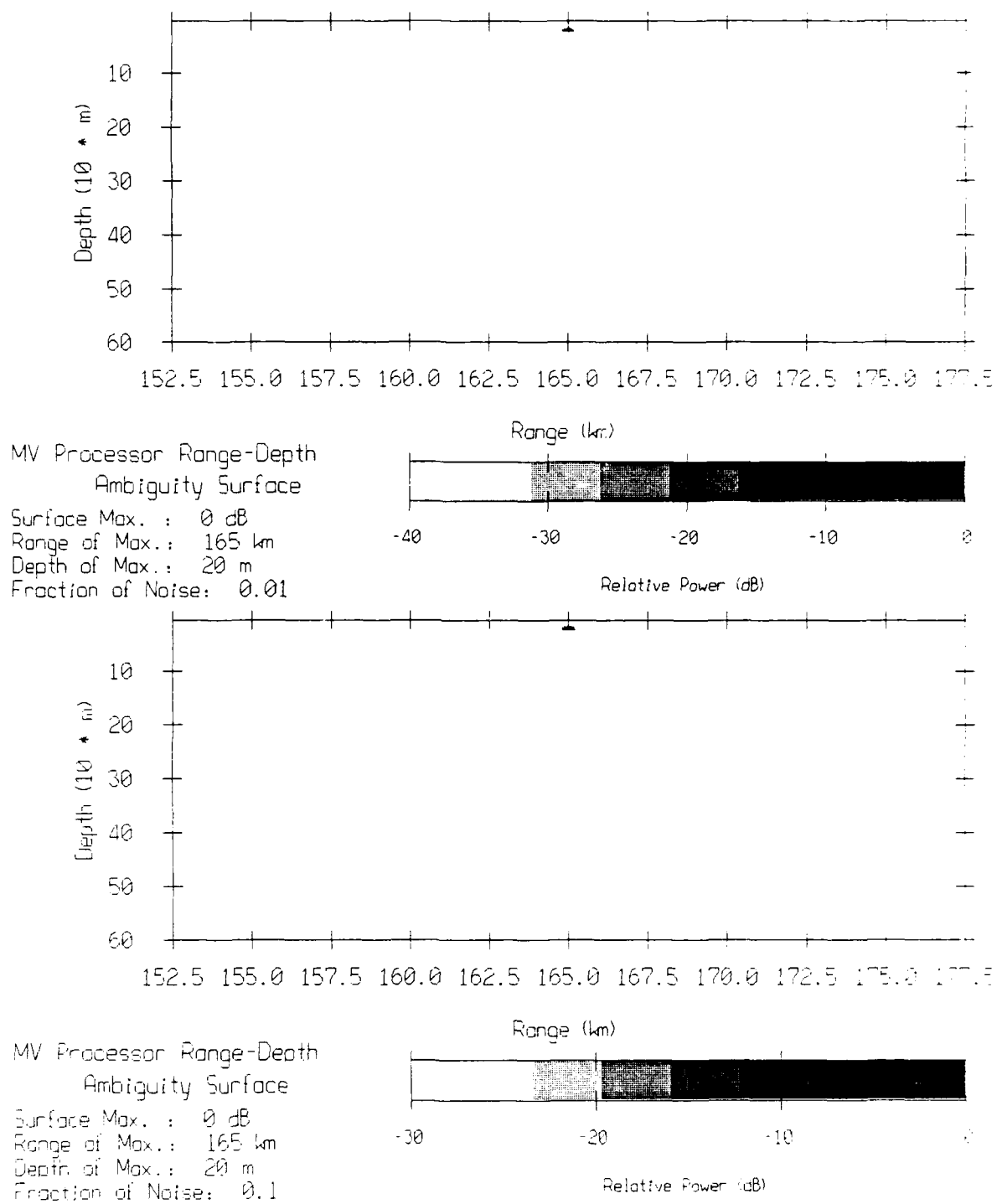


**Figure 5.11:** Matched field processing simulation, part 2 (no mismatch, no noise).

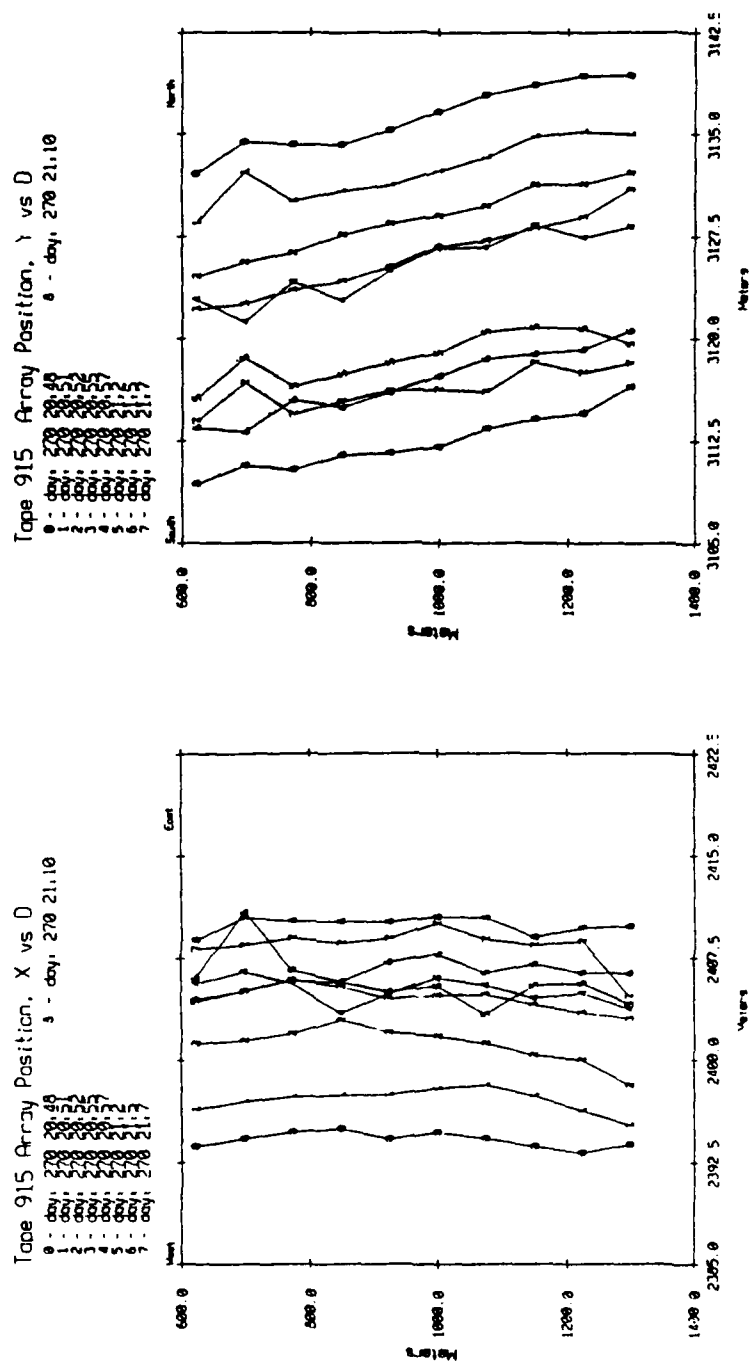
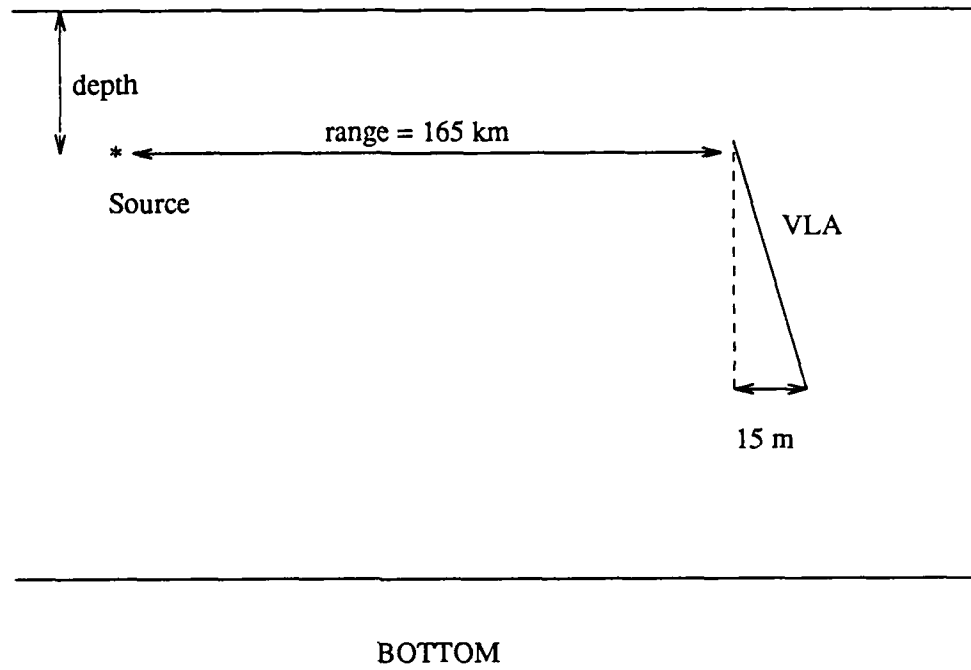
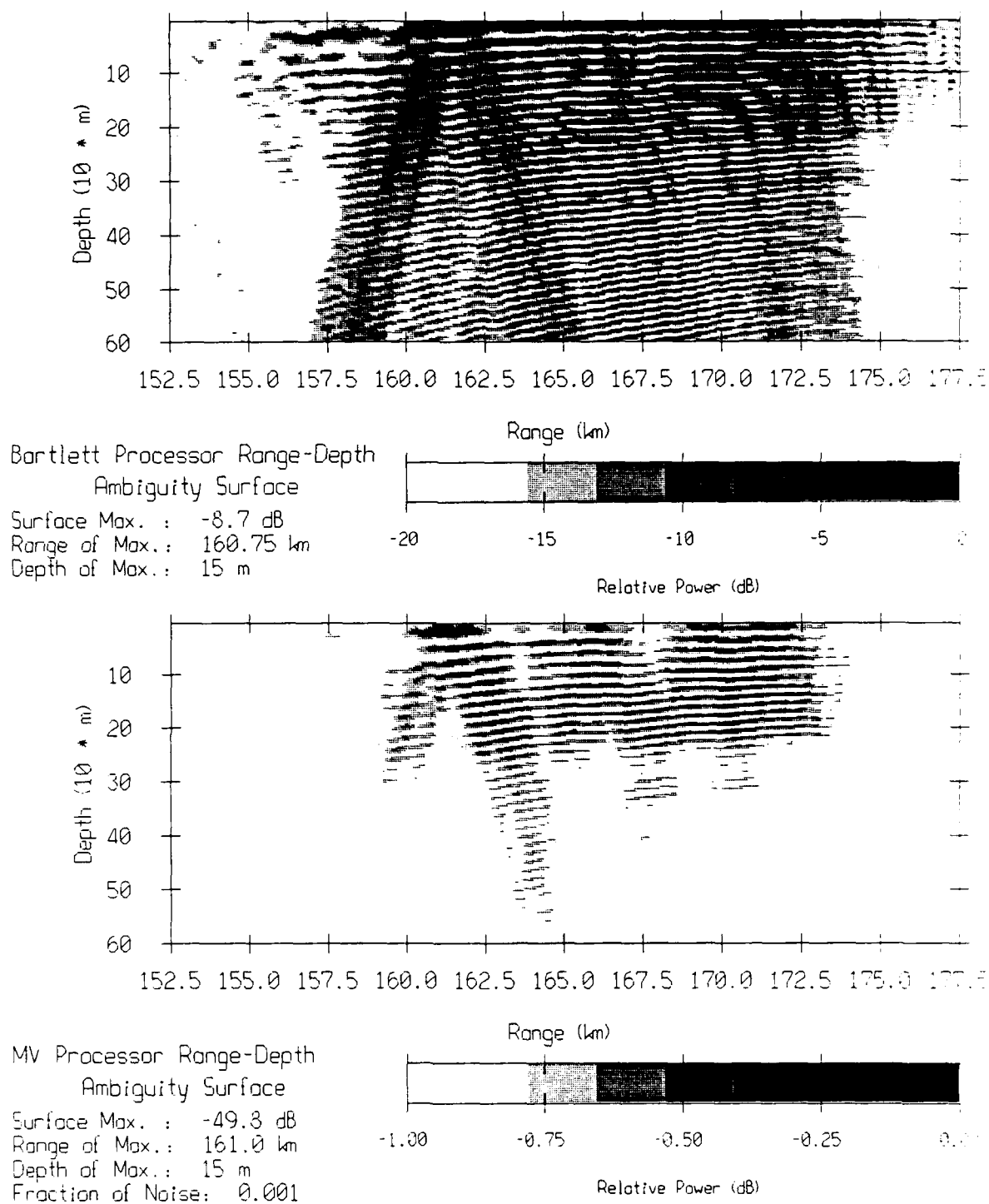


Figure 5.12: Array navigation data for Tape 915.



**Figure 5.13:** Tilted array simulation geometry.



**Figure 5.14:** Matched field processing simulation, part 1, (tilted array).

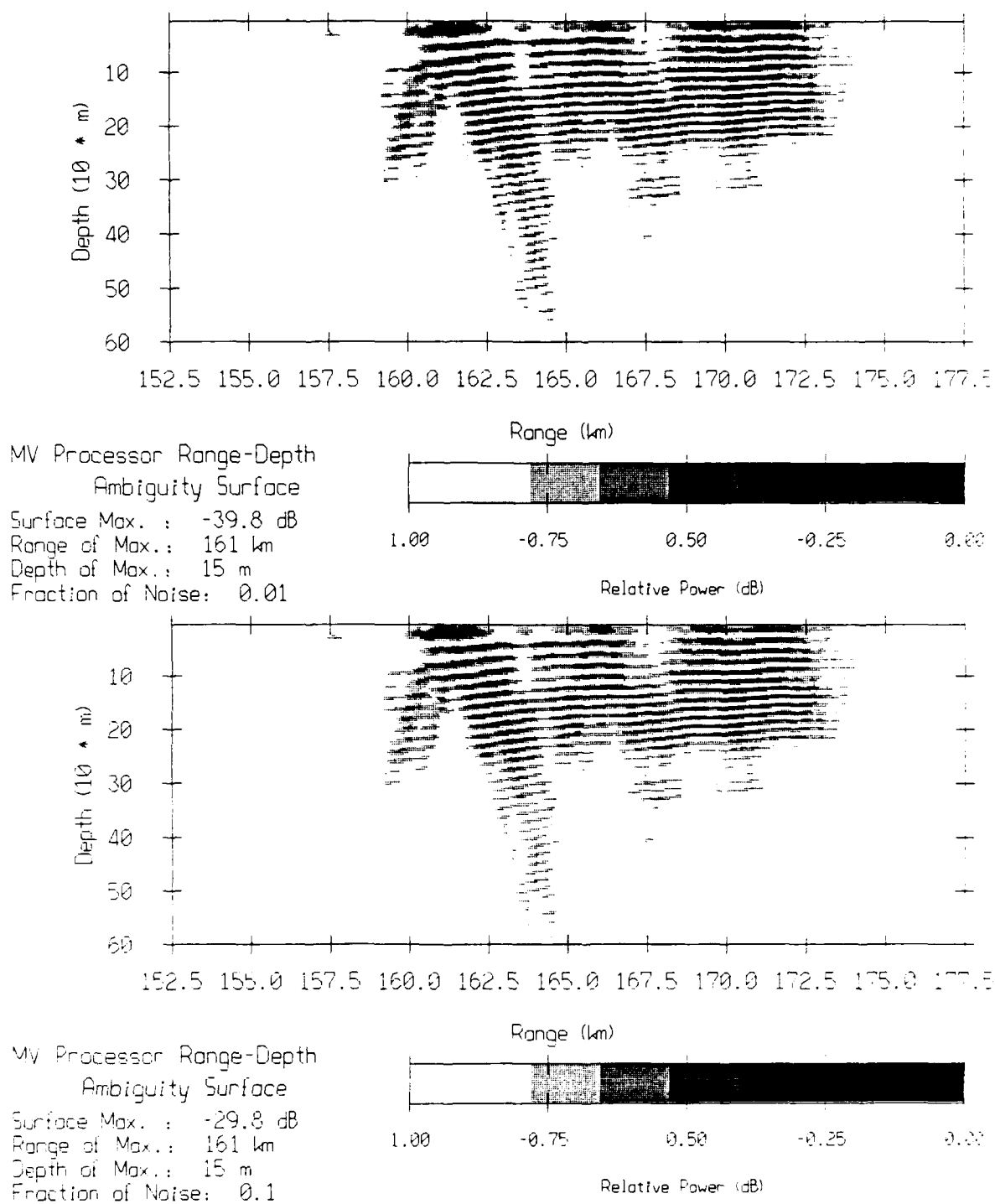


**Figure 5.15:** Matched field processing simulation, part 2, (tilted array).

## Conclusions

Various approaches to process the data from large aperture vertical line arrays have been examined in this dissertation. Depending on the available knowledge of the environment, beamforming or matched field processing can be used to enhance the detection of signals through an increase in signal-to-noise ratio, and also provide direction of arrival estimation or range-depth localization.

In a scenario where little is known on the oceanic environment, beamforming is performed to detect signals and estimate the field vertical arrival structure. The use of the adaptive Minimum Variance processor, with large aperture vertical line arrays, has been studied and its performance compared to the conventional FFT beamformer. As a preliminary to processing real data, the signal cancellation problem of correlated arrivals is examined and the spatial smoothing techniques interpreted. The mismatch due to wavefront curvature also is evaluated. It is shown that wavefront curvature should be taken into account for a 3000 m aperture array and for arrivals with low angle with respect to the horizontal. On the other hand, plane wavefront replica vectors can be used with a 900 m aperture array even at high input signal-to-noise ratio (on the order of 10 dB), when there is no arrival shallower than  $\pm 10^\circ$ . The estimation of a 100-sensor array covariance matrix requires a large number of data snapshots from a potentially nonstationary pressure field. For this reason, subaperture Minimum Variance processing was proposed. Using subapertures reduces the computational load in addition to the number of snapshots entering into the covariance matrix, but at the cost of processing gain and resolution because of the reduction of the aperture length. The full and subaperture processing schemes are validated in simulations and used on real data collected by the MPL digital array. The multipath arrivals are found to illuminate only parts of the array and based on the particular data set presented in this dissertation, a real wavefield may be highly inhomogeneous. Subaperture MV processing is shown to be valuable in illustrating the great multipath variability, but averaging subaperture angular spectra may not enhance the peaks in the composite estimate. The processing gain obtained with the MV processor is lower than the conventional FFT beamformer because of spatial smoothing or residual signal cancellation, and mismatch. On the other hand, resolution can be significantly improved, especially for high level arrivals.

The array gain estimates of the conventional FFT beamformer were found between 14 and 15 dB in the simulation and real data cases, i.e. 6 to 7 dB lower than what matched field processing would achieve in the case of no mismatch (21 dB or  $10 \log M$  where  $M$  is the number of sensors). Matched field processing was attempted on 200 Hz real data signals that propagated to the MPL array over 165 km. The available knowledge of the environment, the acoustic modeling and the good quality of the data make this attempt successful. Generally, the source is correctly localized in range and depth. The main cause of mismatch is identified to be the array tilt, at most equal to  $1^\circ$  (which corresponds to a horizontal displacement of two wavelengths at 200 Hz from the top to the bottom of the array). Although mismatch is present, the processing gain estimates of the MFP Bartlett processor are 1 to 3 dB larger than the conventional FFT beamformer array gain estimates. The MV processing is found to perform poorly as a result of mismatch and lack of robustness.

A few aspects in this dissertation should be the subject of further investigations. The beamforming schemes proposed here can be implemented with processors other than the Minimum Variance processor which is known to be very sensitive to mismatch at high signal-to-noise ratio. The adaptive processor under additional constraints (for example the multiple point constraints or the derivative



constraints [Van Veen1989]), where "real world" perturbations are accommodated, should enjoy more robustness which is an important characteristic when processing real data. The problem of the variance of the angular spectra produced by the Minimum Variance processor was not addressed in this dissertation and should be studied in order to treat issues related to detectability. In this dissertation, the emphasis was put on a 900 m aperture and the MPL digital array. With larger aperture arrays expected in the future, it would be interesting to test further via simulation and the processing of real data the curved wavefront beamforming techniques. Finally, although matched field processing did perform reasonably well, efforts should be directed toward using more robust processors than the Minimum Variance processor. In addition, the array navigation data (sensor position) should be incorporated into the processing and the increase in array gain measured.

## References

- Anderson, V. C., "Vertical Noise Distribution," in *International Workshop on Low Frequency Propagation*, vol. 2, pp. 859-886, Woodshole, MA, October 1974.
- Anderson, V. C., "Variation of Directionality of Noise with Depth in the North Pacific," *J. Acoust. Soc. Am.*, vol. 66, no. 5, pp. 1446-1452, 1979.
- Baggeroer, A. B., "High Resolution Velocity/Depth Spectra Estimation for Seismic Profiling," *IEEE Inter. Conf. Engineering in the Environment, OCEAN 74*, vol. 2, pp. 201-211, Halifax, Nova Scotia, 21-23 August 1974.
- Baggeroer, A. B. and R. Falconer, "Refraction Profiles and Crustal Models of the Canada Basin," *J. Geophys. Res.*, vol. 87, no. B7, pp. 5461-5476, 1982.
- Baggeroer, A. B., *Robust Beamforming Issues for Large Arrays*, October 1985.
- Baggeroer, A. B., W. A. Kuperman, and H. Schmidt, "Matched Field Processing: Source Localization in Correlated Noise as an Optimum Parameter Estimation Problem," *J. Acoust. Soc. Am.*, vol. 83, no. 2, pp. 571-587, 1988.
- Barnard, T. E., "Two Maximum Entropy Beamforming Algorithms for Equally Spaced Line Array," *IEEE Trans. Acoust. Speech Signal Processing*, vol. 30, no. 2, pp. 175-189, 1982.
- Baxley, P. A. and J-M. Tran, "The Adverse Effects of a Mismatched Surface Layer in Matched Field Depth Discrimination," *Fourth Matched Field Processing Workshop*, Defence Research Establishment Pacific, Victoria, B.C. Canada, September 6-8 1989.
- Bohme, J. F., "Array Signal Processing," in *Traitement du Signal / Signal Processing*, ed. J. L. Lacoume, T. S. Durrani and R. Stora, pp. 438-482, Elsevier, 1987.
- Boroson, D. M., "Sample Size Considerations for Adaptive Arrays," *IEEE Trans. Aerosp. Electron. Syst.*, vol. 16, no. 4, pp. 446-451, 1980.
- Boyles, A. C., *Acoustic Waveguides, Applications to Oceanic Science*, John Wiley, N.Y., 1984.
- Brekhovskikh, L. and Yu. Lysanov, *Fundamentals of Ocean Acoustics*, Springer Verlag, Berlin, 1982.
- Brennan, L. E. and L. S. Reed, "Theory of Adaptive Arrays," *IEEE Trans. Aerosp. Electron. Syst.*, vol. 9, no. 2, pp. 237-252, 1973.
- Bucker, H. P., "Use of Calculated Sound Fields and Matched Field Detection to Locate Sound Sources in Shallow Water," *J. Acoust. Soc. Am.*, vol. 59, no. 2, pp. 368-373, 1976.

- Burdic, W. S., *Underwater Acoustic System Analysis*, Prentice-Hall, Englewood Cliffs, N.J., 1984.
- Burg, J. P., "Maximum Entropy Spectral Analysis," *Proc 37th Meeting of the Society of Exploration Geophysicists*, Oklahoma City, OK, 31 October 1967.
- Cadzow, J. A., "A High Resolution Direction-of-Arrival Algorithm for Narrow-Band Coherent and Incoherent Sources," *IEEE Trans. Acoust. Speech Signal Processing*, vol. 36, no. 7, pp. 965-979, 1988.
- Cantoni, A. and L. C. Gondara, "Resolving the Directions of Sources on a Correlated Field Incident on an Array," *J. Acoust. Soc. Am.*, vol. 67, no. 4, pp. 214-219, 1980.
- Capon, J., "High Resolution Frequency-Wavenumber Spectrum Analysis," *Proc. IEEE*, vol. 57, pp. 1408-1418, 1969.
- Capon, J. and N. R. Goodman, "Probability Distribution for Estimators of the Frequency Wavenumber Spectrum," *Proc. IEEE (Lett.)*, vol. 58, pp. 1785-1786, 1970.
- Carlson, B. D., "Covariance Matrix Estimation Errors and Diagonal Loading in Adaptive Arrays," *IEEE Trans. Aerosp. Electron. Syst.*, vol. 24, no. 4, pp. 397-401, 1988.
- Clarke, I. J., "High Discrimination Target Detection Algorithms and Estimation of Parameters," *Nato Advanced Study Institute on Underwater Acoustic Data Processing*, Kingston, Ontario, Canada, 18 July to 29 July 1988.
- Cox, H., "Resolving Power and Sensitivity to Mismatch of Optimum Array Processors," *J. Acoust. Soc. Am.*, vol. 54, no. 3, pp. 771-785, 1973.
- Cox, H., R. M. Zeskind, and M. M. Owen, "Robust Adaptive Beamforming," *IEEE Trans. Acoust. Speech Signal Processing*, vol. 35, no. 10, pp. 1365-1375, 1987.
- Del Bazo, D. R., C. Feuillade, and Mary M. Rowe, "Effects of water-depth mismatch on matched field localization in shallow water," *J. Acoust. Soc. Am.*, vol. 83, no. 6, June 1988.
- De Fatta, D., J. Lucas, and W. Hodgkiss, *Digital Signal Processing*, John Wiley, N.Y., 1988.
- De Graaf, S. R. and D. H. Johnson, "Capability Of Array Processing Algorithms To Estimate Source Bearings," *IEEE Trans. Acoust. Speech Signal Processing*, vol. 33, no. 6, pp. 1368-1379, 1985.
- Dosso, S. E. and N. R. Chapman, "Measurement and Modeling of Downslope Acoustic Propagation Loss over a Continental Slope," *J. Acoust. Soc. Am.*, vol. 81, no. 2, pp. 258-268, 1987.
- Feuillade, C., D. R. Del Bazo, and Mary M. Rowe, "Environmental mismatch in shallow-water matched field processing: Geoacoustic parameter variability," *J. Acoust. Soc. Am.*, vol. 83, no. 6, June 1989.

- Fizell, R. G., "Application of High-Resolution Processing to Range and Depth Estimation Using Ambiguity Function Methods," *J. Acoust. Soc. Am.*, vol. 82, no. 2, pp. 606-613, 1987.
- Fofonoff, N. P., *Algorithms for the Computation of Fundamental Properties of Seawater*, Technical Paper 44, Unesco Division of Marine Sciences, Paris, France, 1983.
- Gabriel, W. F., "Spectral Analysis and Adaptive Array Superresolution Techniques," *Proc. IEEE*, vol. 68, pp. 654-666, 1980.
- Gabriel, W. F., "Using Spectral Estimation Techniques in Adaptive Processing Antenna Systems," *IEEE Trans. Ant. Prop.*, vol. 34, no. 3, pp. 291-300, 1986.
- Gammelsaeter, O. B., "Adaptive Beamforming with Emphasis on Narrowband Implementation," in *Underwater Acoustics and Signal Processing*, ed. Leif Bjorno, pp. 307-326, D. Reidel Publishing Company, Dordrecht-Holland, 1981.
- Golub, G. H. and C. F. Van Loan, *Matrix Computations*, John Hopkins University Press, 1985.
- Goodman, N. R., "Statistical Analysis Based on a Certain Multivariate Complex Gaussian Distribution (An Introduction)," *Ann. Math. Stat.*, vol. 34, pp. 152-177, 1963.
- Gordon, D. F. and H. P. Buckner, *Arctic Acoustic Propagation Model with Ice Scattering*, NOSC Technical Report 985, 30 September 1984.
- Griffiths, J. W. R. and J. E. Hudson, "An Introduction to Adaptive Processing in Passive Sonar System," in *Aspects of Signal Processing with Emphasis on Underwater Acoustics*, ed. G. Tacconi, vol. 1, pp. 299-308, D. Reidel Publishing Company, Dordrecht-Holland, 1977.
- Heitmeyer, R. M., W. B. Moseley, and R. G. Fizell, "Full Field Ambiguity Function Processing in a Complex Shallow Water Environment," in *High-Resolution Spatial Processing in Underwater Acoustics*, ed. A. B. Baggeroer, pp. 171-191, Naval Ocean Research and Development Activity, NSTL, Mississippi, 1985.
- Hsu, K. and A. B. Baggeroer, "Application of the Maximum Likelihood Method (MLM) for Sonic Logging," *Geophysics*, vol. 551, no. 3, pp. 780-787, 1986.
- Hudson, J. E., *Adaptive Array Principles*, Peter Peregrinus Ltd., U.K., 1981.
- Hung, E. K. L., R. M. Turner, and R. W. Herring, "A Pitfall in Using the Pseudoinverse of a Singular Covariance Matrix in Adaptive Signal Processing," *ASSP Workshop on Spectral Estimation*, pp. 253-258, 1983.
- Johnson, D. J. and S. R. De Graaf, "Improving the Resolution of Bearing in Passive Sonar Arrays by Eigenvalue Analysis," *IEEE Trans. Acoust. Speech Signal Processing*, vol. 30, no. 4, pp. 638-647, 1982.
- Kanasewich, E. R., *Time Sequence Analysis in Geophysics*, University of Alberta Press, Edmonton, Alberta, 1975.

- Kay, S. M., *Modern Spectral Estimation, Theory & Applications*, Prentice-Hall, Englewood Cliffs, N.J., 1988.
- Kelly, E. J., "Performance of an Adaptive Detection Algorithm; Rejection of Unwanted Signals," *IEEE Trans. Aerosp. Electron. Syst.*, vol. 25, no. 2, pp. 122-133, 1989.
- Kewley, D. J., "Using Eigenvalue Analysis to Identify Interference in Ambient Sea Noise Vertical Directionality Measurements," *J. Acoust. Soc. Am.*, vol. 75, no. 3, pp. 826-833, 1984.
- Kumaresan, R. and D. W. Tufts, "Estimating the Angle of Arrival of Multiple Plane Waves," *IEEE Trans. Aerosp. Electron. Syst.*, vol. 19, no. 1, pp. 134-139, 1983.
- Kung, S. Y., *VLSI Array Processors*, Prentice Hall, Englewood Cliffs, N.J., 1988.
- Lacoss, R. T., "Data Adaptive Spectral Analysis Methods," *Geophys.*, vol. 36, pp. 661-675, 1971.
- Linebarger, D. A. and D. H. Johnson, "The Effect of Spatial Averaging on Coherence and Resolution," *Proc. ICASSP 1988*, vol. V, pp. 2865-2868, 1988.
- Lunde, E. B., "The Forgotten Algorithm in Adaptive Beamforming," in *Aspects of Signal Processing With Emphasis on Underwater Acoustics*, ed. G. Tacconi, vol. 2, pp. 406-413, Reidel Publishing Company, Dordrecht-Holland, 1976.
- Mackenzie, K. V., "Nine-term Equation for Sound Speed in the Oceans," *J. Acoust. Soc. Am.*, vol. 70, no. 3, p. 808, September 1981.
- Maksym, J. N., "A Robust Formulation of an Optimum Cross-spectral Beamformer for Line Arrays," *J. Acoust. Soc. Am.*, vol. 65, no. 4, pp. 971-975, 1979.
- Marple, S. L., *Digital Spectral Analysis with Applications*, Prentice-Hall, Englewood Cliffs, N.J., 1987.
- McDonough, R. N., "Degraded Performance of Nonlinear Array Processors in the Presence of Data Modeling Errors," *J. Acoust. Soc. Am.*, vol. 51, no. 4, pp. 1186-1193, 1972.
- Monzingo, R. A. and T. W. Miller, *Introduction to Adaptive Arrays*, John Wiley, N.Y., 1980.
- Murphy, D. A. and D. R. Del Bazo, "Multipath Processing for Improved Detection on a Long Vertical Array," in *Progress in Underwater Acoustics*, ed. H. M. Merklinger, pp. 765-772, Plenum Press, N.Y., 1987.
- Naidu, P. S. and V. V. Krishna, "Improved Maximum Likelihood Spectrum For Direction Of Arrival (DOA) Estimation," *Proc. ICASSP 1988*, vol. V, pp. 2901-2904, 1988.
- Nickel, U., "Angular Superresolution with Phased Array Radar: A Review of Algorithms and Operational Constraints," *IEE Proc. Part F*, vol. 134, no. 1, pp. 53-59, 1988.

- Oltman-Shay, J. and R. T. Guza, "A Data-Adaptive Ocean Wave Directional Spectrum Estimation for Pitch and Roll Type Measurements," *J. Physical Oceanography*, vol. 14, pp. 1800-1810, 1984.
- Oppenheim, A. V. and R. W. Schaffer, *Digital Signal Processing*, Prentice-Hall, N.J., 1975.
- Orfanidis, S. J., *Optimum Signal Processing, An Introduction*, Macmillan, N.Y., 1988.
- Owsley, N. L., "Sonar Array Processing," in *Array Signal Processing*, ed. S. Haykin, pp. 115-193, Prentice-Hall, Englewood Cliffs, N.J., 1985.
- Penrose, R., "A Generalized Inverse for Matrices," *Proc. Cambridge Philos. Soc.*, vol. 51, pp. 406-413, 1955.
- Pillai, S. U. and B. H. Kwon, "Forward/Backward Spatial Smoothing Techniques for Coherent Signal Identification," *IEEE Trans. Acoust. Speech Signal Processing*, vol. 37, no. 1, pp. 8-15, 1989.
- Pillai, S. U., *Array Signal Processing*, Springer Verlag, N.Y., 1989.
- Polvani, D. G., "Harmonic Sound Speed is Adequate for Transponder Navigation," *IEEE Oceans Conference Record*, vol. 1, 1984.
- Porter, M. B., R. L. Dicus, and R. G. Fizell, "Simulations of Matched Field Processing in a Deep-Water Pacific Environment," *IEEE J. Ocean. Eng.*, vol. 12, no. 1, pp. 173-181, January 1987.
- Priestley, M. B., *Spectral Analysis And Time Series*, 1, Academic, N.Y., 1981.
- Reddy, V. U., A. Paulraj, and T. Kailath, "Performance Analysis of the Optimum Beamformer in the Presence of Correlated Sources and its Behaviour under Spatial Smoothing," *IEEE Trans. Acoust. Speech Signal Processing*, vol. 35, no. 7, pp. 927-936, 1987.
- Reed, L. S., J. D. Mallet, and L. E. Brennan, "Rapid Convergence Rate in Adaptive Arrays," *IEEE Trans. Aerosp. Electron. Syst.*, vol. 10, no. 6, pp. 853-863, 1974.
- Schmidt, R. O., "Multiple Emitter Location and Signal Parameter Estimation," *IEEE Trans. Ant. Prop.*, vol. 34, no. 3, pp. 276-280, 1986.
- Seglison, C. D., "Comments on 'High Resolution Frequency Wavenumber Spectrum Analysis'," *Proc. IEEE (Lett.)*, vol. 58, no. 6, pp. 947-949, 1970.
- Sen, M. K., L. N. Frazer, S. Mallick, and N. R. Chapman, "Analysis of Multipaths Sound Propagation in the Ocean Near 49 N 128 W," *J. Acoust. Soc. Am.*, vol. 83, no. 2, pp. 588-597, 1988.
- Shan, Tie-Jun and T. Kailath, "Adaptive Beamforming for Coherent Signals and Interference," *IEEE Trans. Acoust. Speech Signal Processing*, vol. 33, no. 3, pp. 527-536, 1985.

- Shumway, R. H., *Applied Statistical Time Series Analysis*, Prentice-Hall, Englewood Cliffs, N.J., 1988.
- Smith, G. B., C. Feuillade, D. R. Del Bazo, and C. L. Byrne, "A Nonlinear Matched-Field Processor for Detection and Localization of a Quiet Source in a Noisy Shallow Water Environment," *J. Acoust. Soc. Am.*, vol. 85, no. 3, pp. 1158-1166, 1989.
- Sotirin, B. J. and J. A. Hildebrand, "Large Aperture Digital Acoustic Array," *IEEE J. Ocean. Eng.*, vol. 13, no. 4, pp. 271-281, 1989a.
- Sotirin, B. J., *Large Aperture Acoustic Array*, Marine Physical Laboratory Technical Memorandum MPL-U-47/89, Scripps Institution of Oceanography, San Diego, Ca., 1989b.
- Su, Y. L., T. J. Shan, and B. Widrow, "Parallel Spatial Processing: A Cure for Signal Cancellation in Adaptive Arrays," *IEEE Trans. Ant. Prop.*, vol. 34, no. 3, pp. 347-355, 1986.
- Takao, K. and N. Kikuma, "Tamed Adaptive Antenna Array," *IEEE Trans. Ant. Prop.*, vol. 34, no. 3, pp. 388-394, 1986.
- Takao, K. and N. Kikuma, "An Adaptive Array Utilizing an Adaptive Spatial Averaging Technique for Multipaths Environment," *IEEE Trans. Ant. Prop.*, vol. 35, no. 12, pp. 1389-1396, 1987.
- Tran, J-M. and W. S. Hodgkiss, *High Resolution Beamforming on Large Vertical Line Arrays: Processing Synthetic Data*, Marine Physical Laboratory, Scripps Institution of Oceanography (in preparation), (1989b).
- Tran, J-M. and W. S. Hodgkiss, *A Performance Study of Full Aperture and Subaperture Processing on Vertical Line Arrays with the MV Processor*, Marine Physical Laboratory, Scripps Institution of Oceanography (in preparation), (1989c).
- Tran, J-M. and W. S. Hodgkiss, *Processing Real Data with the Full Aperture and Subaperture MV beamformer*, Marine Physical Laboratory, Scripps Institution of Oceanography (in preparation), (1989d).
- Tran, J-M. and W. S. Hodgkiss, *High Resolution Beamforming on Vertical Arrays in a Realistic Oceanic Environment*, Marine Physical Laboratory Technical Memorandum MPL-U-03/89, Scripps Institution of Oceanography, San Diego, Ca., 1989a.
- Urick, R. J., *Principles of Underwater Sound*, McGraw-Hill, New York, N.Y., 1983.
- Urick, R. J., *Ambient Noise in the Sea*, Peninsula, Los Altos, Ca., 1986.
- Van Veen, B. D. and K. M. Buckley, "Beamforming: A Versatile Approach to Spatial Filtering," *IEEE ASSP Magazine*, vol. 5, no. 2, pp. 4-24, 1988.
- Velardo, P. M., *Robust Matched Field Source Localization*, Massachusetts Institute of Technology, MS Thesis, 1989.

- Vural, A. M., "Effects of Perturbations on the Performance of the Optimum/Adaptive Arrays," *IEEE Trans. Aerosp. Electron. Syst.*, vol. 15, no. 1, pp. 76-87, 1979.
- Wang, H. and M. Kaveh, "Coherent Signal-Subspace Processing for the Detection and Estimation of Angles of Arrival of Multiple Wide-Band Sources," *IEEE Trans. Acoust. Speech Signal Processing*, vol. 33, no. 4, pp. 823-831, 1985.
- Weinberg, H., *Generic Sonar Model*, NUSC Technical Document 5971-D, 6 June 1985.
- White, W. D., "Angular Spectra in Radar Applications," *IEEE Trans. Aerosp. Electron. Syst.*, vol. 15, no. 6, pp. 895-899, 1979.
- Widrow, B., K. M. Duvall, R. P. Gooch, and W. C. Newman, "Signal Cancellation Phenomena in Adaptive Antennas: Causes and Cures," *IEEE Trans. Ant. Prop.*, vol. 30, no. 3, pp. 469-478, 1982.
- Williams, J. R., "Fast Beam-forming Algorithm," *J. Acoust. Soc. Am.*, vol. 44, no. 3, pp. 1454-1455, 1968.
- Williams, R. T., S. Prasad, A. K. Mahalanabis, and L. H. Sibul, "An Improved Spatial Smoothing Technique for Bearing Estimation in a Multipaths Environment," *IEEE Trans. Acoust. Speech Signal Processing*, vol. 36, no. 4, pp. 425-432, 1988.
- Yang, T. C., "Modal Beamforming Array Gain," *J. Acoust. Soc. Am.*, vol. 85, no. 1, pp. 146-151, 1989.
- Zhu, J. X. and H. Wang, "Adaptive Beamforming for Correlated Signal and Interferences: A Frequency-Domain Smoothing Approach," *Proc. ICASSP 88*, vol. V, pp. 2757-2760, 1988.
- Ziomek, L. J., *Underwater Acoustics, A Linear System Theory Approach*, Academic Press, U.K., 1985.
- Zoltowski, M. D., "On the Performance Analysis of the MVDR Beamformer in the Presence of Correlated Interference," *IEEE Trans. Acoust. Speech Signal Processing*, vol. 36, no. 6, pp. 945-947, 1988.



# ONR/MPL GENERAL DISTRIBUTION LIST

Chief of Naval Research  
Department of the Navy  
Arlington, Virginia 22217-5000  
Code 12, 122(2), 125  
1121, 112, 1122,  
1123, 1125, 1125 OA,  
1125 GG, 23

ONRDET  
Stennis Space Center  
Bay St. Louis, Mississippi 39529-5004  
Code 125

Commander  
Naval Sea Systems Command  
Washington, D. C. 20362  
Code 63DB, 933A

Commanding Officer  
Naval Ocean Research and  
Development Activity  
Stennis Space Center  
Bay, St. Louis, Mississippi 39529-5004  
Code 100, 110, 300, 330,  
200, 220, 240, 250, 270,  
320, 360, 350

Commander  
U.S. Naval Oceanographic Office  
NSTL Station  
Bay St. Louis, Mississippi 39522-5004  
Attn: Bill Jobst

Assistant Secretary of the Navy  
(Research Engineering & Systems)  
Department of the Navy  
Washington, D. C. 20350

Defense Advanced Res. Proj. Agency  
TTO - Tactical Technology Office  
1400 Wilson Boulevard  
Arlington, Virginia 22209-2308  
Attn: John N. Entzminger

National Oceanic & Atmospheric  
Administration  
Ocean Engineering Office  
6001 Executive Boulevard  
Rockville, Maryland 20852

Commander  
Space and Naval Warfare  
Systems Command  
Washington, D. C. 20360-5100  
Code FMW-180T, FMW-180-S

Commander  
Naval Ship Res. & Dev. Center  
Bethesda, Maryland 20084

Executive Secretary  
Naval Studies Board  
National Academy of Sciences  
2101 Constitution Avenue, N.W.  
Washington, D.C. 20418

Director  
Strategic Systems Proj. Ofc.  
Department of the Navy  
Washington, D. C. 20361  
Code NSP-20

Commander  
Naval Ocean Systems Center  
San Diego, California 92152  
Code 00, 01, 16, 94,  
54, 541, 605, 71, 72, 701

Commander  
Submarine Development Group ONE  
139 Sylvester Road  
San Diego, California 92106

Commanding Officer  
Civil Engineering Laboratory  
Naval Construction Battalion Center  
Port Hueneme, California 93043  
Code L40, L42

Commanding Officer  
Naval Underwater Systems Center  
Newport, Rhode Island 02844  
Attn: E.L. Sullivan

Officer in Charge  
Naval Underwater Systems Center  
New London Laboratory  
New London, Connecticut 06320  
Code 900, 905, 910, 930, 960

Director of Research  
U.S. Naval Research Laboratory  
Washington, D. C. 20375  
Code 2620, 2627, 5000, 5100, 5800

Officer in Charge  
Naval Surface Warfare Center  
10901 New Hampshire Avenue  
White Oak Laboratory Detachment  
Silver Spring, Maryland 20903-5000  
Attn: E232 Tech Library

Commanding Officer  
Naval Coastal Systems Laboratory  
Panama City, Florida 32401

STOIA  
Battelle Columbus Laboratories  
505 King Avenue  
Columbus, Ohio 43201

Commander  
Naval Air Systems Command  
Washington, D. C. 20361  
Code 370

Commanding Officer  
U.S. Naval Air Development Center  
Attention: Bruce Steinberg  
Warminster, Pennsylvania 18974

Director  
Defense Documentation Center  
(TIMA), Cameron Station  
5010 Duke Street  
Alexandria, Virginia 22314

Institute for Defense Analyses  
1801 North Beaupard Street  
Arlington, Virginia 22311

Superintendent  
U.S. Naval Postgraduate School  
Monterey, California 93940

Chief Scientist  
Navy Underwater Sound Reference Div.  
U.S. Naval Research Laboratory  
P.O. Box 8337  
Orlando, Florida 32806

Supreme Allied Commander  
U.S. Atlantic Fleet  
ASW Research Center, APO  
New York, New York 09019  
Via: ONR 100 M, CNO OF092D1,  
Secretariat of Military,  
Information Control, Committee

Director  
Institute of Marine Science  
University of Alaska  
Fairbanks, Alaska 99701

Director  
Applied Physics Laboratory  
Johns Hopkins University  
Johns Hopkins Road  
Laurel, Maryland 20810  
Attn: J. R. Austin

Director  
College of Engineering  
Department of Ocean Engineering  
Florida Atlantic University  
Boca Raton, Florida 33431

Director  
Marine Research Laboratories  
c/o Marine Studies Center  
University of Wisconsin  
Madison, Wisconsin 53706

Director  
Applied Research Laboratory  
Pennsylvania State University  
P.O. Box 30  
State College, Pennsylvania 16802

Director  
Applied Physics Laboratory  
University of Washington  
1013 NE 40th Street  
Seattle, Washington 98195

Director  
The Univ. of Texas at Austin  
Applied Research Laboratory  
P.O. Box 8029  
Austin, Texas 78712

Director  
Lamont-Doherty Geological Observatory  
Torrey Cliff  
Palisades, New York 10964

Director  
Woods Hole Oceanographic Institution  
Woods Hole, Massachusetts 02543

Director  
Inst. of Ocean Science Engineering  
Catholic University of America  
Washington, D.C. 20017

National Science Foundation  
Ocean Sciences Division  
Washington, D. C. 20550

Office of Naval Research  
Resident Representative  
c/o Univ. of California, San Diego  
Mail Code 0023  
La Jolla, California 92093

University of California, San Diego  
Marine Physics Laboratory  
Branch Office  
La Jolla, California 92093